ΔO2/N2' as a Tracer of Mixed Layer Net Community Production: Theoretical Considerations and Proof-of-Concept

Robert W. Izett[1,1] and Philippe D. Tortell[1,1]

[1]University of British Columbia

November 30, 2022

Abstract

The biological oxygen (O2) saturation anomaly ΔO2/Ar is a tracer for net community production (NCP) in marine surface waters, with argon (Ar) normalization used to correct for physical effects on O2 supersaturation. Ship-board mass spectrometry has been used for ΔO2/Ar measurements, but this approach may not be accessible to many research groups. Here, we present a proof-of-concept for NCP estimates based on underway measurements of ΔO2/N2, which can be obtained from deployments of O2-Optodes and gas tension devices (GTD). We used a one-dimensional mixed layer model, validated against field observations, to evaluate divergence in ΔO2/Ar and ΔO/N2 resulting from differences in the sensitivity of Ar and nitrogen (N2) to various physical processes. Changes in sea surface temperature and responses in air-sea exchange most strongly decouple surface Ar and N2 with additional excess N2 associated with bubble-injection during high-wind conditions and vertical mixing in regions of elevated subsurface N2. In contrast, biological N2-fixation has a negligible contribution to the observed divergence between Ar and N2. Based on readily available environmental data, we present an approach to correct for Ar and N2 differences, yielding a new tracer, N2', that is a near analog of Ar. We show that ΔO2/N2' provides an excellent approximation to ΔO2/Ar, and that uncertainty and biases in ΔO2/N2' are small relative to other errors in NCP calculations. Our results demonstrate the potential for ΔO2/N2' measurements to expand NCP estimates from oceanographic research surveys, vessels of opportunity or autonomous surface vehicles.

$\Delta O_2/N_2'$ as a Tracer of Mixed Layer Net Community Production: Theoretical Considerations and Proof-of-Concept

Robert W. Izett[1], and Philippe D. Tortell[1,2]

[1] Department of Earth, Ocean and Atmospheric Sciences, University of British Columbia, Vancouver, BC, Canada.

[2] Botany Department, University of British Columbia, Vancouver, BC, Canada.

Corresponding author: Robert Izett (*rizett@eoas.ubc.ca*)

Key Points:

- Numerical simulations are used to evaluate physically-induced changes in mixed layer N_2 and Ar saturation from environmental forcing data

- A new tracer, N_2', is derived, using simple computations to correct for differential physical effects on N_2 and Ar saturation

- $\Delta O_2/N_2'$ is shown to be an excellent alternative to $\Delta O_2/Ar$ for calculations of surface net community production

Abstract

The biological oxygen (O_2) saturation anomaly ($\Delta O_2/Ar$) is a tracer for net community production (NCP) in marine surface waters, with argon (Ar) normalization used to correct for physical effects on O_2 supersaturation. Ship-board mass spectrometry has been used for $\Delta O_2/Ar$ measurements, but this approach may not be accessible to many research groups. Here, we present a proof-of-concept for NCP estimates based on underway measurements of $\Delta O_2/N_2$, which can be obtained from deployments of O_2-Optodes and gas tension devices (GTD). We used a one-dimensional mixed layer model, validated against field observations, to evaluate divergence in $\Delta O_2/Ar$ and $\Delta O_2/N_2$ resulting from differences in the sensitivity of Ar and nitrogen (N_2) to various physical processes. Changes in sea surface temperature and responses in air-sea exchange most strongly decouple surface Ar and N_2, with additional excess N_2 associated with bubble-injection during high-wind conditions and vertical mixing in regions of evelated subsurface N_2. In contrast, biological N_2-fixation has a negligible contribution to the observed divergence between Ar and N_2. Based on readily available environmental data, we present an approach to correct for Ar and N_2 differences, yielding a new tracer, N_2', that is a near analog of Ar. We show that $\Delta O_2/N_2'$ provides an excellent approximation to $\Delta O_2/Ar$, and that uncertainty and biases in $\Delta O_2/N_2'$ are small relative to other errors in NCP calculations. Our results demonstrate the potential for $\Delta O_2/N_2'$ measurements to expand NCP estimates from oceanographic research surveys, vessels of opportunity or autonomous surface vehicles.

Plain Language Summary

Marine net community production, NCP, represents the difference between biological oxygen (O_2) production through photosynthesis and O_2 consumption through respiration. This quantity reflects the ocean's capacity to support marine life and remove carbon dioxide from the atmosphere. One common approach to estimate NCP employs mass spectrometry to measure the oxygen-to-argon ratio ($\Delta O_2/Ar$) in surface seawater. Since Ar is biologically inert and has similar physical properties to O_2, this approach is used to examine marine biological production. However, the instrumentation required to measure $\Delta O_2/Ar$ is expensive and requires significant technical oversight, thus limiting the coverage of observations. Here, we use simple numerical simulations to show that NCP can be accurately derived from the seawater O_2-to-nitrogen ratio ($\Delta O_2/N_2$). We derive a new term, $\Delta O_2/N_2'$, that corrects for small differences between $\Delta O_2/N_2$ and $\Delta O_2/Ar$ resulting from the enhanced sensitivty of N_2 to bubbles, seawater temperature changes and mixing effects. NCP calculated from $\Delta O_2/N_2'$ provides an excellent alternative to $\Delta O_2/Ar$-based estimates, and uncertainty in $\Delta O_2/N_2'$ is low relative to other error sources in NCP calculations. As $\Delta O_2/N_2$ can be measured autonomously at sea with simple instrumentation, our results demonstrate the potential to expand coverage of NCP estimates from a variety of sampling platforms.

1 Introduction

Net community production (NCP) quantifies the balance between gross photosynthetic production and community-wide respiration, and serves as an important metric of the metabolic state of an ocean region. Integrated over seasonal timescales, NCP constrains upper limits on marine biomass production and carbon export from the ocean surface via the biological pump.

62 As such, the spatial and temporal distribution of marine NCP has significant implications for
63 food web dynamics and global biogeochemical cycles. To understand and predict the response of
64 marine systems to future environmental change, it is therefore important to quantify NCP on
65 ecologically-relevant time and space scales.

66 An increasingly common approach for deriving oceanic NCP estimates at high spatial
67 resolution employs ship-based mass spectrometry to obtain underway measurements of the
68 seawater oxygen-to-argon ratio (O_2/Ar). This approach relies on the nearly identical solubility
69 properties of O_2 and its biologically-inert analog Ar, which make O_2/Ar largely insensitive to
70 temperature or salinity-dependent solubility changes, or bubble injection processes (Craig &
71 Hayward, 1987; Fig. S1). The biological saturation anomaly (ΔO_2/Ar, Eq. 1) thus provides a
72 specific tracer for net biological O_2 production, and can be derived by normalizing measured
73 O_2/Ar ($[O_2/Ar]_{sw}$) to the seawater equilibrium ratio ($[O_2/Ar]_{eq}$).

74
$$\Delta O_2/Ar = \left(\frac{[O_2/Ar]_{sw}}{[O_2/Ar]_{eq}} - 1 \right) \cdot 100 \ \% \tag{1}$$

75 Net community production is then equated to the air-sea flux of biologically-produced excess O_2
76 (i.e. the "bioflux" of $\Delta O2/Ar \cdot [O2]_{eq}$; Jonsson et al., 2013; Kaiser et al., 2005; Teeter et al.,
77 2018). This approach has been applied to obtain broad spatial coverage of NCP estimates from
78 ship-based surveys, thus improving our understanding of marine carbon cycling (e.g. Hamme et
79 al., 2012; Howard et al., 2010; Izett et al., 2018; Juranek et al., 2019; Lockwood et al., 2012;
80 Rosengard et al., 2020; Tortell et al., 2015; Ulfsbo et al., 2014). However, the expense of mass
81 spectrometers and the technical expertise required to run these instruments may be prohibive to
82 some research groups. Additionally, mass spectrometers can have significant power consumption
83 requirements and are generally not capable of fully-autonomous deployments, thus limiting their
84 use to scientific research vessels with dedicated infrastructure and personnel. Truly autonomous
85 gas measurements on ships of opportunity, or in-situ platforms such as autonomous surface
86 vehicles (e.g. Saildrone), would significantly expand the global coverage of NCP estimates from
87 underway surveys, helping to integrate these measurements with a growing suite of autonomous
88 biogeochemical and ecological observations (Gordon et al., 2020; Johnson et al., 2017; Mordy et
89 al., 2017; Pelland et al., 2018; Plant et al., 2016; Yang et al., 2017).

90 The development of O_2 Optodes (Tengberg et al., 2006) and Gas Tension Devices
91 (GTDs; McNeil et al., 2006a; Reed et al., 2018) capable of stable, accurate measurements during
92 extended in-situ deployments provides new opportunities for autonomous NCP surveys. Using
93 observations of O_2 from the Optode and the seawater total dissolved gas pressure (i.e. the sum of
94 all gas partial pressures) from the GTD, it is possible to obtain estimates of seawater nitrogen
95 (N_2) concentrations (McNeil et al., 1995). Nitrogen has roughly similar physical properties to O_2
96 (i.e. salinity and temperature solubility dependence; Fig. S1), such that NCP could, in principle,
97 be approximated from N_2-based calculations of the biological O_2 saturation anomaly (i.e.
98 $\Delta O_2/N_2$, following Eq. 1).

99 To date, O_2 and N_2 measurements have been combined to estimate NCP time-series from
100 Optode and GTD deployments on moorings and/or floats (e.g. Bushinsky & Emerson, 2015;
101 Emerson & Stump, 2010; Weeding & Trull, 2014; Yang et al., 2017). These applications employ
102 simultaneous observations of sea surface temperature, salinity and wind speed to estimate the
103 contribution of physical processes driving changes in O_2 solubility, thereby isolating a biological
104 signature of NCP without the need for Ar or N_2 normalization. In these studies, mooring-based

105 N$_2$ measurements are commonly used to estimate the effects of physical processes on the mixed
106 layer O$_2$ budget, most importantly air-sea flux via bubbles (Emerson et al., 2019). Thus far,
107 direct estimates of NCP from O$_2$ and N$_2$ measurements have only been obtained from ship-based
108 depth profiles (McNeil et al., 2006b) or in-ice measurements (Zhou et al., 2014). To our
109 knowledge, no previous work has derived NCP from underway surface $\Delta O_2/N_2$, although Tortell
110 et al. (2015) used simultaneous O$_2$/N$_2$ and O$_2$/Ar data to describe physical and biological controls
111 on O$_2$ across various hydrographic regimes in the Southern Ocean.

112   A key challenge in the use of $\Delta O_2/N_2$ measurements as an NCP tracer is accounting for
113 divergences in mixed layer $\Delta O_2/Ar$ and $\Delta O_2/N_2$ resulting from the slightly different solubility
114 properties of Ar and N$_2$ (Fig. S1). Nitrogen is less soluble in water than O$_2$ and Ar, and is
115 therefore more susceptible to bubbled-induced supersaturation (Craig & Hayward, 1987; Weiss,
116 1970; Woolf & Thorpe, 1991). Moreover, small differences in the temperature-sensitivity of
117 O$_2$/Ar and O$_2$/N$_2$ induce differential responses to surface warming or cooling. Finally, N$_2$, unlike
118 Ar, is not entirely inert, as its concentration can be altered by N$_2$-fixation, denitrification, and
119 annamox. If differences between Ar and N$_2$ supersaturation anomalies (ΔAr and ΔN_2,
120 respectively) are sufficiently large and unaccounted for, interpretations of NCP estimated from
121 $\Delta O_2/N_2$ could be biased, with significant implications for the interpretation of oceanic net tropic
122 status and metabolic state.

123   The primary goal of this article is to demonstrate the utility of $\Delta O_2/N_2$ measurements as
124 an alternative to $\Delta O_2/Ar$ for NCP estimates. We present simulations from a simple one-
125 dimensional model, validated against in-situ N$_2$ and O$_2$ measurements, to evaluate differences
126 between $\Delta O_2/Ar$ and $\Delta O_2/N_2$ resulting from ΔAr and ΔN_2 divergence in surface waters. Based on
127 the simulations, we tested a framework for predicting these differences from readily-available
128 environmental data, and derived a new tracer, N$_2$' ("N$_2$-prime"), which accounts for excess ΔN_2
129 relative to ΔAr. We conclude by evaluating the uncertainty in NCP calculations based on
130 $\Delta O_2/N_2$' measurements. Our results demonstrate the potential for underway, ship-based
131 observations of $\Delta O_2/N_2$ (and derived $\Delta O_2/N_2$') to expand coverage of NCP estimates in oceanic
132 waters. In the supporting information (SI), we provide details and software code for the
133 application of the N$_2$' approach to field surveys. In related articles (Izett & Tortell, 2020) we
134 describe an underway measurement system for ship-board O$_2$/N$_2$ surveys, and provide a field-
135 validation of the approach proposed here (manuscript in preparation).

136

137 **2 Methods**

138   2.1 One-dimensional mixed layer physical gas model

139   We developed a simple one-dimensional mixed layer box model to evaluate mechanisms
140 driving the divergence between ΔAr and ΔN_2 under various environmental forcing conditions
141 (i.e. $\Delta C = (C/C_{eq} - 1) * 100$ %, where C_{eq} is the equilibrium solubility concentration at ambient
142 sea level pressure). We also tested an empirical approach for correcting these offsets, which is
143 described in section 2.2. The model predicts the evolution of mixed layer gas concentrations
144 resulting from physical perturbations, including temperature-dependent solubility changes, air-
145 sea exchange, and vertical mixing. The following budget was applied to O$_2$, Ar and N$_2$:

146
$$MLD \cdot \frac{dC}{dt} = F_d + F_B + F_M. \tag{2}$$

147   Here, MLD is the mixed layer depth, dC/dt is the change in gas concentration over time,
148 F_d and F_B are the air-sea gas exchange fluxes via diffusion and bubbles (from both fully- and
149 partially-collapsing bubbles), respectively, and F_M represents the sum of diapycnal mixing,
150 upwelling and entrainment of water from below the mixed layer. We employ a two-box domain,
151 with prescribed hydrographic properties in the subsurface and mixed layers (see below). Unless
152 otherwise stated, we excluded biological production of O_2 and N_2 and ignored lateral fluxes (see
153 below).

154   We used the air-sea exchange parameterization of Liang et al. (2013) in ice-free
155 simulations. For Arctic simulations (fractional ice cover >1 %) we excluded explicit bubble
156 fluxes, but scaled bulk gas exchange rates with the fraction of ice-free water following
157 Butterworth & Miller (2016). Net air-sea exchange fluxes differ by less than 5 % between these
158 two parameterizations at winds speeds below ~10 m s^{-1}, thus justifying our exclusion of bubble
159 processes in waters with >1 % ice coverage. We note that the time-series of N_2 and Ar predicted
160 by our simulaitons, and the relative differences between them, will depend on the air-sea
161 diffusion rates of these gases applied in our model domain. The Liang et al. (2013) bubble-
162 mediated flux model is based on Ar diffusion rates which are believed to exceed those of N_2
163 (Fig. S1). There is, however, some disagreement in the literature, with suggestions that N_2
164 diffusion may exceed Ar (e.g. Wise & Houghton, 1966). Nonetheless, the results presented here
165 are consistent with the majority of studies describing surface diffusion rates (e.g. see within
166 Wanninkhof, 2014), and the Liang et al. model has been validated for N_2 and other similar gases
167 (Emerson & Bushinsky 2016; and see below, section 3.3). The analyses presented throughout
168 this manuscript are thus based on the assumption that Ar diffusion rates exceed those of N_2.

169   The mixing flux term encompasses diapycnal mixing, upwelling and entrainment, and is
170 proportional to the vertical gas gradient (i.e. $dC/dZ = (C_{deep} - C_{surf}) / dZ$, where C_{deep} is the
171 subsurface gas concentration). Terms for these fluxes are derived from a prescribed eddy
172 diffusivity coefficient (κ_Z), Ekman pumping velocity (ω, proportional to wind speed; Hartmann,
173 1994) and the rate of MLD deepening (dMLD/dT), respectively. These parameterizations are
174 described briefly below, with full details presented in section S1 of the SI. Model code for
175 performing simulations is also provided at doi.org/10.5281/zenodo.4024952.

176   We performed sensitivity analyses comparing our simulated gas time-series with in-stiu
177 observations (see below section 3.3) to determine appropriate parameterizations for the bubble
178 scaling factor, β, and the integration depth scale, dZ, over which vertical mixing fluxes are
179 estimated.

180   From these analyses, we found that a bubble flux scaling coefficient, β, of 0.5 produces
181 best results, and is consistent with results from Yang et al. (2017) and Emerson et al. (2019). A
182 vertical mixing depth scale, dZ, proportional to the thermocline depth, is also most appropriate,
183 but is generally insensitive to small variability (e.g. ±10 m). In the experimental simulations, dZ
184 was set to a constant value (25 m) based on an empirical relationship between MLD and the
185 thermocline depth.

186   The model was initialized and forced with either real observations or simulated values, as
187 described below. Unless otherwise stated, sea level pressure (SLP), salinity and MLD were held
188 constant, and gas concentrations were initialized at 100 % saturation using the solubility
189 equations of Garcia & Gordon (1993) and Hamme & Emerson (2004). Subsurface Ar (ΔAr_{deep})
190 was set based on previously published observations, and $\Delta N_{2,deep}$ was varied in each model run

191 by adjusting subsurface $\Delta N_2/Ar$ (i.e. $\Delta N_2/Ar_{deep} = (N_{2,sat,deep} / Ar_{sat,deep} - 1) \cdot 100\%$). Our
192 simulations neglect lateral fluxes as they are generally small in a Eulerian framework, and
193 irrelevant to underway surveys which measure gas concentrations that have been modified along
194 a Lagrangian flow path (Teeter et al., 2018).

195

196   2.1.1 Model simulations

197   We performed six simulations with our gas model to examine the main drivers of ΔAr
198 and ΔN_2 divergence. Table 1 summarizes the different forcing conditions used for these
199 simulations. For all model runs, we performed calculations in 0.25-day time increments, and
200 omitted the first 90 days of output so that the simulated results were independent of initial
201 conditions. Four of the simulations (denoted as 'experimental' and named with the prefix 'Ex')
202 were designed to represent the impacts of extreme temperature (SST) and wind speed (u_{10})
203 variability in ice-free (runs Ex-IF 1, Ex-IF 2, and Ex-IF 3) and partially ice-covered (run Ex-IC
204 1) waters. Two additional simulations (denoted as 'realistic' and named with the prefix 'real')
205 included more realistic environmental forcing, based on in-situ observations at Ocean Station
206 Papa in the Subarctic Pacific (real-OSP) and Baffin Bay (real-BB) in the eastern Arctic,
207 respectively.

208   In the experimental runs, initial conditions (temperature and salinity profiles) were
209 derived from representative 2019 observations from Ocean Station Papa (50 ºN, 145 ºW; runs
210 Ex-IF 1–3) and northern Baffin Bay (67 ºN, 62.5 ºW; Ex-IC 1) (data provided by the Institute of
211 Ocean Sciences, DFO Canada at www.waterproperties.ca/linep and by Amundsen Science Data
212 Collection, 2019 at www.polardata.ca). To simulate extreme environmental change, we
213 introduced two rapid step-changes in u_{10} (between 7 and 15 m s^{-1}) and SST (± 4 ºC) based on
214 observed variability in Subarctic NE Pacific and Arctic field studies (R. Izett and P. Tortell
215 unpublished results). Mixed layer depth, salinity, subsurface properties and dZ were derived
216 from the initial conditions and held constant throughout the run. For each set of conditions, we
217 performed three runs (details in Table 1): (a) no mixing; (b) dampened mixing; (c) full mixing.
218 For runs b and c, we prescribed κ_Z values and scaled ω (upwelling velocity) with u_{10}.
219 Entrainment was set to zero, because the MLD was constant. We set the value of $\Delta N_2/Ar_{deep}$ to
220 1.5 % in the experimental simulations based on the observed upper range of $\Delta N_2/Ar$ just below
221 the mixed layer in most ocean basins (e.g. Hamme et al., 2017, 2019; Hamme & Emerson, 2013;
222 Nicholson et al., 2010). Although subsurface $\Delta N_2/Ar_{deep}$ can range from <0 % to >2 % (Chang et
223 al., 2010, 2012; Hamme et al., 2019; Shigemitsu et al., 2016), values greater than ~1.5 % are rare
224 outside of tropical and sub-tropical zones impacted by near-surface water column denitrification.

225   In the realistic simulations, u_{10} and SST data were obtained from in-situ mooring
226 observations (real-OSP) or gridded reanalysis products (real-BB). In the Subarctic Pacific runs,
227 we approximated a two year cycle (2011-2013) using u_{10}, SST and SLP data from the NOAA
228 PMEL mooring at OSP (provided by NOAA PMEL at www.pmel.noaa.gov). For the Baffin Bay
229 simulations (representing May – October, 2019), u_{10} data were obtained from the CCMP vector
230 product (provided by Remote Sensing Systems at www.remss.com/measurements/ccmp/; Atlas
231 et al., 2011), while SST and sea ice percent-coverage were from the NOAA High Resolution OI
232 Dataset (provided by NOAA ESRL at psl.noaa.gov; Reynolds et al., 2007) and SLP was from the
233 NCEP/NCAR reanalysis 2 product (provided by NOAA ESRL at *psl.noaa.gov*; Kalnay et al.,
234 1996). In both realistic simulations, we applied a time-variable MLD based on density

235 measurements obtained on the OSP mooring line (real-OSP), or from the NOAA MIMOC mixed
236 layer depth climatology (real-BB; provided by NOAA PMEL at pmel.noaa.gov/mimoc;
237 Schmidtko et al., 2013). We performed two simulation runs representing different mixing
238 scenarios (Table 1), omitting the weak mixing scenario (i.e. run b). In run c of the OSP
239 simulation (i.e. full mixing), we applied time-varied κ_z by extrapolating the results from Cronin
240 et al. (2015) onto our model domain. In real-BB run c, time-variable κ_z was set based on eddy
241 diffusivity values obtained from NEMO model simulations of the Arctic and N. Atlantic (NEMO
242 model simulations described in Castro de la Guardia et al., 2019). Subsurface gases were set
243 based on calculated equilibrium concentrations at the deep temperature and salinity conditions,
244 and from supersaturation anomalies based on archived observations below the MLD in the
245 subarctic Pacific and Labrador Sea (provided at www.bco-dmo.org; Hamme et al., 2019). In real-
246 OSP run c, ΔAr_{deep} and $\Delta N_2/Ar_{deep}$ were interpolated from observations from multi-year sampling
247 at OSP in February, June and August to the model run time (ranges 0-1 % and 0-0.5 %,
248 respectively). In real-BB run c, ΔAr_{deep} and $\Delta N_2/Ar_{deep}$ were held constant 0 % and 0.5 %,
249 respectively. Temperature, salinity and O_2 in the "deep" boxes (i.e. the layer beneath the MLD)
250 were based on observations at the OSP mooring (real-OSP) or from profile measurements and
251 NEMO model output in northern Baffin Bay (real-BB). In the real-OSP and real-BB simulations,
252 we applied biological production terms to the O_2 budget (Eq. 2) based on field observations from
253 the respective regions to better reflect seasonal ΔO_2 variability (mean annual cycle at OSP from
254 Fassbender et al., 2016 and constant NCP in BB from on R. Izett and P. Tortell unpublished
255 results).

256
257

Table 1. Summary of model simulation conditions. Vertical advection and entrainment fluxes
were set to zero in run a of all simulations, and were proportional to wind speed and the rate of
MLD deepening in runs b and c, respectively. Initial conditions were obtained from ship-based
observations at Ocean Station Papa (OSP) in the Subarctic Pacific, NOAA mooring data at OSP,
or ship-based measurements in Baffin Bay (BB). The three numbers listed for SST and u_{10}
correspond with values used during each of three forcing time segments (days 0-12, 12-65, and
65-1 20 in Fig. 1). In the real-OSP and real-BB run c, we derived time-variable κ_z from Cronin et
al. (2015) and NEMO model simulations, respectively, while $\Delta N_2/Ar_{deep}$ was based on archived
values from Hamme et al. (2019). Both terms were set to zero in run a of the realistic
simulations. We did not perform intermediate mixing scenarios (i.e. run b) for the realistic
simulations. The results of these simulations are shown in Figs. 2-4.

Simulation (duration)	Forcing					Mixing	
	deep & initial conditions	SST [ºC]	u_{10} [m s^{-1}]	ice [%]	SLP [mbar]	κ_z [m^2 s^{-1}]	$\Delta N_2/Ar_{deep}$ [%]
Ex-IF 1 (120 days)	OSP pofile	10, 10, 10	7, 15, 7	0	1013.25		
Ex-IF 2 (120 days)	OSP profile	10, 14, 10	7, 7, 7	0	1013.25	Run a: 0 Run b: 10^{-5} Run c: 10^{-4}	Run a: 0 Run b: 1.5 Run c: 1.5
Ex-IF 3 (120 days)	OSP profile	6, 10, 14	7, 15, 7	0	1013.25		
Ex-IC 1 (120 days)	BB profile	0, 4, 8	7, 15, 7	50	1013.25		
real-OSP (Jan. 2011- Jan. 2013)	NOAA OSP mooring profile	NOAA OSP mooring	NOAA OSP mooring	0	NOAA OSP mooring	Run a: 0 Run c: Cronin	Run a: 0 Run c: Hamme
real-BB (May – Oct. 2019)	BB profile	NOAA OI SST product	CCMP product	NOAA OI ice product	NCEP/ NCAR reanalysis	Run a: 0 Run c: NEMO	Run a: 0 Run c: 0.5

2.2 Derivation of N_2'

Based on our simulations, we developed a framework to reconcile the differences
between surface water $\Delta O_2/Ar$ and $\Delta O_2/N_2$ resulting from differential solubility effects and
physical fluxes of Ar and N_2. From this analysis, we derived a new tracer, N_2' ("N_2-prime") that
corrects for these differences and provides an Ar analog. For this approach, we used a slightly
simplified version of the gas budget described in Eq. 2 to predict the difference between ΔN_2 and
ΔAr occurring over a timescale relevant to NCP calculations. We then subtracted this estimated
offset from ΔN_2 derived from the full model simulations. We modified Eq. 2 by combining all
vertical mixing processes into a single term, expressing the rates of diapycnal mixing and
advection with a single coefficient, κ. We excluded entrainment from the simplified budget
because temporal variability in MLD (i.e. dMLD/dt) cannot be estimated readily from ship-based
sampling. The simplified budget is represented by:

283
$$\text{MLD} \cdot \frac{dC}{dt} = F_d + F_C + F_P + \frac{C_{deep} - C}{dZ} \kappa \qquad (3)$$

284 where F_d, F_C and F_P are the diffusive, small bubble and large bubble air-sea exchange fluxes, as
285 described above. We evaluated this budget for Ar and N_2 over one mixed layer O_2 re-
286 equilibration timescale, τ_{O2} (defined in section 3.1.2, Eq. 6, and derived in section S1 of the SI),
287 prior to each calculation derived from the full model simulations. As in the full simulations, we
288 set the starting gas concentrations to equilibrium values (i.e. $C(t\text{-}\tau_{O2}) = C_{eq} \frac{SLP}{1\,atm}$) and performed
289 calculations in 0.25-day increments. The same environmental data used to force the full model
290 simulations (i.e. u_{10}, SST and SLP) were applied in Eq. 3. Finally, we obtained $\Delta N_2'$ by
291 subtracting the derived difference between ΔAr and ΔN_2 ($\Delta N_2^{est} - \Delta Ar^{est}$) from the
292 corresponding ΔN_2 value predicted by the full model (ΔN_2^{true})

293
$$\Delta N_2' = \Delta N_2^{true} - (\Delta N_2^{est} - \Delta Ar^{est}) \qquad (4)$$

294 and recalculated $\Delta O_2/N_2'$ from $\Delta N_2'$ following Eq. 1.

295   In field studies, ΔN_2^{true} will be the measured value, and ΔN_2^{est} and ΔAr^{est} will be values
296 predicted by the simplified gas budget (Eq. 3) using environmental data over one τ_{O2} before
297 observations. An example of the approach is presented in the SI (Fig. S2). Whereas estimates of
298 u_{10}, SST and SLP over τ_{O2} can be obtained from readily available reanalysis products, the time-
299 histories of MLD, surface salinity, and sub-surface conditions are more difficult to estimate. For
300 compatibility with field studies, we therefore fixed these terms (MLD, salinity, deep temperature,
301 deep salinity, κ, $\Delta N_2/Ar_{deep}$) over τ_{O2} at values corresponding with the time of ΔN_2^{true} (i.e. the
302 time of in-situ sampling during field sampling). Moreover, given the paucity of in-situ
303 subsurface noble gas measurements, we set ΔAr_{deep} to 0 % in all N_2' calculations, and held
304 $\Delta N_2/Ar_{deep}$ constant at values from the full model run corresponding with the time of ΔN_2^{true}. In
305 section 3.4.3, we evaluate errors in $\Delta N_2'$ and $\Delta O_2/N_2'$ resulting from these simplifying
306 assumptions.

307

308 **3 Results and Discussion**

309   Differences between mixed layer $\Delta O_2/Ar$ and $\Delta O_2/N_2$ are most simply represented using
310 the term $\Delta N_2/Ar$ (i.e. ($[N_2/Ar]/[N_2/Ar]_{eq} - 1) \cdot 100$ %), which is not sensitive to ΔO_2, and thus not
311 dependent on biological O_2 production in our modeling framework (Figs. S3, S6). Our
312 experimental simulations (Ex-IF and Ex-IC; section 3.1) were designed to evaluate the effects of
313 different physical factors on $\Delta N_2/Ar$, including bubble-mediated and diffusive gas transfer,
314 vertical mixing and sea ice cover. The realistic simulations (real-OSP and real-BB; section 3.2)
315 allowed us to evaluate the combined influence of these processes, and test our N_2' framework
316 under typical oceanographic conditions. Below, we discuss the relative effects of different
317 processes on gas variability, present a validation of the model against field observations, and
318 show that our N_2' approach can correct for most of the difference between ΔN_2 and ΔAr
319 saturation. We conclude by evaluating $\Delta O_2/N_2'$ as an NCP tracer and identifying the main
320 sources of uncertainty associated with the use of this approach. In a subsequent paper, we will
321 present a field validation of $\Delta O_2/N_2'$ measurements for NCP derivation. The SI of the present
322 manuscript contains details and annotated software scripts for applying the N_2' approach to field
323 data (section S3).

324

325   3.1 Mixed layer model experimental simulation results

326   A quasi-steaty-state condition can be predicted from the MLD budget described in Eq. 3.
327 Analysis of these conditions in our model reveals that bubble processes, mediated by sustained
328 high wind speeds, can induce the largest $\Delta N_2/Ar$ disequilibria, with values potentially exceeding
329 1.5 % at u_{10} of 20 m s^{-1} (Fig. 1). Notably, elevated wind speeds always produce positive $\Delta N_2/Ar$
330 (i.e. $\Delta N_2 > \Delta Ar$ and $\Delta O_2/Ar > \Delta O_2/N_2$), because of the lower solubility of N_2 relative to Ar (Fig.
331 S), and its greater sensitivity to small bubble injection (Hamme et al., 2019; Liang et al., 2013).
332 However, the bubble effect can be either dampened or enhanced by vertical mixing processes,
333 such that the quasi-steady-state value of $\Delta N_2/Ar$ represents the relative influence of bubble
334 processes and sustained mixing, which may increase or decrease $\Delta N_2/Ar$, depending on
335 $\Delta N_2/Ar_{deep}$. The role of these two processes is reflected in the equation for the quasi-steady-state
336 gas concentration, C_{SS}, derived in section S1 of the SI from the analytical solution to the N_2'
337 MLD gas budget (Eq. 3):

338
$$C_{SS} = \frac{k_T \cdot C_{eq} \cdot (1 + \Delta_{eq}) \cdot \frac{SLP}{1\,atm} + \frac{\kappa}{dz} \cdot C_{deep}}{k_T + \frac{\kappa}{dz}} \ . \tag{5}$$

339 Here, k_T is the combined u_{10}-dependent diffusive and bubble-mediated exchange velocity, and
340 Δ_{eq} is the bubble-induced steady-state supersaturation anomaly. Evaluating Eq. 5 for Ar and N_2
341 enables derivation of the quasi-steady-state $\Delta N_2/Ar$ value.

342   As shown in Fig. 1, surface $\Delta N_2/Ar$ depends, to first order, on u_{10}, vertical mixing rates
343 and the value of $\Delta N_2/Ar$ below the mixed layer. As rates of vertical mixing increase and/or
344 $\Delta N_2/Ar_{deep}$ decreases, bubble effects are dampened. For example, for κ and $\Delta N_2/Ar_{deep}$ values of
345 10^{-3} m^2 s^{-1} and -0.5 %, respectively, our model predicts negative quasi-steady-state $\Delta N_2/Ar$
346 across a range of wind speeds ($u_{10} < 15$ m s^{-1}). Without vertical mixing, $\Delta N_2/Ar$ is set by the
347 relative bubble-induced supersaturation states, Δ_{eq}, of N_2 and Ar (grey lines in Fig. 1), while in
348 the absence of bubble processes, the quasi-steady-state $\Delta N_2/Ar$ falls between $\Delta N_2/Ar_{deep}$ and
349 zero, depending on the strength of mixing (evaluate Eq. 5 for Δ_{eq} set to 0 %). This analysis
350 illustrates the importance of bubble processes and vertical mixing in setting baseline $\Delta N_2/Ar$ in
351 marine surface waters.

352   As described below, variability in u_{10}, SST and mixing strength on shorter time-scales
353 (i.e. days) can induce significant transient signals in $\Delta N_2/Ar$. In contrast, atmospheric pressure
354 alters all gas saturation states equally, such that SLP variability has no effect on $\Delta N_2/Ar$ (Hamme
355 et al., 2019).

356
357
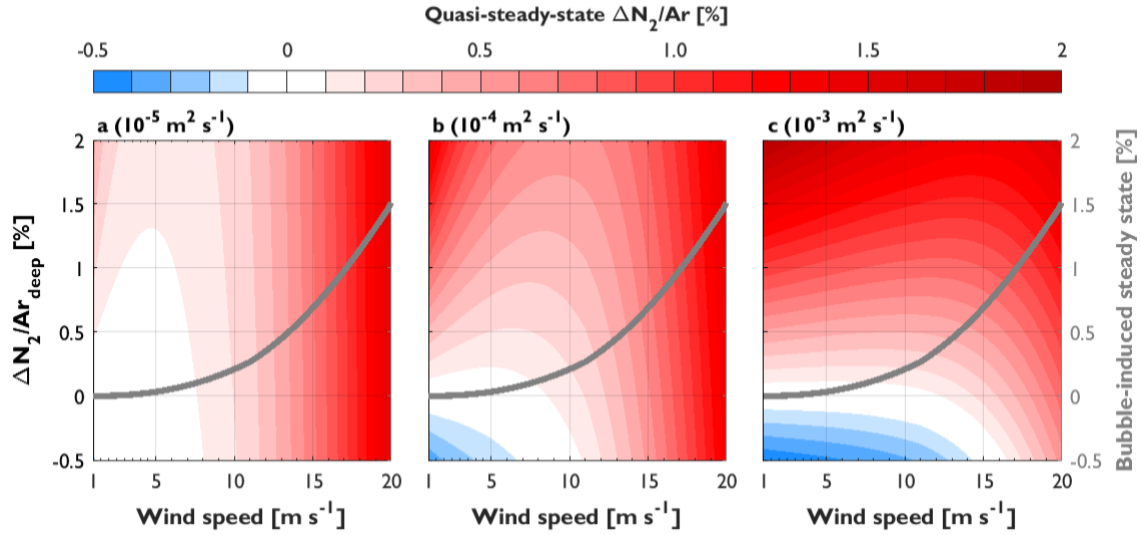
Figure 1. The combined effects of wind speed and mixing on steady-state $\Delta N_2/Ar$ derived from model simulations. Colour scaling represents the quasi-steady-state surface $\Delta N_2/Ar$ predicted by our model at SST and salinity values of 10 °C, and 34 PSU, respectively, based on equations presented in section S1.2 of the SI. The thick grey line represents the average bubble-induced steady-state condition (i.e. proportional to $\Delta_{eq,N2}/\Delta_{eq,Ar}$) without mixing over a range of SST (0-25 °C). Panels represent a gradient from weakest (a) to strongest (c) mixing, with values of the mixing coefficient, κ, given at the top left of each panel.

3.1.1 Effects of variable wind speed, temperature and sea ice coverage

In practice, the ocean mixed layer rarely exists in a steady-state condition, and it is thus necessary to understand the dynamic response of mixed layer gases to transient physical perturbations. We used our experimental simulations to examine the response of $\Delta N_2/Ar$ to rapid changes in u_{10} (Ex-IF 1, 3, 4), SST (ΔSST; Ex-IF 2, 3, 4) and see ice cover (Ex-IC 1). In these simulations, u_{10} variability induces large responses in surface $\Delta N_2/Ar$ resulting from bubble processes, with the rate of re-equilibration to steady-state values also depending on u_{10} (Fig. 2a, c). In our simulations without mixing or rapid SST changes (Ex-IF 1a; Fig. 2a), the maximum $\Delta N_2/Ar$, was ~0.7 % at a wind speed of 15 m s^{-1}, but values can exceed 1.5 % for speeds >20 m s^{-1} (Fig. 1).

Temperature changes can enhance or dampen $\Delta N_2/Ar$ disequilibria by affecting gas saturation states over both long (i.e. seasonal) and shorter (days to weeks) time-scales (e.g. Emerson & Stump, 2010; Hamme et al., 2019; Hamme & Emerson, 2002; Hamme & Severinghaus, 2007; Steiner et al., 2007). If air-sea exchange rates are low, temperature-driven $\Delta N_2/Ar$ disequilibrium can persist for extended periods, while rapid ΔSST or periodic elevated wind events induce near-instantaneous disturbances in $\Delta N_2/Ar$, preventing gases from reaching steady-state values. In the absence of mixing, gas supersaturation anomalies will increase (decrease) if the rate of warming (cooling) exceeds the rate of re-equilibration via air-sea exchange. While bubble processes only produce positive $\Delta N_2/Ar$, temperature changes can lead to negative $\Delta N_2/Ar$ (i.e. $\Delta O_2/Ar < \Delta O_2/N_2$). Such SST effects occur through two mechanisms, which are represented in the Ex-IF 2 and Ex-IF 3 simulations (Fig. 2b, c). The first is a transient

388 response to rapid warming (day 12), which causes ΔAr to increase more than ΔN_2 as a result of
389 the greater SST-dependent solubility of Ar (Fig. S1a). Subsequently, as SST stabilizes, and/or
390 ventilation rates increase, the sign of $\Delta N_2/Ar$ reverses (i.e. $\Delta N_2 > \Delta Ar$; days 20-65), as Ar re-
391 equilibrates more rapidly via diffusive air-sea exchange (Fig. S1c). Conversely, $\Delta N_2/Ar$ can
392 increase transiently following rapid cooling (Fig. 2b, days 65-68), before air-sea exchange
393 effects dominate once again to produce values lower than stead-state conditions. This response is
394 attributable to the greater cooling-induced increase in Ar solubility, followed by faster Ar re-
395 equilibration (Fig. 2b, >day 68), resulting in $\Delta Ar > \Delta N_2$ and potentially negative $\Delta N_2/Ar$.

396   Temperature effects can persist for long time-periods if air-sea exchange is weak (Fig.
397 2b-d; >day 75) or if SST continues to change steadily. Notably, rapid warming (cooling) will not
398 always produce transiently negative (positive) $\Delta N_2/Ar$, as the resulting gas perturbation depends
399 on the magnitude of ΔSST, prior gas conditions, and other gas fluxes (e.g. vertical mixing;
400 section 3.1.2). For example, during the second warming event in Ex-IF3 (Fig. 2c, day 65)
401 $\Delta N_2/Ar$ remains positive, but decreases, since prior values were near the u_{10}-dependent quasi-
402 steady-state condition. This scenario may be more likely in real conditions, as $\Delta N_2/Ar$ is often
403 positive in oceanic surface waters (see section 3.2 below).

404   In simulations conducted with partial ice cover (50 %; Ex-IC), the presence of ice
405 dampened u_{10} effects and accentuated SST controls on gas saturation states (Fig. 2d). The effects
406 of ΔSST persisted for significantly longer in ice-covered conditions due to reduced ventilation
407 rates. Moreover, gases approached 100 % saturation, rather than the bubble-induced
408 supersaturation states (grey line in Fig. 2d). The exact response depends on the gas exchange
409 model employed and the fraction of ice cover but a sensitivity analysis with different gas
410 exchange parameterizations (Butterworth & Miller, 2016; Islam et al., 2016; Loose et al., 2014)
411 produced the same general results, albeit with slightly variable re-equilibration times (not
412 shown). Our results thus reproduce the expected effects of sea ice dampening of gas exchange,
413 and the persistence of gas disequilibria caused by other physical factors (DeGrandpre et al.,
414 2020; Manning et al., 2017). The suppression of bubble effects under ice-covered conditions
415 (Nilsson et al., 2001) reflects the reduction in sea states and wave breaking activity (Liang et al.,
416 2017; Voermans et al., 2019; Woolf & Thorpe, 1991). Under partial or full ice-cover, other
417 physical processes are therefore more significant in generating mixed layer $\Delta N_2/Ar$ disequilibria
418 (see section 3.2). These results demonstrate the potential impact of sea ice dynamics in driving
419 O_2, Ar and N_2 saturation anomalies. Future work should characterize the contributions of ice
420 formation or melt to $\Delta O_2/Ar$ and $\Delta O_2/N_2$ deviations.

421
422

423
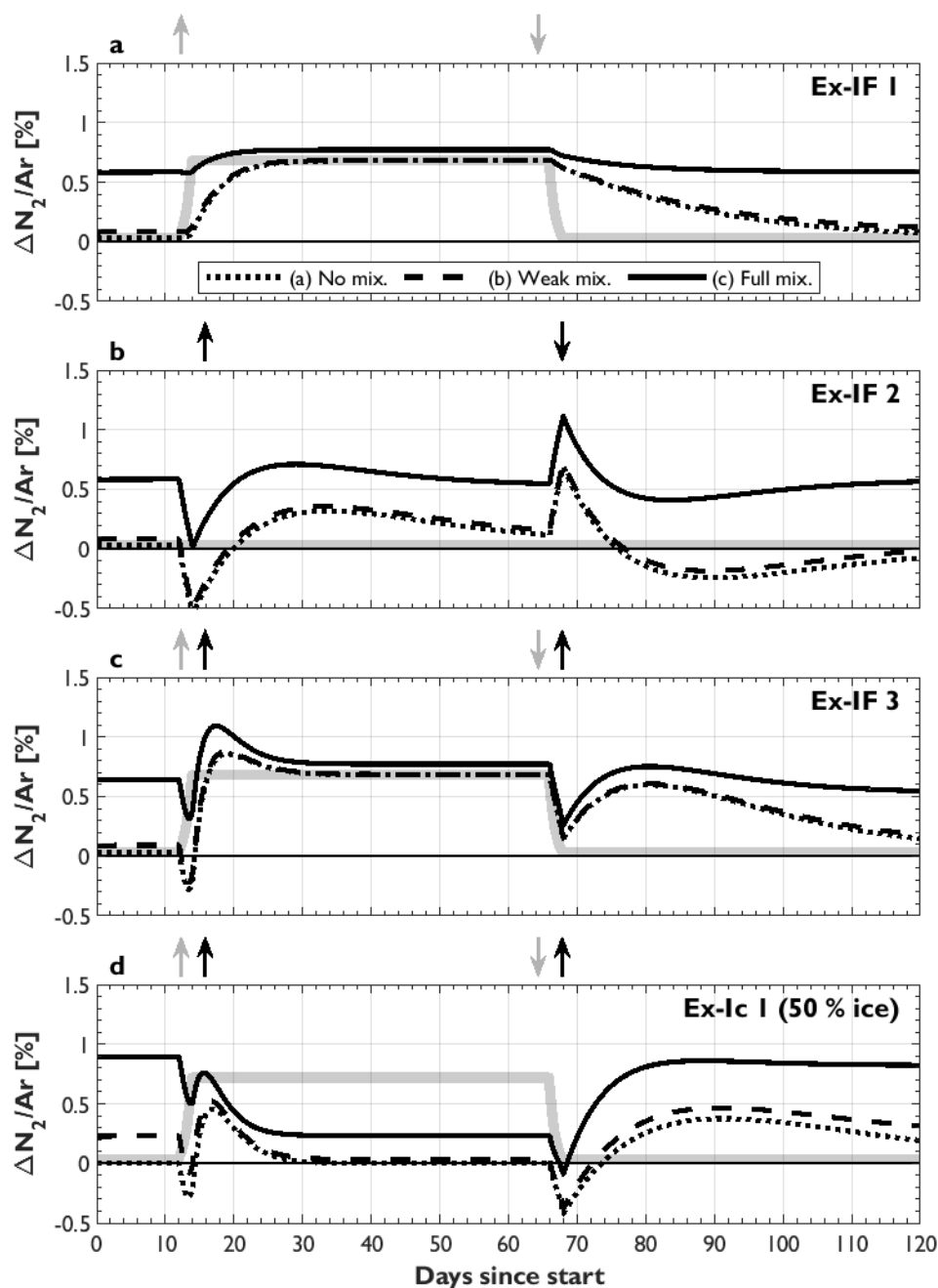
Figure 2. Results from model simulations showing derived $\Delta N_2/Ar$ under different experimental perturbations. The three black lines in each panel represent the different mixing scenarios (described in panel a), and the thick light grey lines depict expected steady-state $\Delta N_2/Ar$ values resulting from bubble-induced supersaturation in each model run (grey lines in Fig. 1). Arrows above the panels represent step changes of increasing (up arrow) or decreasing (down arrow) wind speed (light grey) and SST (black). Details of imposed experimental conditions are presented in Table 1. The first three panels present simulations for ice-free conditions, while the bottom panel presents results with simulations containing 50% ice cover.

432

433   3.1.2 The role of vertical mixing

434   The results from our simulations excluding vertical mixing (run a) are consistent with
435 Hamme & Emerson (2002) who demonstrate the first-order control of temperature changes and
436 bubble-mediated gas exchange in controlling surface inert gas conditions. However, our
437 simulations including mixing processes (runs b, c) highlight the key role of mixing in altering
438 surface $\Delta N_2/Ar$. For example, vertical mixing of water parcels with different temperatures can
439 induce supersaturation in O_2, Ar and N_2 due to the non-linear temperature-dependence of gas
440 solubility (Fig. S1; Hamme et al., 2019; Ito & Deutsch, 2006). Since temperature effects on O_2
441 and Ar are nearly identical, surface $\Delta O_2/Ar$ will be largely insensitive to mixing if subsurface gas
442 anomalies are negligible (i.e. subsurface $\Delta O_2/Ar$ near 0 %). However, throughout most of the
443 ocean, waters below the mixed layer are depleted in O_2 so that surface $\Delta O_2/Ar$ and $\Delta O_2/N_2$ will
444 be negatively biased in regions of active vertical mixing (see below; Izett et al., 2018; Teeter et
445 al., 2018). Moreover, decoupling between surface $\Delta O_2/Ar$ and $\Delta O_2/N_2$ will occur through mixing
446 of water masses with differing temperatures (or salinities, to a lesser-degree) as a result of the
447 lower temperature-sensitivity of N_2 solubility (Fig. S1a), or from mixing of water parcels with
448 subsurface $\Delta N_2/Ar$ not equal to 0 % (as observed throughout most of the ocean; Shigemitsu et
449 al., 2016).

450   These mixing effects are represented in our model simulations, where weak vertical
451 fluxes (run b; dashed lines in Fig. 2) lead to only minor deviations in surface $\Delta N_2/Ar$ from the
452 bubble-induced value (compare dotted, dashed and grey lines in Fig. 2). Conversely, higher
453 mixing fluxes (run c) may result in significantly elevated $\Delta N_2/Ar$. As predicted by our quasi-
454 steady-state analyses (Fig. 1), surface $\Delta N_2/Ar$ in simulations including mixing is weighted
455 between end members represented by the bubble-induced supersaturation ratio of N_2 and Ar, and
456 $\Delta N_2/Ar_{deep}$. The resulting mixed layer value depends on the relative influence of air-sea exchange
457 (i.e. k_T) and vertical mixing (κ/dZ). At low wind speeds or high mixing rates, surface $\Delta N_2/Ar$ is
458 closer to $\Delta N_2/Ar_{deep}$ (Fig. 2; days <12 and >68) and potential deviations from the bubble-induced
459 steady-state value can exceed ~2 % (Fig. 1c). In contrast, at higher u_{10} (Fig. 2a, c; days ~12-65)
460 or low κ, air-sea exchange fluxes drive surface $\Delta N_2/Ar$ towards the bubble-induced
461 supersaturation value, thus minimizing the effect of mixing fluxes.

462   While mixing can produce large $\Delta N_2/Ar$ anomalies, the results from Ex-IF 2-4
463 demonstrate that the effects of rapid ΔSST and sea ice coverage are similar, regardless of the
464 mixing scenario. Specifically, mixing shifts the baseline in $\Delta N_2/Ar$, but the transient responses to
465 ΔSST in Ex-IF 2 are similar in all mixing scenarios. Similarly, as sea ice dampens the wind
466 effect, strong mixing caused surface $\Delta N_2/Ar$ to approach $\Delta N_2/Ar_{deep}$ rather than the bubble-
467 induced supersaturation state.

468   Throughout most of the ocean, the rate of air-sea exchange will typically exceed turnover
469 via mixing (k_T >3.3 m d^{-1} at wind speeds >7 m s^{-1} and canonical κ_z, 10^{-4} m^2 s^{-1}; Cronin et al.,
470 2015; Whalen et al., 2012). This implies that mixing can cause baseline shifts in surface $\Delta N_2/Ar$
471 (Figs. 1-4), but that elevated wind events should still dominate on short time-scales, as observed
472 in our experimental simulations (Ex-IF 1,3 and Ex-IC). Nonetheless, vertical mixing remains
473 important in decreasing the re-equilibration timescale of mixed layer gas anomalies. When κ is
474 high, gas residence times are reduced, more rapidly erasing any potential bubble-induced
475 supersaturation effects. The analytical solution to our simplified MLD budget is useful for

476 diagnosing this effect as κ appears in the exponential term of the solution (Eq. 5), and therefore
477 influences the rate constant of gas re-equilibration. Our definition of τ_{O2} (Eq. 6), the O_2 re-
478 equilibration time-scale over which N_2' calculations are performed (see sections 2.2, 3.4.1 and S1
479 in the SI), also includes the mixing coefficient κ.

480
$$\tau_{O2} = \frac{-\ln{(0.01)} \cdot \text{MLD}}{\left(k_T + \frac{\kappa}{\text{dz}}\right)}$$
(6)

481

482 3.2 Realistic simulations

483 The main processes driving variability in $\Delta N_2/Ar$ in our experimental runs are also
484 apparent in the realistic simulations (real-OSP in Fig. 3, and real-BB in Fig. 4). Under the more
485 realistic scenarios, however, SST and differential gas exchange rates exerted the strongest
486 controls on $\Delta N_2/Ar$ over long time-scales. Indeed, in both the real-OSP and real-BB simulations,
487 ΔAr and ΔN_2 followed seasonal changes in SST, with transient modifications during periods of
488 elevated wind-speeds (Figs. S4, S5). The OSP and Baffin Bay runs without mixing generally
489 resemble the results of experiment Ex-IF 2a (ΔSST at constant u_{10}). The elevated spring and
490 summertime $\Delta N_2/Ar$ in both sets of runs (days ~155-255 and ~520-620 in real-OSP, Fig 3; and
491 days ~190-230 in real-BB, Fig. 4) is consistent with increased gas supersaturation states, and the
492 slower re-equilibration rate of N_2 over Ar following positive ΔSST. In the real-OSP run without
493 mixing (run a), a net warming of ~9 $^{\circ}$C during the spring and summer caused $\Delta N_2/Ar$ to increase
494 to ~0.4 % (corresponding with ΔN_2 and ΔAr increases to ~3 %; Figs. S4, S5). In real-BBa, the
495 equivalent ΔSST raised $\Delta N_2/Ar$ to ~0.8 % (ΔN_2 and ΔAr increase to ~11 %; Fig. S5). These
496 positive $\Delta N_2/Ar$ values, which exceed the quasi-steady-state conditions (thick gret lines in Figs.
497 3, 4), thus reflect seasonal warming. During conditions of elevated u_{10} and net cooling (days
498 ~260-400 and >~620 in real-OSP and >day 250 in real-BB), the decline in $\Delta N_2/Ar$ is again more
499 consistent with temperature-dependent solubility effects, with short-term modifications by
500 bubble processes. In these realistic scenarios, the decline in $\Delta N_2/Ar$ during cooling periods
501 resembled the response in Ex-IF 2 (i.e. decreased $\Delta N_2/Ar$; Fig. 2b, c).

502 As observed in the experimental runs, the real-OSP and real-BB simulations also
503 demonstrated a mixing effect on gas conditions, with vertical fluxes elevating surface gas
504 anomalies, particularly during autumn and winter periods. The mixing effect on $\Delta N_2/Ar$ was
505 most significant at higher κ, during MLD deepening (Figs. 3c, 4c), or under sea ice cover (Fig.
506 4b), when $\Delta N_2/Ar$ approached $\Delta N_2/Ar_{deep}$. In the full mixing runs of both realistic simulations,
507 $\Delta N_2/Ar$ was almost always higher than in the non-mixing runs. Exceptions occurred during
508 periods of reduced summertime mixing in real-OSP (annotated in Fig. 3) when $\Delta N_2/Ar$ was
509 equivalent in both mixing scenarios (and in all sensitivity model runs; see section 3.3), and
510 between days 220 and 240 in real-BB, when mixing dampened the warming effect. Ultimately,
511 seasonal variability in the mixing respone will be sensitive to intra-annual variability in u_{10},
512 $\Delta N_2/Ar_{deep}$ and κ_z, which we attempted to capture in our real-OSP simulations (Table 1).

513 In contrast to the experimental runs, $\Delta N_2/Ar$ in the realistic simulations seldom achieved
514 the quasi-steady-state condition (grey lines in Figs. 3, 4 predicted by Eq. 5). This reflects the
515 high variability in environmental forcing, and the fact that thermal disequilibrium can persist for
516 long periods (up to 60 days in our experimental simulations) under low wind speeds. This result
517 demonstrates the simultaneous effects of various fluxes on gas saturation states. Only under

518   conditions of significant ice cover and high mixing does $\Delta N_2/Ar$ remain near to the steady state
519   values.
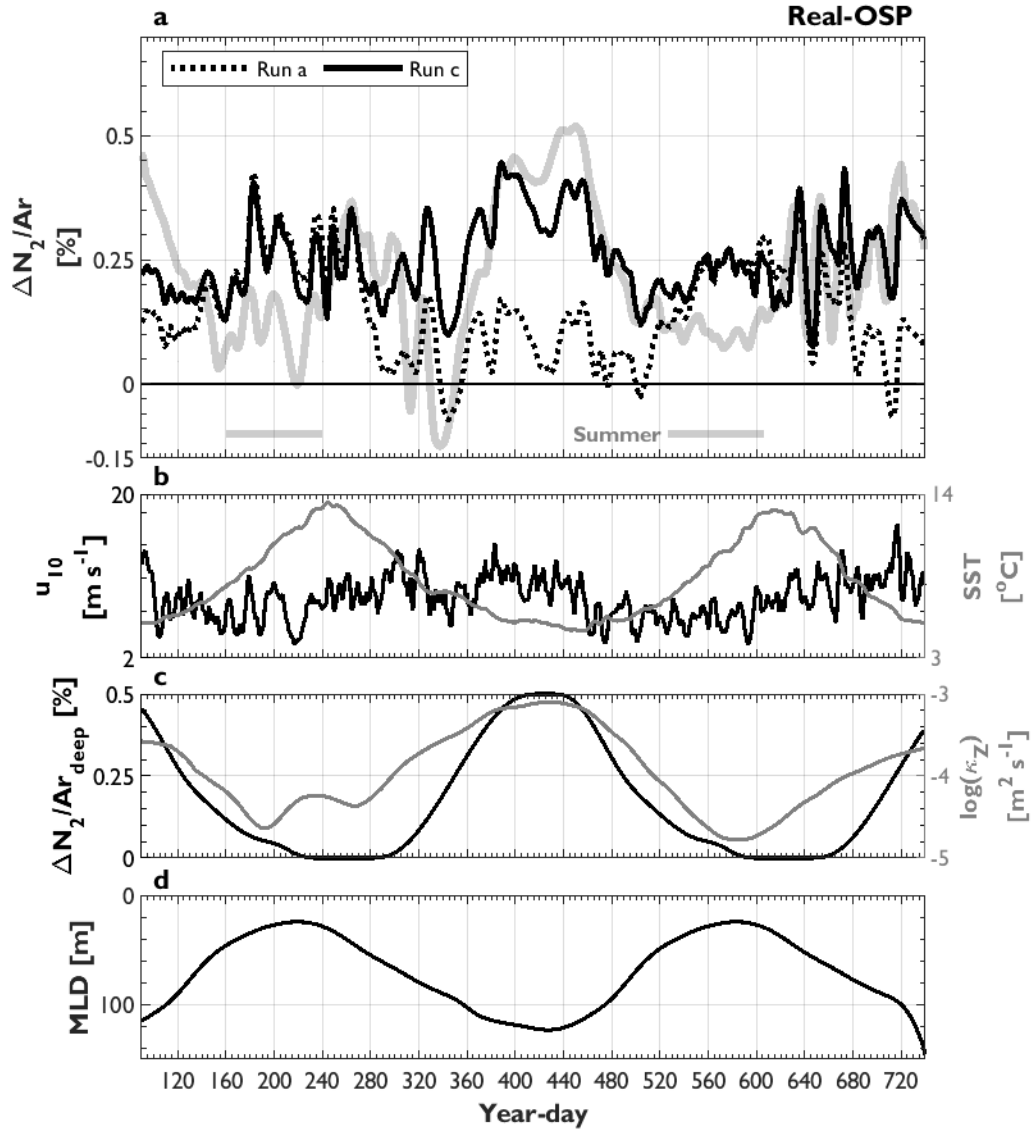
520

521   **Figure 3.** Results from realistic model simulations of OSP in the Subarctic Northeast Pacific.
522   Panel (a) shows $\Delta N_2/Ar$ in runs without (run a; dotted lines) and with (run c; solid lines) mixing,
523   while panels (b)-(d) represent the forcing environmental data (details in Table 1). The x-axes
524   represent the 2011 year-day (Jan. 2011 – Jan. 2013). The thick grey line in (a) depicts the quasi-
525   steady-state condition (Eq. 5; Fig. 1) corresponding with run c. The grey bars in (a) (labelled
526   "summer") represent periods of weak mixing between June and September, and correspond with
527   data shown in Fig. 6.
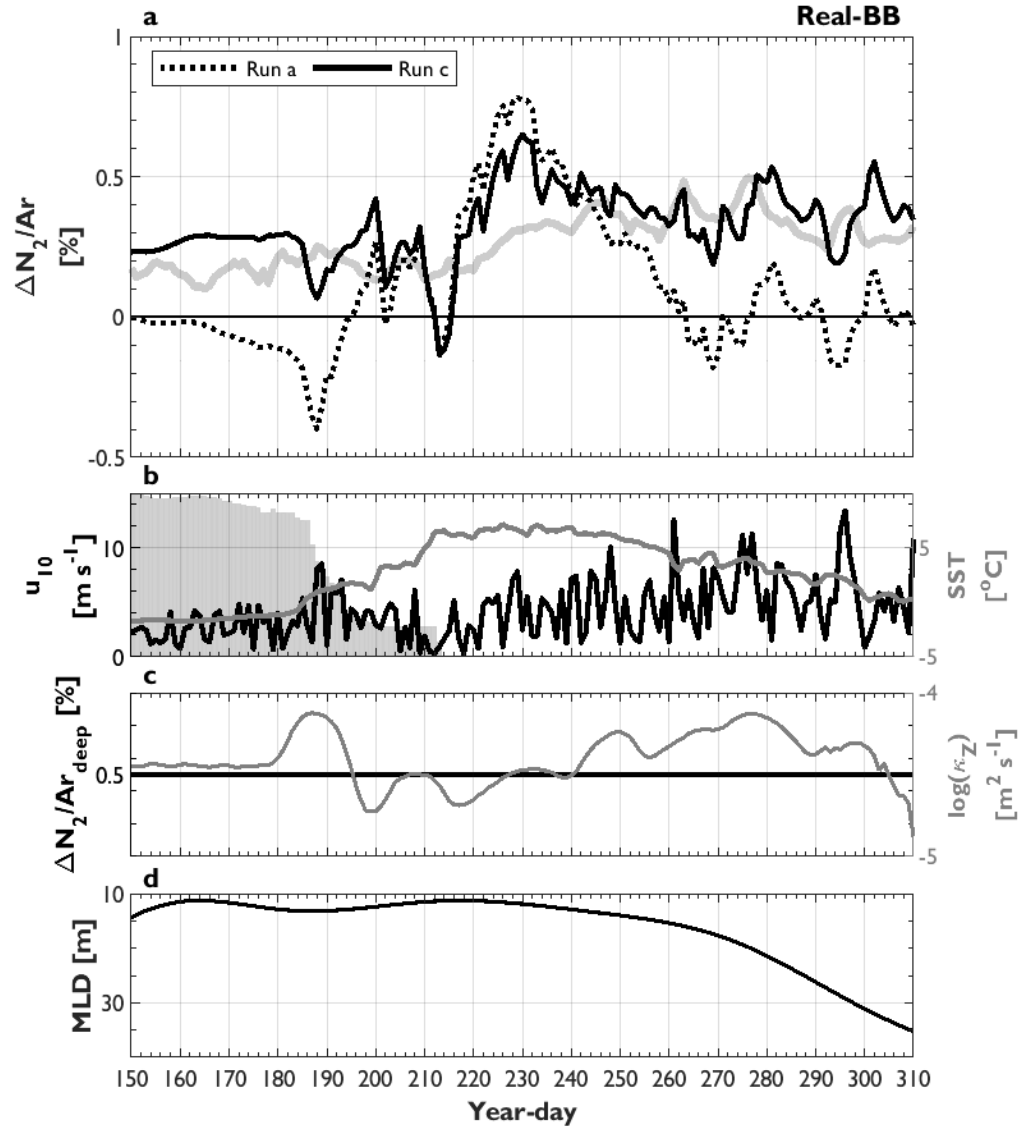
Figure 4. Results from realistic model simulations of Baffin Bay in the eastern Arctic. The x-axes represent the 2019 year-day (May – Oct.). The grey shading in (b) represents the ice-coverage as a percent of the figure y-scale. Refer to Fig. 3 caption and Table 1 for details.

### 3.3 Model validation and sensitivity tests

To validate our modelling approach in support of the subsequent N_2' analysis (section 3.4.1), we compared N_2 and O_2 from our real-OSP run c simulation against a two-year cycle of surface measurements from the NOAA PMEL OSP mooring (provided by S. Emerson at https://www.nodc.noaa.gov/ocads/oceans/Moorings/Papa_145W_50N.html; Emerson et al., 2017). As shown in Fig. 5a, b, our model calculations forced with relevant environmental data and time-variable mixing terms agree well with the mooring gas data. The model is able to reproduce both short-term (associated with wind events) and long-term (associated with seasonal

541   SST and mixing variability) responses of N_2 to environmental drivers, with an overall root mean
542   square error (RMSE) between the model and data of 1.0 % (range of offset between modeled and
543   observed N_2 ~0 – 2.4 %). Moreover, our modelled O_2, which was forced with a mean annual
544   NCP time-series and subsurface O_2 observations at OSP, recaptures the observed annual cycle
545   with equally-small deviation from the in-situ time-series (RMSE = 1 %; range 0 – 3.1 %).

546   Residual differences between the model and observations can be explained by several
547   factors, including the potential effects of lateral advection (Emerson & Stump, 2010), which are
548   neglected in our calculations, and the smoothed mixed layer and mixing forcing conditions
549   applied in our model runs. In addition, interpolation of sparse ΔAr_{deep} and $\Delta N_2/Ar_{deep}$
550   observations from discrete gas sampling at OSP (February, June and August data from Hamme
551   et al., 2019) may not fully represent subsurface conditions across the full seasonal cycle. Indeed,
552   the poorest alignment between model and observed ΔN_2 occurs during the fall and early winter
553   (e.g. days ~260-390), when no subsurface gas observations were available. Moreover, while we
554   applied κz values corresponding with the location and timing of our model setting (from Cronin
555   et al., 2015), it is also possible that uncertainty in the κz dataset may contribute to differences
556   between the model and observed gas data. Importantly, however, the model run with realistic
557   mixing fluxes was able to better replicate the full seasonal cycles of N_2 and O_2 than the
558   simulation run without mixing (light grey line in Fig. 5a,b). Indeed, the model run without
559   mixing often under-estimates ΔN_2, demonstrating the importance of vertical mixing in supplying
560   relatively high-N_2 to surface waters.

561   We tested the model sensitivity to flux parameterizations by performing additional
562   simulations in which the mixing terms (κz, dZ, entrainment) and bubble scaling coefficient (β)
563   were modified from the real-OSP full mixing run (Fig. 5c). Overall, we find that the model skill
564   at reproducing observed N_2 at OSP is most sensitivie to the exclusion of bubble processes and
565   vertical flux terms. This result is consistent with other studies (e.g., Emerson et al., 2019;
566   Emerson & Bushinsky, 2016; Hamme & Severinghaus, 2007), which noted that exlplict bubble
567   flux terms are required to explain gas observations. Moreover, we find that the model sensitivity
568   is greater in the wintertime at OSP. This reflects the reduced significance of bubble fluxes and
569   vertical mixing during summer months, as a result of lower wind speeds and upper ocean
570   turbulence. The weak sensitivity of the model to parameterizations in the summer months is a
571   key result as it supports the application of the present approach during time-periods when NCP
572   and carbon export are typically elevated, and when in-situ sampling from research vessels is
573   most common. Indeed, results vary by less than 0.25 % across all modified simulations between
574   June and August, as compared with deviations exceeding 1 % in winter periods.

575   Based on the comparisons of modeled and observed N_2, we believe that our model
576   captures the main drivers of N_2 saturation variability in oceanic surface waters, particularly
577   during biologically-productive summer months. Although the model cannot be equally-validated
578   for Ar due to a lack of observations, we expect that our conclusions apply to this gas as well.
579   This exercise should also be taken as a rough validation of the Liang et al. (2013) bubble-flux
580   parameterization, which was previously evaluated in the North Pacific by Emerson & Bushinsky
581   (2016) using a similar model as that employed here. Importantly, the strong agreement between
582   our model results and observations over a two-year cycle justifies the air-sea flux and mixing
583   parameterizations used in our model simulations, and provides confidence in the N_2' approach
584   described below.

585
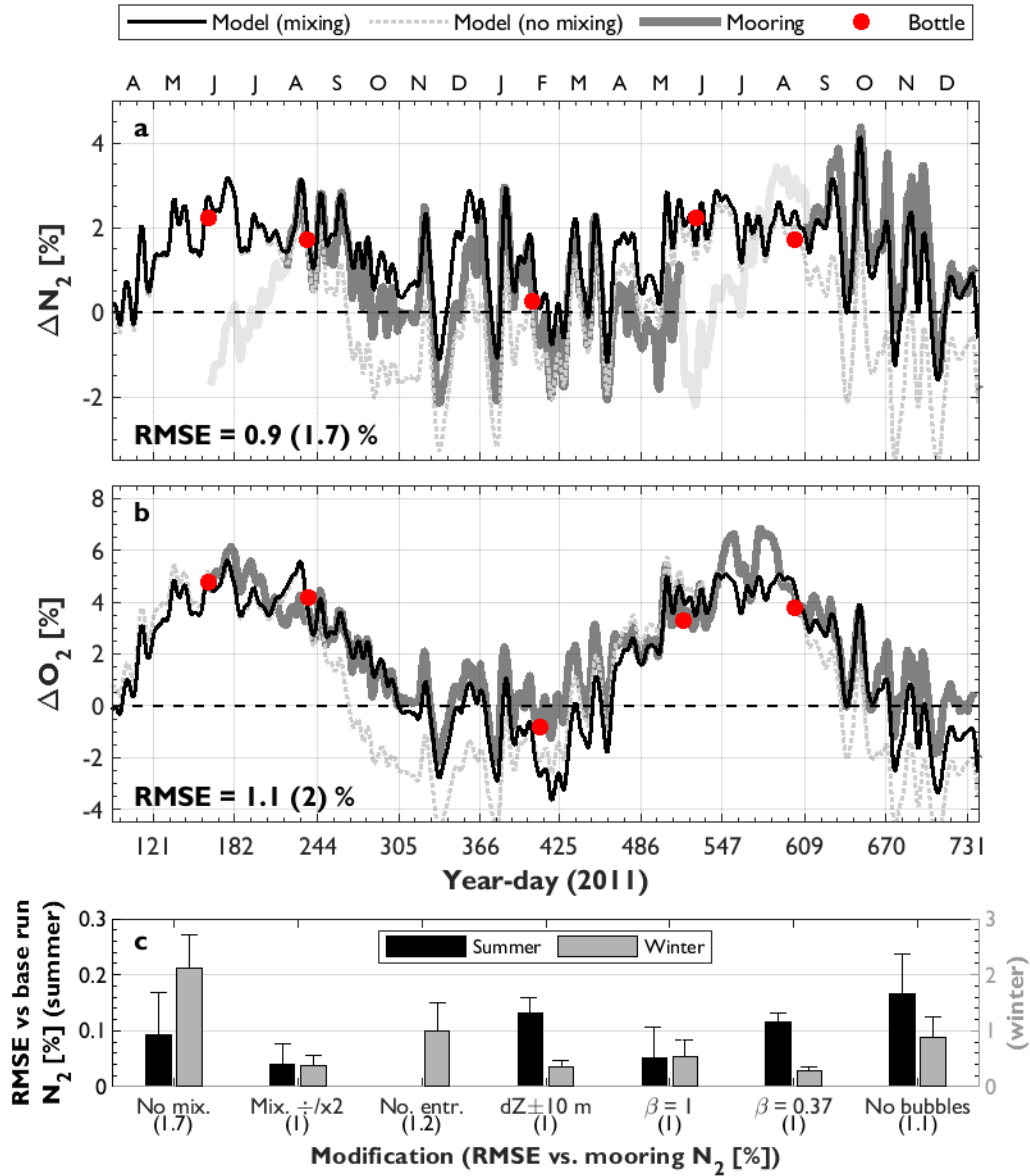
Figure 5. A comparison of modeled (thin lines) and observed (thick grey line) N_2 (a) and O_2 (b) supersaturation anomalies over a two-year cycle at OSP in the Subarctic Northeast Pacific. The modelled gas results are from the full mixing (run c; black line) and no mixing (run a; light grey line) real-OSP simulations and correspond with results and forcing parameters presented in Fig. 3 and Table 1. Gas observations were obtained from the NOAA PMEL mooring at OSP. The light, thick-grey section of the mooring N_2 time-series in (a) represents a section of the record where the N_2 data may be biased by sampling artifacts (S. Emerson personal communication, 2020). All lines represent 1-day smoothed values. The red dots in (a) and (b) represent discrete observations. The N_2 data (a) are mean February, June and August N_2 values from Hamme et al. (2019), and O_2 data (b) are from Rosette sampling at the specified times. The RMSE values presented at the top-right represent differences between modelled and mooring values for real-OSP run c (run a value in brackets). Values on the x-axis correspond with 2011 year-day, and labels at the top represent month. Panel (c) represents a sensitivity analysis on our model

600 parameterizations where the real-OSP with full mixing simulation ($\beta = 0.5$ and dZ = MLD to
601 thermocline depth) was modified as indicated by the labels on the x-axis. The model sensitivity
602 was evaluated during summer (July-Aug.; left axis) and a winter (Nov.-Feb.; right axis)
603 segments. The bars represent the mean difference between the base and modified runs during
604 these segments, with error bars depicting the range of values. The numbers below the x-axis
605 labels are the overall RMSE between each modified model run and the real mooring N_2 data
606 from OSP. Note that the summer sensitity results are represented by the left y-axis, which is a
607 factor of 10 smaller than the scale on the left axis, representing the winter results.

608

609   3.4 NCP calculations from O_2 and N_2 measurements

610   Divergence between mixed layer $\Delta O_2/Ar$ and $\Delta O_2/N_2$ (non-zero $\Delta N_2/Ar$) can lead to
611 significant uncertainty in NCP estimates calculated from O_2 and N_2 observations. For a realistic
612 range of ΔO_2 and $\Delta N_2/Ar$ in the ocean, absolute differences between $\Delta O_2/Ar$ and $\Delta O_2/N_2$ may
613 exceed 2 % (Fig. S6a), which is of the same magnitude as ΔO_2 observed in many low
614 productivity ocean regions. Relative differences between NCP tracers can exceed 100 % for low
615 ΔO_2, and will likely be significant over a large range of ocean conditions (Fig. S6b). These
616 biases will propagate as errors in NCP estimates derived from observations of the biological O_2
617 saturation anomaly calculated following Kaiser et al., (2005):

618          $$NCP = k_{O_2} \cdot \Delta O_2/N_2 \cdot [O_2]_{eq} \tag{7}$$

619 Over a realistic range of SST (0-30 ^{o}C), salinity (30-35 PSU) and u_{10} (2-10 m s^{-1}), a bias in
620 $\Delta O_2/N_2$ of 0.3 % (the mean value of $\Delta O_2/Ar – \Delta O_2/N_2$ in our realistic simulations; Table S1)
621 would introduce ~6 mmol O_2 m^{-2} d^{-1} error in NCP estimates, while a bias of 1.1 % (the upper
622 range in our simulations) would contribute up to ~19 mmol O_2 m^{-2} d^{-1} uncertainty. These errors
623 may be comparable to those resulting from diel O_2 variability (up to ~5 to >100 mmol O_2 m-2 d-
624 1; Wang et al., 2020) and vertical mixing of subsurface O_2-deplete waters (~0-50 and 60-190
625 mmol O_2 m^{-2} d^{-1} in offshore and coastal waters, respectively; Izett et al., 2018), depending on the
626 ocean region sampled. However, the differences between $\Delta O_2/Ar$ and $\Delta O_2/N_2$ in our realistic
627 simulations are almost as large in magnitude as reported $\Delta O_2/Ar$ values in many offshore regions
628 of all ocean basins, which are typically smaller than ~$\pm$5-10 % (e.g. Eveleth et al., 2014, 2017;
629 Giesbrecht et al., 2012; Hamme & Emerson, 2006; Izett et al., 2018; Juranek et al., 2019;
630 Lockwood et al., 2012; Munro et al., 2013; Palevsky et al., 2016; Ulfsbo et al., 2014; Wang et
631 al., 2020). Thus, biases in the quantification of the biological O_2 saturation anomaly could lead to
632 erroneous interpretations of NCP estimates from $\Delta O_2/N_2$ measurements and, in some regions,
633 false conclusions regarding the metabolic status of surface waters (i.e. implied net heterotrophy
634 from negative $\Delta O_2/N_2$ versus autotrophy from positive $\Delta O_2/Ar$; represented by outlined region in
635 Fig. S6). These limitations motivate the need to correct $\Delta O_2/N_2$ observations for excess physical
636 N_2 saturation, particularly in offshore waters where other biases are smaller.

637   Fortunately, our analyses demonstrate that differences between $\Delta O_2/Ar$ and $\Delta O_2/N_2$
638 respond systematically to differential physical gas fluxes and environmental perturbations,
639 enabling us to apply appropriate corrections. We thus derived a new term, N_2' (calculations
640 described in section 2.2 and software scripts provided at doi.org/10.5281/zenodo.4024952),
641 which holds significant value as a tracer for physically-induced changes in the mixed layer O_2.
642 As we discuss below, $\Delta O_2/N_2'$, derived from Optode (O_2) and GTD (N_2) measurements and

643 calculations from a simplified MLD budget, provides a good analog for $\Delta O_2/Ar$-based NCP
644 estimates.

645

646   3.4.1. N_2' in mixed layer model setting

647   We tested the performance of our N_2' approach using the experimental and realistic
648 simulations (Figs. 2-4). We treated the simulated gas values as "true" (i.e. analogous to in-situ
649 ocean observations; see Eq. 4) and applied the N_2' approach based on readily-available data from
650 reanalysis products or field observations. In deriving $\Delta N_2'$, we thus applied the same
651 environmental forcing data (SST, u_{10} and SLP) as in the full model simulations, but assumed
652 constant values backwards in time for MLD, surface salinity, κ, and $\Delta N_2/Ar_{deep}$, to mirror the
653 information available from field studies (see below, section 3.4.3).

654   Overall, N_2' successfully corrects for differences in surface water ΔAr and ΔN_2, thereby
655 reducing biases between $\Delta O_2/Ar$ and $\Delta O_2/N_2$ (Fig. 6). Across all experimental simulations,
656 median $\Delta N_2'/Ar$ was ~0 % and ~0.01 in the runs without (a) and with (c) mixing, respectively. In
657 comparison, uncorrected $\Delta N_2/Ar$ was significantly larger than 0, with median values of 0.23 and
658 0.63 % (maximum 1.1 %). In the realistic simulations, median $\Delta N_2'/Ar$ and $\Delta O_2/Ar - \Delta O_2/N_2'$
659 were ~0.01 (range -0.24 to 0.3 %; Fig. 6, Table S1), demonstrating that differences between
660 $\Delta O_2/Ar$ and $\Delta O_2/N_2$ can be corrected using simple MLD budget computations performed over an
661 estimated O_2 re-equilibration time (Eq. 6).

662   The remaining $\Delta N_2'/Ar$ disequilibria is attributable to the simplifying assumptions in the
663 N_2' approach, which we discuss in section 3.4.3. We observed the largest remaining biases in
664 $\Delta N_2'/Ar$ during the summer period of the real-BB full mixing simulation (Fig. S9b). These
665 relatively large remaining offsets between $\Delta N_2'$ and ΔAr resulted from significant temporal
666 variability in subsurface gas concentrations in the BB simulations, which cannot be represented
667 in N_2' calculations (see sections 2.1.1, 3.4.3 and S2.2 for details). However, we believe that these
668 biases represent the upper limit of values expected from application of the present approach to
669 real data sets, as subsurface gas conditions are likely to vary less in reality than in our model.
670 Additional remaining biases in $\Delta N_2'/Ar$ occured during the autumn months of the real-OSP full
671 mixing scenario when vertical entrainment was significant (~days 230-330 and >600 in Fig.
672 S9a), and in early summer (~days 160-200 and ~525-565) when the N_2' budget was unable to
673 resolve the relatively strong mixing occurring prior to this time. Despite these offsets, N_2' is
674 useful in reducing differences between $\Delta O_2/Ar$ and $\Delta O_2/N_2$ observations, and $\Delta N_2'/Ar$ was
675 almost always lower than $\Delta N_2/Ar$ in all of our simulations.

676   Given the sparsity of oceanic mixing rate estimates (e.g. Whalen et al., 2012) or
677 subsurface Ar and N_2 measurements (e.g. Hamme et al., 2019), it may be difficult to constrain
678 the mixing flux terms in our N_2' model (see below, sections 3.4.2 and 3.4.3). We therefore
679 performed an additional set of N_2' calculations to test our approach when vertical mixing fluxes
680 are neglected. This term, which we denote as $\Delta N_2'$(no mix.), was derived by setting κ to 0 $m^2 s^{-1}$
681 in the N_2' calculations. We find that $\Delta N_2'$(no mix.)/Ar does not fully correct for differences
682 between $\Delta O_2/Ar$ and $\Delta O_2/N_2$ in most simulations (Fig. 6). However, in a subset of real-OSP run
683 c corresponding with mid-June to September (labelled bars in Fig. 3), N_2'(no mix.) successfully
684 reduced $\Delta N_2'/Ar$ to a median value of ~0.04 %. This result is promising for in-situ applications in
685 stratified ocean regions, when vertical mixing is small relative to other gas flux terms.
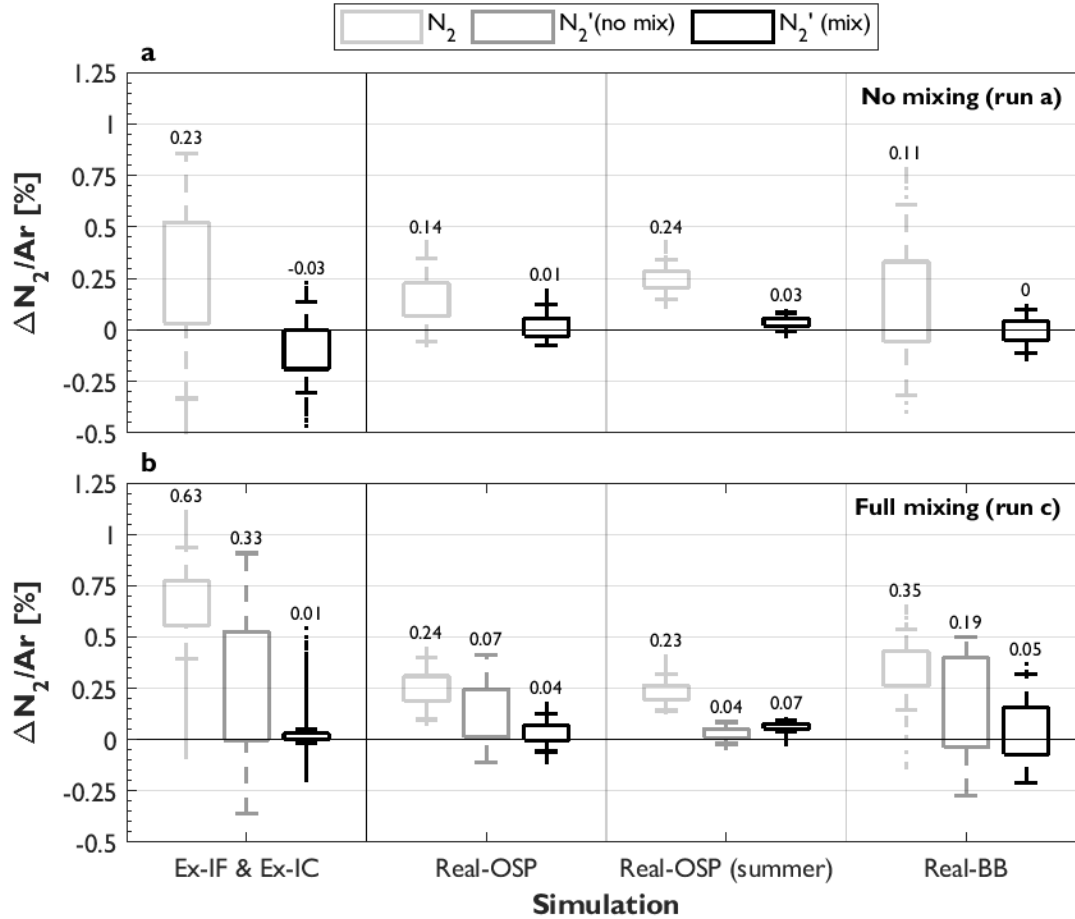
Figure 6. Distribution of $\Delta N_2/Ar$ and $\Delta N_2'/Ar$ in the experimental (left) and realistic (right) simulations runs without mixing (run a) and with mixing (run c) (details in Table 1). The numbers above each box represent the median $\Delta N_2/Ar$ or $\Delta N_2'/Ar$ values. A value of zero implies that N_2' provides a perfect analog for Ar. A subset of the OSP simulation is included to represent results in more stratified waters during summer months in the Subarctic Northeast Pacific (highlighted in Fig. 3a).

3.4.2 $\Delta O_2/N_2'$ as an in-situ NCP tracer

Our work demonstrates that $\Delta O_2/N_2'$ offers a robust analog for $\Delta O_2/Ar$ measurements. Indeed, we found that $\Delta O_2/N_2'$ performed significantly better than either ΔO_2 or uncorrected $\Delta O_2/N_2$ in reproducing $\Delta O_2/Ar$. As shown in Fig. 7, $\Delta O_2/N_2'$ was tightly correlated to $\Delta O_2/Ar$, with a linear regression slope that was not significantly different from unity, and an RMSE of 0.03 %. This result suggests that NCP calculations based on $\Delta O_2/N_2'$ should be nearly-equivalent to $\Delta O_2/Ar$-derived estimates, providing an alternative approach to isolate biological influences on mixed layer oxygen dynamics. Moreover, we have observed strong coherence between $\Delta O_2/Ar$ and $\Delta O_2/N_2'$ in observations obtained from underway ship-board surveys across broad spatial scales and hydrographic gradients (manuscript in preparation).

704   Field-based application of the N_2' approach will depend on proper characterization of
705   environmental histories and mixing environments. Quantification of the mixing terms, κ and
706    $\Delta N_2/Ar_{deep}$, will likely constitute the largest source of uncertainty in $\Delta O_2/N_2'$ (see section S2 of
707   the SI), as these values are generally poorly constrained by limited observations and strong
708   spatial or temporal variability. Recent work has provided several approaches to approximating κ
709   from direct or indirect estimates of turbulent dissipation rates (Chanona et al., 2018; Scheifele et
710   al., 2018; Whalen et al., 2012), and by proxy relationships with temperature and salinity (Cronin
711   et al., 2015), nitrous oxide (Izett et al., 2018) or inert gas measurements (Ito & Deutsch, 2006). It
712   is also possible to estimate $\Delta N_2/Ar_{deep}$ and κ from archived datasets (e.g. Hamme et al., 2019) or
713   circulation models (e.g. Castro de la Guardia et al., 2019; Shigemitsu et al., 2016). Moreover, as
714   demonstrated in Fig. 1, and in the simulations with weak or no mixing (Figs. 2, 3), vertical fluxes
715   have a relatively small impact on surface $\Delta N_2/Ar$ when mixing rates fall below $\sim 10^{-4}$ m^2 s^{-1}, or
716   when $\Delta N_2/Ar_{deep}$ is less than ~ 0.25 %. Indeed, in our real-OSP and real-BB simulations forced
717   with time-variable and realistic κ_z and $\Delta N_2/Ar_{deep}$, surface $\Delta N_2/Ar$ converged on similar values
718   for both mixing scenarios between days during summer periods, when κ_z was small (Figs. 3, 4).
719   This suggests a negligible contribution of vertical fluxes to surface gas budgets during periods of
720   stratification, consistent with observations of reduced summertime vertical gas fluxes in mid-
721   latitude oceanic waters (e.g. Emerson & Stump, 2010; Izett et al., 2018; Pelland et al., 2018;
722   Plant et al., 2016). The implication of these results is that mixing terms can potentially be
723   neglected in N_2' corrections under conditions of moderate to strong stratification. Such
724   conditions occur over much of the ocean during periods of summer productivity.

725   In dynamic coastal waters where vertical mixing may contribute to a significant
726   divergence between $\Delta O_2/Ar$ and $\Delta O_2/N_2$, particularly in regions of subsurface or benthic
727   denitrification (see below, section 3.4.3), the resulting bias in NCP estimates may be small
728   compared with errors resulting from vertical mixing fluxes of O_2 and diel variability (section
729   3.4). Moreover, if ΔO_2 is elevated (>5 %) by strong biological production, relative differences
730   between $\Delta O_2/Ar$ and $\Delta O_2/N_2$ will remain smaller than the $\sim 20 - 40$ % uncertainty in gas transfer
731   parameterizations (Fig. S6b; Bender et al., 2011; Wanninkhof, 2014). In offshore waters, where
732   ΔO_2 is typically nearer to equilibrium, and other biases in O_2 are small, N_2' corrections will be
733   necessary to minimize errors in NCP calculations. Overall, we conclude that underway $\Delta O_2/N_2$
734   measurements from Optode and GTD sampling, combined with careful application of the N_2'
735   calculations described here, can serve as an effective alternative to $\Delta O_2/Ar$-based NCP sampling
736   across a wide range of oceanic conditions. This approach thus has the potential to significantly
737   increase the spatial and temporal coverage of marine NCP estimates.

738

739
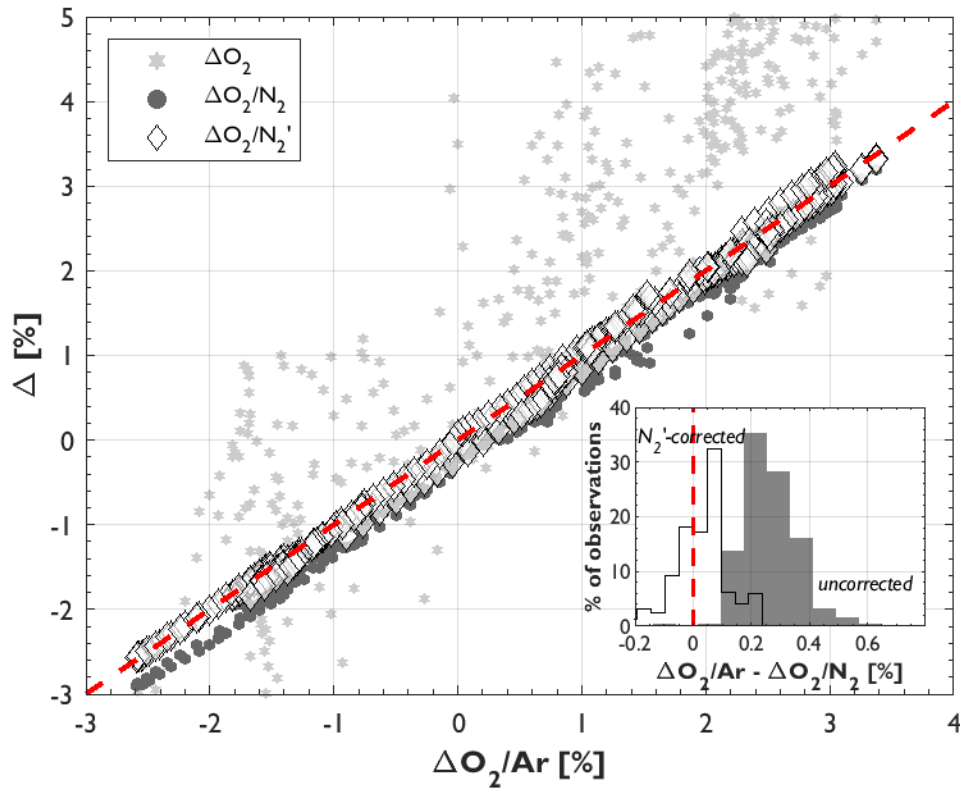
740   **Figure 7.** The relationship between $\Delta O_2/Ar$ and ΔO_2 (light grey stars), $\Delta O_2/N_2$ (dark grey
741   circles) and $\Delta O_2/N_2'$ (black/white diamonds) in the realistic model simulations (real-OSP and
742   real-BB, simulations with full mixing only). The dashed red line shows the 1:1 fit. The inset
743   shows the distribution of $\Delta O_2/Ar - \Delta O_2/N_2$ before (filled grey) and after (outlined) applying N_2'
744   corrections.

745

746   3.4.3 Remaining biases and uncertainty in $\Delta O_2/N_2'$

747   Despite strong the coherence between $\Delta O_2/N_2'$ and $\Delta O_2/Ar$ (Fig. 7), and general
748   agreement of ΔAr and $\Delta N_2'$ some biases remain. These are attributable to the simplifying
749   assumptions in the N_2' calculations (i.e. constant MLD, salinity, κ and $\Delta N_2/Ar_{deep}$), made
750   necessary by the limitation of field observations. The time-history of u_{10}, SST, and SLP prior to
751   ship-board sampling in a given location can be obtained from remote sensing and reanalysis
752   products, but estimates of MLD and salinity are most reliable from ship-board measurements.
753   The subsurface and mixing terms (κ and $\Delta N_2/Ar_{deep}$) may be derived from measurements made at
754   the time of underway gas sampling (see above), but will normally be obtained from external
755   sources and assumed constant over τ_{O2}. Across our realistic simulation runs, we found that the
756   contribution of these simplifying assumptions to uncertainty in $\Delta O_2/N_2'$ was ~0.07 % (Table S1;
757   details in section S2 of the SI), which is small relative to other sources of error in NCP
758   calculations, as discussed above. In general, these errors were largest during times of significant
759   subsurface hydrographic and gas variability, as was the case in our real-BB simulation. While the
760   settings in our BB runs may not be entirely representative of reality, and we were unable to
761   validate the modeled time-series in this location, the N_2' results from these model runs should be

762 seen as upper limits of valus expected from field studies. Errors associated with these
763 assumptions can only be reduced by quantifying the time-variability of the relevant terms, which
764 may be feasible from Argo floats near to cruise track observations, additional reanalysis products
765 or numerical model output.

766   Additional uncertainty in field applications of the N_2' approach arises from the
767 parameterization uncertainty in each of the terms (u_{10}, SST, SLP, F_d, F_C, F_P, β, MLD, κ and
768 $\Delta N_2/Ar_{deep}$) used to predict $\Delta N_2/Ar$ (Eq. 3). To evaluate the magnitude of these errors, we
769 performed a Monte Carlo analysis on the realistic simulations (real-OSP and real-BB, run c only)
770 by randomly varying each of the input variables around their estimated parameter uncertainty
771 (details in section S2 of the SI). We estimated a combined absolute parameterization error in
772 $\Delta O_2/N_2'$ of 0.09 %, with the largest contributions coming from the SST product (Table S1). This
773 is unsurprising given the seasonal controls of SST variability in driving intra-annual variability
774 in gas conditions (see above, sections 3.1-3.2). The bubble terms (F_C, F_P, β) contributed
775 relatively small errors, due to the low prevelance of elevated wind speeds (Figs. 3-4).
776 Calculations of N_2' will, nonetheless, depend on the air-sea exchange model employed in the
777 budget evaluations. We used the bubble-mediated model of Liang et al. (2013) because it has
778 been validated against in-situ N_2 and noble gas measurements (here and in Emerson &
779 Bushinsky, 2016), and was parameterized for weakly-soluble gases similar to O_2. When possible,
780 we recommend that future studies employ air-sea exchange parameterizations that have been
781 validated for the region of interest.

782   An additional consideration is the influence of biological processes on $\Delta N_2'/Ar$. Unlike
783 Ar, N_2 concentrations can be altered by several bacterially-mediated processes, including surface
784 N_2-fixation, and subsurface or sedimentary denitrification and annamox. These processes could,
785 in principle, impact $\Delta O_2/N_2'$-based NCP estimates, but their influence is likely to be small under
786 most conditions. Rates of N_2-fixation are orders of magnitude smaller than air-sea gas fluxes
787 over most oceanic regions, minimizing the influence of this process on $\Delta N_2/Ar$ (Figs. S7, S8). In
788 nitrate-deplete waters of the subtropical and tropical ocean, where N_2-fixation is most important
789 (Deutsch et al., 2007; Gruber & Sarmiento, 1997) the upper range of N_2-fixation rates is ~220
790 mmol N_2 m^{-2} yr^{-1} (~0.6 mmol N_2 m^{-2} d^{-1}). Elsewhere, mean estimates of N_2-fixation in
791 subtropical, temperate and polar waters range from about <0.01 to 0.24 mmol N_2 m^{-2} d^{-1} (Blais et
792 al., 2012; Sipler et al., 2017; Tang et al., 2019, 2020). Net air-sea exchange fluxes almost always
793 exceed the maximum rate of N_2-fixation (Fig. S8), so that any ΔN_2 anomalies produced by
794 biological processes should be rapidly erased at wind speeds above ~3 m s^{-1}. Neglecting the
795 influence of other physical gas fluxes (e.g. vertical mixing), maximum rates of N_2-fixation
796 applied to our model will only induce a quasi-steady-state ΔN_2 anomaly larger than 0.05 % at u_{10}
797 below 6 m s^{-1} (Fig. S8b), which only occurs consistently in a narrow latitude band near the
798 equator. Regardless, periodic elevated sea states should rapidly erase any accumulated N_2
799 deficits (Shigemitsu et al., 2016). Indeed, in an additioanl real-OSP run forced with constant
800 global maximum N_2-fixation rate, simulated ΔN_2 always differend from values in the base run by
801 less than 0.05 %. We thus conclude that N_2-fixation should not have a significant impact on the
802 derivation of N_2', or on $\Delta O_2/N_2'$-based NCP estimates.

803   The influence of denitrification and annamox on surface $\Delta O_2/N_2'$ will also be small and
804 indirect, as these processes elevate $\Delta N_2/Ar_{deep}$ (Deutsch et al., 2007; Gruber & Sarmiento, 1997;
805 Kana et al., 1998; Tortell, 2005), but do not alter surface N_2 directly. Their contribution to
806 potential vertical mixing of excess N_2 into the mixed layer may only be prominent in regions

807 where O_2 and nitrate depletion occurs in the upper few hundred of meters of the water column
808 (e.g. Arabian Sea, Eastern Tropical North and South Pacific, suboxic inlets and estuaries; Chang
809 et al., 2010, 2012; DeVries et al., 2012; Tortell, 2005; Wu et al., 2013) or overlying shallow
810 continental shelves where benthic and sedimentary denitrification occur (DeVries et al., 2013).
811 Taking an extreme upper limit of subsurface $\Delta N_2/Ar$ of ~2-2.5 % in these regions (Chang et al.,
812 2010; 2012; Shigemitsu et al., 2016), surface $\Delta N_2/Ar$ anomalies will be less than 2.5 % (Fig. 1).
813 N_2' corrections can minimize this bias, but even without such corrections, the error associated
814 with a 2.5 % underestimation of $\Delta O_2/N_2$ may be smaller than errors associated with vertical O_2
815 mixing fluxes in continental shelf regions (see above).

816 Other processes which we have not evaluated in the present study, such as freshwater
817 input, lateral mixing and ice melt/formation can also cause divergence between ΔAr and ΔN_2
818 (e.g. Beaird et al., 2015; Crabeck et al., 2014; Eveleth et al., 2017; Hamme et al., 2019; Hamme
819 & Emerson, 2013; Loose & Jenkins, 2014; Top et al., 1988), but their contributions to surface
820 $\Delta N_2/Ar$ disequilibria, and the resulting uncertainty in $\Delta O_2/N_2'$-based NCP estimates are likely to
821 be small in most ocean regions. As our model evaluation suggests (section 3.3, above), the
822 framework we presented here captures the main drivers of inert gas and N_2 variability in oceanic
823 waters. Additional fluxes will be larger in coastal, or polar regions, but biases in NCP estimates
824 resulting from vertical O_2 fluxes or diel O_2 variability are likely to be more significant in these
825 regions (see above).

826

827 **4 Conclusions**

828 Global coverage of marine NCP estimates is constrained by the limitation of mass
829 spectrometry to obtain underway $\Delta O_2/Ar$ measurements. Recent advances in Optode and GTD
830 technology have made high-resolution $\Delta O_2/N_2$ sampling feasible, providing potential avenues to
831 expand NCP from low-cost and user-friendly instrument systems (Izett & Tortell, 2020).
832 Differences between Ar and N_2 solubility properties necessitate careful interpretation of in-situ
833 O_2/N_2 measurements in order to accurately isolate biological O_2 signatures. In the present study,
834 we used a model to evaluate the main mechanisms controlling surface water uncoupling between
835 $\Delta O_2/Ar$ and $\Delta O_2/N_2$. Critically, our model, when parameterized with relevant environmental
836 forcing and time-variable mixing terms, accurately captures the main processes driving surface
837 ocean inert gas and N_2 evolution.

838 From our numerical simulations, performed under experimental and realistic conditions,
839 we find that seasonal SST variability exerts long-term control on $\Delta O_2/Ar$ and $\Delta O_2/N_2$
840 decoupling, with transient and baseline modifications resulting from enhanced bubble fluxes
841 during periods of elevated wind-speeds, and variable vertical mixing fluxes. Due to differences
842 in the sensitivity of Ar and N_2 to SST variability and small bubble injection, nominal $\Delta N_2/Ar$
843 anomalies are generally positive over a range of conditions, so that NCP estimates derived from
844 raw $\Delta O_2/N_2$ measurements could be biased low. Fortunately, the predictability of these
845 anomalies to environmental perturbations permits corrections to ΔN_2 measurements, based on a
846 new tracer, $\Delta N_2'$, which we derived from simple MLD budget calculations performed over a
847 relevant NCP time-scale, τ_{O_2}. Applying this $\Delta N_2'$ approach using readily available reanalysis data
848 products allows us to reconcile differences between $\Delta O_2/Ar$ and $\Delta O_2/N_2$, making $\Delta O_2/N_2'$ a
849 robust NCP tracer.

850   The overall uncertainty in $\Delta O_2/N_2'$, resulting from model parameterization errors and
851 necessary simplifying assumptions, is generally smaller than other sources of uncertainty in NCP
852 calculations. Field application of the present approach will depend on the accuracy of
853 environmental data products, and assumptions about the time-variability of mixed layer
854 hydrography. Yet, even when differences between $\Delta O_2/Ar$ and $\Delta O_2/N_2'$ cannot be reduced to
855 zero, N_2' is still a valuable tracer for minimizing NCP errors based on O_2/N_2 measurements. This
856 approach is expected to be most accurate in stratified waters ande during summer conidtions,
857 when surface productivity is elevated, and mixing contributions to $\Delta N_2/Ar$ decoupling may be
858 neglected in N_2' calculations. In most ocean regions, N_2-fixation, denitrification and annamox
859 will have a negligible impact on NCP estimates derived from underway $\Delta O_2/N_2'$.

860   Our work demonstrates the feasibility of deriving $\Delta O_2/N_2'$-based NCP estimates from
861 underway O_2 and N_2 measurements and simple computations. The approach we describe here has
862 the potential to greatly expand NCP coverage from research vessels, volunteer observing
863 platforms and/or automous surface vehicles. This approach, combined with our upcoming field
864 validation (manuscript in preparation) constitutes a significant advance in our ability to
865 accurately quantify NCP and oceanic metabolism across a range of relevant space and time
866 spaces.

867

Acknowledgments

884

References

886 Amundsen Science Data Collection. (2019). CTD data collected by the CCGS Amundsen in the
887 Canadian Arctic. ArcticNet Inc., Québec, Canada. Processed data. Version 1. Archived at
888 www.polardata.ca. Waterloo, Canada: Canadian Cryospheric Information Network (CCIN).
889 https://doi.org/https://doi.org/10.5884/12713. Accessed May 2020.

890 Atlas, R., Hoffman, R. N., Ardizzone, J., Leidner, S. M., Jusem, J. C., Smith, D. K., & Gombos,
891 D. (2011). A cross-calibrated, multiplatform ocean surface wind velocity product for

892   meteorological and oceanographic applications. *Bulletin of the American Meteorological*
893   *Society*, *92*, 157–174. https://doi.org/10.1175/2010BAMS2946.1

894   Beaird, N., Straneo, F., & Jenkins, W. (2015). Spreading of Greenland meltwaters in the ocean
895   revealed by noble gases. *Geophysical Research Letters*, *42*(18), 7705–7713.
896   https://doi.org/10.1002/2015GL065003

897   Bender, M. L., Kinter, S., Cassar, N., & Wanninkhof, R. (2011). Evaluating gas transfer velocity
898   parameterizations using upper ocean radon distributions. *Journal of Geophysical Research:*
899   *Oceans*, *116*(2), 1–11. https://doi.org/10.1029/2009JC005805

900   Blais, M., Tremblay, J. É., Jungblut, A. D., Gagnon, J., Martin, J., Thaler, M., & Lovejoy, C.
901   (2012). Nitrogen fixation and identification of potential diazotrophs in the Canadian Arctic.
902   *Global Biogeochemical Cycles*, *26*(3). https://doi.org/10.1029/2011GB004096

903   Bushinsky, S. M., & Emerson, S. (2015). Marine biological production from in situ oxygen
904   measurements on a profiling float in the subarctic Pacific Ocean. *Global Biogeochemical*
905   *Cycles*, *29*, 2050–2060. https://doi.org/10.1002/2015GB005251

906   Butterworth, B. J., & Miller, S. D. (2016). Air-sea exchange of carbon dioxide in the Southern
907   Ocean and Antarctic marginal ice zone. *Geophysical Research Letters*, *43*, 7223–7230.
908   https://doi.org/10.1002/2016GL069581

909   Castro de la Guardia, L., Garcia-Quintana, Y., Claret, M., Hu, X., Galbraith, E. D., & Myers, P.
910   G. (2019). Assessing the Role of High-Frequency Winds and Sea Ice Loss on Arctic
911   Phytoplankton Blooms in an Ice-Ocean-Biogeochemical Model. *Journal of Geophysical*
912   *Research: Biogeosciences*, *124*(9), 2728–2750. https://doi.org/10.1029/2018JG004869

913   Chang, B. X., Devol, A. H., & Emerson, S. R. (2010). Denitrification and the nitrogen gas excess
914   in the eastern tropical South Pacific oxygen deficient zone. *Deep-Sea Research Part I:*
915   *Oceanographic Research Papers*, *57*(9), 1092–1101.
916   https://doi.org/10.1016/j.dsr.2010.05.009

917   Chang, B. X., Devo, A. H., & Emerson, S. R. (2012). Fixed nitrogen loss from the eastern
918   tropical North Pacific and Arabian Sea oxygen deficient zones determined from
919   measurements of N2:Ar. *Global Biogeochemical Cycles*, *26*(3), 1–8.
920   https://doi.org/10.1029/2011GB004207

921   Chanona, M., Waterman, S., & Gratton, Y. (2018). Variability of Internal Wave-Driven Mixing
922   and Stratification in Canadian Arctic Shelf and Shelf-Slope Waters. *Journal of Geophysical*
923   *Research: Oceans*, *123*(12), 9178–9195. https://doi.org/10.1029/2018JC014342

924   Crabeck, O., Delille, B., Rysgaard, S., Thomas, D. N., Geilfus, N.-X., Else, B., & Tison, J.-L.
925   (2014). First '"in situ"' determination of gas transport coefficients (DO2, DAr, and DN2)
926   from bulk gas concentration measurements (O2, N2, Ar) in natural sea ice. *Journal of*
927   *Geophysical Research: Oceans*, *119*, 6655–6668.
928   https://doi.org/10.1002/2014JC010105.Received

929   Craig, H., & Hayward, T. (1987). Oxygen Supersaturation in the Ocean: Biological Versus
930   Physical Contributions. *Science*, *235*(4785), 199–202.
931   https://doi.org/10.1126/science.235.4785.199

932   Cronin, M. F., Pellan, N. A., Emerson, S. R., & Crawford, W. R. (2015). Estimating diffusivity

from the mixed layer heat and salt balances in the North Pacific. *Journal of Geophysical Research: Oceans*, *120*, 7346–7362. https://doi.org/10.1002/2015JC011010

DeGrandpre, M., Evans, W., Timmermans, M., Krishfield, R., Williams, B., & Steele, M. (2020). Changes in the Arctic Ocean Carbon Cycle With Diminishing Ice Cover. *Geophysical Research Letters*, *47*(12). https://doi.org/10.1029/2020gl088051

Deutsch, C., Sarmiento, J. L., Sigman, D. M., Gruber, N., & Dunne, J. P. (2007). Spatial coupling of nitrogen inputs and losses in the ocean. *Nature*, *445*(7124), 163–167. https://doi.org/10.1038/nature05392

DeVries, T., Deutsch, C., Primeau, F., Chang, B., & Devol, A. (2012). Global rates of water-column denitrification derived from nitrogen gas measurements. *Nature Geoscience*, *5*(8), 547–550. https://doi.org/10.1038/ngeo1515

DeVries, T., Deutsch, C., Rafter, P. A., & Primeau, F. (2013). Marine denitrification rates determined from a global 3-D inverse model. *Biogeosciences*, *10*(4), 2481–2496. https://doi.org/10.5194/bg-10-2481-2013

Emerson, S., & Bushinsky, S. (2016). The role of bubbles during air-sea gas exchange. *Journal of Geophysical Research: Oceans*, *121*(6), 4360–4376. https://doi.org/10.1002/2016JC011744

Emerson, S., & Stump, C. (2010). Net biological oxygen production in the ocean-II: Remote in situ measurements of O2 and N2 in subarctic pacific surface waters. *Deep-Sea Research Part I: Oceanographic Research Papers*, *57*, 1255–1265. https://doi.org/10.1016/j.dsr.2010.06.001

Emerson, S., White, M. R. T., Stump, C., & Bushinsky, S. M. (2017). Salinity and other variables collected from time series observations using Bubble type equilibrator for autonomous carbon dioxide (CO2) measurement, Carbon dioxide (CO2) gas analyzer and other instruments from MOORINGS_PAPA_145W_50N. NOAA National Centers for Environmental Information. Dataset. https://doi.org/https://doi.org/10.3334/cdiac/otg.tsm_papa_145w_50n_o2_n2.

Emerson, S., Yang, B., White, M., & Cronin, M. (2019). Air-Sea Gas Transfer: Determining Bubble Fluxes With In Situ N2 Observations. *Journal of Geophysical Research: Oceans*, *124*(4), 2716–2727. https://doi.org/10.1029/2018JC014786

Eveleth, R., Timmermans, M.-L., & Cassar, N. (2014). Physical and biological controls on oxygen saturation variability in the upper Arctic Ocean. *Journal of Geophysical Research: Oceans*, *119*(11), 7420–7432. https://doi.org/https://doi.org/10.1002/2014JC009816

Eveleth, R., Cassar, N., Doney, S. C., Munro, D. R., & Sweeney, C. (2017). Biological and physical controls on O2/Ar, Ar and pCO2 variability at the Western Antarctic Peninsula and in the Drake Passage. *Deep-Sea Research Part II*, *139*, 77–88. https://doi.org/10.1016/j.dsr2.2016.05.002

Fassbender, A. J., Sabine, C. L., & Cronin, M. F. (2016). Net community production and calcification from 7 years of NOAA Station Papa Morring measurements. *Global Biogeochemical Cycles*, *30*, 250–267. https://doi.org/10.1002/2015GB005205

Garcia, H. E., & Gordon, L. I. (1993). Erratum: Oxygen solubility in seawater: better fitting

974   equations. *Limnology and Oceanography*, *38*, 656.

975   Giesbrecht, K. E., Hamme, R. C., & Emerson, S. R. (2012). Biological productivity along Line P
976   in the subarctic northeast Pacific: In situ versus incubation-based methods. *Global
977   Biogeochemical Cycles*, *26*(GB3028). https://doi.org/10.1029/2012GB004349

978   Gordon, C., Fennel, K., Richards, C., Shay, L. K., & Brewster, J. K. (2020). Can ocean
979   community production and respiration be determined by measuring high-frequency oxygen
980   profiles from autonomous floats? *Biogeosciences Discuss*, (Preprint).
981   https://doi.org/10.5194/bg-2020-119

982   Gruber, N., & Sarmiento, J. L. (1997). Global paterns of marine nitrogen fixation and
983   denitrification. *Global Biogeochemical Cycles*, *11*(2), 235–266.

984   Hamme, R. C., & Emerson, S. R. (2002). Mechanisms controlling the global oceanic distribution
985   of the inert gases argon, nitrogen and neon. *Geophysical Research Letters*, *29*(23), 1–4.
986   https://doi.org/10.1029/2002GL015273

987   Hamme, R. C., & Emerson, S. R. (2004). The solubility of neon , nitrogen and argon in distilled
988   water and seawater. *Deep-Sea Research Part I*, *51*, 1517–1528.
989   https://doi.org/10.1016/j.dsr.2004.06.009

990   Hamme, R. C., & Emerson, S. R. (2006). Constraining bubble dynamics and mixing with
991   dissolved gases: Implications for productivity measurements by oxygen mass balance.
992   *Journal of Marine Research*, *64*, 73–95. https://doi.org/10.1357/002224006776412322

993   Hamme, R. C., & Emerson, S. R. (2013). Deep-sea nutrient loss inferred from the marine
994   dissolved N2/Ar ratio. *Geophysical Research Letters*, *40*(6), 1149–1153.
995   https://doi.org/10.1002/grl.50275

996   Hamme, R. C., & Severinghaus, J. P. (2007). Trace gas disequilibria during deep-water
997   formation. *Deep-Sea Research Part I: Oceanographic Research Papers*, *54*(6), 939–950.
998   https://doi.org/10.1016/j.dsr.2007.03.008

999   Hamme, R. C., Cassar, N., Lance, V. P., Vaillancourt, R. D., Bender, M. L., Strutton, P. G., et al.
1000   (2012). Dissolved O_2/Ar and other methods reveal rapid changes in productivity during a
1001   Lagrangian experiment in the Southern Ocean. *Journal of Geophysical Research*,
1002   *117*(C00F12). https://doi.org/10.1029/2011JC007046

1003   Hamme, R. C., Emerson, S. R., Severinghaus, J. P., Long, M. C., & Yashayaev, I. (2017). Using
1004   Noble Gas Measurements to Derive Air-Sea Process Information and Predict Physical Gas
1005   Saturations. *Geophysical Research Letters*, *44*(19), 9901–9909.
1006   https://doi.org/10.1002/2017GL075123

1007   Hamme, R. C., Nicholson, D. P., Jenkins, W. J., & Emerson, S. R. (2019). Using Noble Gases to
1008   Assess the Ocean's Carbon Pumps. *Annual Review of Marine Science*, *11*(18), 1–29.
1009   https://doi.org/10.1146/annurev-marine-121916-063604

1010   Hartmann, D. L. (1994). The ocean general circulation and climate. In *Global Physical
1011   Climatology* (pp. 171–203). San Diego, CA: Academic Press.

1012   Howard, E., Emerson, S., Bushinsky, S., & Stump, C. (2010). The role of net community
1013   production in air-sea carbon fluxes at the North Pacific subarctic-subtropical boundary
1014   region. *Limnology and Oceanography*, *55*(6), 2585–2596.

1015   https://doi.org/10.4319/lo.2010.55.6.2585

1016 Islam, F., DeGrandpre, M., Beatty, C., Krishfield, R., & Toole, J. (2016). Gas exchange of CO2
1017   and O2 in partially ice-covered regions of the Arctic Ocean investigated using in situ
1018   sensors. *IOP Conference Series: Earth and Environmental Science*, *35*(012018).
1019   https://doi.org/10.1088/1755-1315/35/1/012018

1020 Ito, T., & Deutsch, C. (2006). Understanding the saturation state of argon in the thermocline: The
1021   role of air-sea gas exchange and diapycnal mixing. *Global Biogeochemical Cycles*, *20*(3),
1022   1–15. https://doi.org/10.1029/2005GB002655

1023 Izett, R., & Tortell, P. (2020). The Pressure of In Situ Gases Instrument (PIGI) for Autonomous
1024   Shipboard Measurement of Dissolved O2 and N2 in Surface Ocean Waters. *Oceanography*,
1025   *33*(2). https://doi.org/10.5670/oceanog.2020.214

1026 Izett, R., Manning, C. C., Hamme, R. C., & Tortell, P. D. (2018). Refined estimates of net
1027   community production in the Subarctic Northeast Pacific derived from ΔO2/Ar
1028   measurements with N2O-based corrections for vertical mixing. *Global Biogeochemical*
1029   *Cycles*, *32*, 326–350. https://doi.org/https://doi.org/10.1002/2017GB005792

1030 Johnson, K. S., Plant, J. N., Dunne, J. P., Talley, L. D., & Sarmiento, J. L. (2017). Annual nitrate
1031   drawdown observed by SOCCOM profiling floats and the relationship to annual net
1032   community production. *Journal of Geophysical Research: Oceans*, *122*(8), 6668–6683.
1033   https://doi.org/10.1002/2017JC012839

1034 Jonsson, B. F., Doney, S. C., Dunne, J., & Bender, M. (2013). Evaluation of the Southern Ocean
1035   O$_2$/Ar-based NCP estimates in a model framework. *Journal of Geophysical Research:*
1036   *Biogeosciences*, *118*, 385–399. https://doi.org/10.1002/jgrg.20032

1037 Juranek, L., Takahashi, T., Mathis, J., & Pickart, R. (2019). Significant Biologically Mediated
1038   CO2 Uptake in the Pacific Arctic During the Late Open Water Season. *Journal of*
1039   *Geophysical Research: Oceans*, *124*(2), 1–23. https://doi.org/10.1029/2018JC014568

1040 Kaiser, J., Reuer, M. K., Barnett, B., & Bender, M. L. (2005). Marine productivity estimates
1041   from continuous O$_2$/Ar ratio measurements by membrane inlet mass spectrometry.
1042   *Geophysical Research Letters*, *32*(L19605). https://doi.org/10.1029/2005GL023459

1043 Kalnay, E., Kanamitsu, M., Kistler, R., Collins, W., Deaven, D., Gandin, L., et al. (1996). The
1044   NCEP/NCAR 40-year reanalysis project. *Bulletin of the American Meteorological Society*,
1045   *77*, 437–471. https://doi.org/10.1175/1520-0477(1996)077<0437:TNYRP>2.0.CO;2

1046 Kana, T. M., Sullivan, M. B., Cornwell, J. C., & Groszkowski, K. M. (1998). Denitrification in
1047   estuarine sediments determined by membrane inlet mass spectrometry. *Limnology and*
1048   *Oceanography*, *43*(2), 334–339. https://doi.org/10.4319/lo.1998.43.2.0334

1049 Liang, J.-H. H., Deutsch, C., McWilliams, J. C., Baschek, B., Sullivan, P. P., & Chiba, D.
1050   (2013). Parameterizing bubble-mediated air-sea gas exchange and its effect on ocean
1051   ventilation. *Global Biogeochemical Cycles*, *27*(3), 894–905.
1052   https://doi.org/10.1002/gbc.20080

1053 Liang, J. H., Emerson, S. R., D'Asaro, E. A., McNeil, C. L., Harcourt, R. R., Sullivan, P. P., et
1054   al. (2017). On the role of sea-state in bubble-mediated air-sea gas flux during a winter
1055   storm. *Journal of Geophysical Research: Oceans*, *122*(4), 2671–2685.

1056   https://doi.org/10.1002/2016JC012408

1057   Lockwood, D., Quay, P. D., Kavanaugh, M. T., Juranek, L. W., & Feely, R. A. (2012). High-
1058   resolution estimates of net community production and air-sea CO_2 flux in the northeast
1059   Pacific. *Global Biogeochemical Cycles*, *26*(GB4010).
1060   https://doi.org/10.1029/2012GB004380

1061   Loose, B., & Jenkins, W. J. (2014). The five stable noble gases are sensitive unambiguous tracers
1062   of glacial meltwater. *Geophysical Research Letters*, *41*, 2835–2841.
1063   https://doi.org/doi:10.1002/2013GL058804

1064   Loose, B., McGillis, W. R., Perovich, D., Zappa, C. J., & Schlosser, P. (2014). A parameter
1065   model of gas exchange for the seasonal sea ice zone. *Ocean Science*, *10*(1), 17–28.
1066   https://doi.org/10.5194/os-10-17-2014

1067   Manning, C. C., Stanley, R. H. R., Nicholson, D. P., Loose, B., Lovely, A., Schlosser, P., &
1068   Hatcher, B. G. (2017). Changes in gross oxygen production, net oxygen production, and air-
1069   water gas exchange during seasonal ice melt in the Bras d'Or Lake, a Canadian estuary.
1070   *Biogeosciences Discussions*. https://doi.org/10.5194/bg-2017-428

1071   McNeil, C., D'Asaro, E., Johnson, B., & Horn, M. (2006a). A gas tension device with response
1072   times of minutes. *Journal of Atmospheric and Oceanic Technology*, *23*(11), 1539–1558.
1073   https://doi.org/10.1175/JTECH1974.1

1074   McNeil, C., Katz, D. R., Ward, B., McGillis, W. R., & Johnson, B. D. (2006b). A method to
1075   estimate net community metabolism from profiles of dissolved O2 and N2. *Hydrobiologia*,
1076   *571*(1), 181–190. https://doi.org/10.1007/s10750-006-0236-7

1077   McNeil, C. L., Johnson, B. D., & Farmer, D. M. (1995). In situ measurement of dissolved
1078   nitrogen and oxygen in the ocean. *Deep-Sea Research Part I*, *42*(5), 819–826.
1079   https://doi.org/10.1016/0967-0637(95)97829-W

1080   Mordy, C. W., Cokelet, E. D., Robertis, A. De, Jenkins, R., Kuhn, C. E., Lawrence-Salvas, N., et
1081   al. (2017). Advances in Ecosystem Research: Saildrone Surveys of Oceanography, Fish,
1082   and Marine Mammals in the Bering Sea. *Oceanography*, *30*(2), 113–115.

1083   Munro, D. R., Quay, P. D., Juranek, L. W., & Goericke, R. (2013). Biological production rates
1084   off the Southern California coast estimated from triple O_2 isotopes and O_2 : Ar gas ratios.
1085   *Limnology and Oceanography*, *58*(4), 1312–1328.
1086   https://doi.org/10.4319/lo.2013.58.4.1312

1087   Nicholson, D., Emerson, S., Caillon, N., Jouzel, J., & Hamme, R. C. (2010). Constraining
1088   ventilation during deepwater formation using deep ocean measurements of the dissolved gas
1089   ratios 40 Ar/ 36 Ar, N 2 /Ar, and Kr/Ar. *Journal of Geophysical Research*, *115*(C11015), 1–
1090   15. https://doi.org/10.1029/2010jc006152

1091   Nilsson, E. D., Rannik, Ü., Swietlicki, E., Leck, C., Aalto, P. P., Zhou, J., & Norman, M. (2001).
1092   Turbulent aerosol fluxes over the Arctic Ocean 2. Wind-driven sources from the sea.
1093   *Journal of Geophysical Research*, *106*(D23), 32139–32154.

1094   Palevsky, H. I., Quay, P. D., Lockwood, D. E., & Nicholson, D. P. (2016). The annual cycle of
1095   gross primary production, net community production, and export efficiency across the
1096   North Pacific Ocean. *Global Biogeochemical Cycles*, *30*(2), 361–380.

1097   https://doi.org/10.1002/2015GB005318

1098 Pelland, N. A., Eriksen, C. C., Emerson, S. R., & Cronin, M. F. (2018). Seaglider surveys at
1099   Ocean Station Papa: Oxygen kinematics and upper-ocean metabolism. *Journal of*
1100   *Geophysical Research: Oceans*, 1–20. https://doi.org/10.1029/2018JC014091

1101 Plant, J. N., Johnson, K. S., Sakamoto, C. M., Jannasch, H. W., Coletti, L. J., Riser, S. C., &
1102   Swift, D. D. (2016). Net community production at Ocean Station Papa observed with nitrate
1103   and oxygen sensors on profiling floats. *Global Biogeochemical Cycles*, *30*, 859–879.
1104   https://doi.org/10.1002/2015GB005349.Received

1105 Reed, A., McNeil, C., D'Asaro, E., Altabet, M., Bourbonnais, A., & Johnson, B. (2018). A gas
1106   tension device for the mesopelagic zone. *Deep-Sea Research Part I*, *139*(2018), 68–78.
1107   https://doi.org/10.1016/j.dsr.2018.07.007

1108 Reynolds, R. W., Smith, T. M., Liu, C., Chelton, D. B., Casey, K. S., & Schlax, M. G. (2007).
1109   Daily High-Resolution-Blended Analyses for Sea Surface Temperature. *Journal of Climate*,
1110   *20*, 5473-5496.

1111 Rosengard, S. Z., Izett, R. W., Burt, W. J., Schuback, N., & Tortell, P. D. (2020). Decoupling of
1112 O_2 / Ar and particulate organic carbon dynamics in nearshore surface ocean waters.
1113   *Biogeosciences*, *17*, 3277–3298. Retrieved from https://doi.org/10.5194/bg-17-3277-2020

1114 Scheifele, B., Waterman, S., Merckelbach, L., & Carpenter, J. R. (2018). Measuring the
1115   Dissipation Rate of Turbulent Kinetic Energy in Strongly Stratified, Low-Energy
1116   Environments: A Case Study From the Arctic Ocean. *Journal of Geophysical Research:*
1117   *Oceans*, *123*, 5459–5480. https://doi.org/10.1029/2017JC013731

1118 Schmidtko, S., Johnson, G. C., & Lyman, J. M. (2013). MIMOC: A global monthly isopycnal
1119   upper-ocean climatology with mixed layers. *Journal of Geophysical Research: Oceans*,
1120   *118*, 1658–1672.

1121 Shigemitsu, M., Gruber, N., Oka, A., & Yamanaka, Y. (2016). Potential use of the N2/Ar ratio as
1122   a constraint on the oceanic fixed nitrogen loss. *Global Biogeochemical Cycles*, *30*, 576–594.
1123   https://doi.org/10.1111/1462-2920.13280

1124 Sipler, R. E., Gong, D., Baer, S. E., Sanderson, M. P., Roberts, Q. N., Mulholland, M. R., &
1125   Bronk, D. A. (2017). Preliminary estimates of the contribution of Arctic nitrogen fixation to
1126   the global nitrogen budget. *Limnology and Oceanography Letters*, *2*(5), 159–166.
1127   https://doi.org/10.1002/lol2.10046

1128 Steiner, N., Vagle, S., Denman, K. L., & McNeil, C. (2007). Oxygen and nitrogen cycling in the
1129   northeast Pacific - Simulations and observations at Station Papa in 2003/2004. *Journal of*
1130   *Marine Research*, *65*(3), 441–469. https://doi.org/10.1357/002224007781567658

1131 Tang, W., Wang, S., Fonseca-Batista, D., Dehairs, F., Gifford, S., Gonzalez, A. G., et al. (2019).
1132   Revisiting the distribution of oceanic N2 fixation and estimating diazotrophic contribution
1133   to marine production. *Nature Communications*, *10*(1), 1–10.
1134   https://doi.org/10.1038/s41467-019-08640-0

1135 Tang, W., Cerdán-García, E., Berthelot, H., Polyviou, D., Wang, S., Baylay, A., et al. (2020).
1136   New insights into the distributions of nitrogen fixation and diazotrophs revealed by high-
1137   resolution sensing and sampling methods. *ISME Journal*. https://doi.org/10.1038/s41396-

1138   020-0703-6

1139 Teeter, L., Hamme, R. C., Ianson, D., & Bianucci, L. (2018). Accurate Estimation of Net
1140   Community Production From O2/Ar Measurements. *Global Biogeochemical Cycles*, 1–19.
1141   https://doi.org/10.1029/2017GB005874

1142 Tengberg, A., Hovdenes, J., Andersson, H. J., Brocandel, O., Diaz, R., Hebert, D., et al. (2006).
1143   Evaluation of a lifetime-based optode to measure oxygen in aquatic systems. *Limnology and*
1144   *Oceanography: Methods*, *4*(2), 7–17. https://doi.org/10.4319/lom.2006.4.7

1145 Top, Z., Martin, S., & Becker, P. (1988). A labratory study of dissolved noble gas anomaly due
1146   to ice formation. *Geophysical Research Letters*, *15*(8), 796–799.

1147 Tortell, P. D. (2005). Dissolved gas measurements in oceanic waters made by membrane inlet
1148   mass spectrometry. *Limnology and Oceanography: Methods*, *3*, 24–37.
1149   https://doi.org/10.4319/lom.2005.3.24

1150 Tortell, P. D., Bittig, H. C., Körtzinger, A., Jones, E. M., & Hoppema, M. (2015). Biological and
1151   physical controls on N2, O2, and CO2 distributions in contrasting Southern Ocean surface
1152   waters. *Global Biogeochemical Cycles*, *29*, 994–1013.
1153   https://doi.org/10.1002/2014GB004975

1154 Ulfsbo, A., Cassar, N., Korhonen, M., van Heuven, S., Hoppema, M., Kattner, G., & Anderson,
1155   L. G. (2014). Late summer net community production in the central Arctic Ocean using
1156   multiple approaches. *Global Biogeochemical Cycles*, *28*, 1129–1148.
1157   https://doi.org/10.1002/2014GB004833

1158 Voermans, J. J., Babanin, A. V., Thomson, J., Smith, M. M., & Shen, H. H. (2019). Wave
1159   Attenuation by Sea Ice Turbulence. *Geophysical Research Letters*, *46*(12), 6796–6803.
1160   https://doi.org/10.1029/2019GL082945

1161 Wang, S., Kranz, S. A., Kelly, T. B., Song, H., Stukel, M. R., & Cassar, N. (2020). Lagrangian
1162   Studies of Net Community Production: The Effect of Diel and Multiday Nonsteady State
1163   Factors and Vertical Fluxes on O 2 /Ar in a Dynamic Upwelling Region. *Journal of*
1164   *Geophysical Research: Biogeosciences*, *125*(6), 1–19.
1165   https://doi.org/10.1029/2019jg005569

1166 Wanninkhof, R. (2014). Relationship between wind speed and gas exchange over the ocean
1167   revisited. *Limnology and Oceanography: Methods*, *12*(6), 351–362.
1168   https://doi.org/10.1029/92JC00188

1169 Weeding, B., & Trull, T. W. (2014). Hourly oxygen and total gas tension measurements at the
1170   Southern Ocean Time Series site reveal winter ventilation and spring net community
1171   production. *Journal of Geophysical Research: Oceans*, *119*, 348–358.
1172   https://doi.org/10.1002/2013JC009302

1173 Weiss, R. F. (1970). The solubility of nitrogen, oxygen and argoninwater and seawater. *Deep Sea*
1174   *Research*, *17*(4), 721–735.

1175 Whalen, C. B., Talley, L. D., & MacKinnon, J. A. (2012). Spatial and temporal variability of
1176   global ocean mixing inferred from Argo profiles. *Geophysical Research Letters*, *39*(17).
1177   https://doi.org/10.1029/2012GL053196

1178 Wise, D. L., & Houghton, G. (1966). The diffusion coefficients of ten slightly soluble gases in

1179   water at 10-60°C. *Chemical Engineering Science*, *21*(11), 999–1010.
1180   https://doi.org/10.1016/0009-2509(66)85096-0

1181 Woolf, D. K., & Thorpe, S. A. (1991). Bubbles and the air-sea exchange of gases in near-
1182   saturation conditions. *Journal of Marine Research*, *49*, 435–466.
1183   https://doi.org/10.1357/002224091784995765

1184 Wu, J., Chen, N., Hong, H., Lu, T., Wang, L., & Chen, Z. (2013). Direct measurement of
1185   dissolved N2 and denitrification along a subtropical river-estuary gradient, China. *Marine*
1186   *Pollution Bulletin*, *66*(2013), 125–134. https://doi.org/10.1016/j.marpolbul.2012.10.020

1187 Yang, B., Emerson, S. R., & Bushinsky, S. M. (2017). Annual net community production in the
1188   subtropical Pacific Ocean from in-situ oxygen measurements on profiling floats. *Global*
1189   *Biogeochemical Cycles*, *31*, 728–744. https://doi.org/10.1002/2016GB005545

1190 Zhou, J., Delille, B., Brabant, F., & Tison, J. L. (2014). Insights into oxygen transport and net
1191   community production in sea ice from oxygen, nitrogen and argon concentrations.
1192   *Biogeosciences*, *11*, 5007–5020. https://doi.org/10.5194/bg-11-5007-2014

1193

1194

Supporting Information References

1196 Amundsen Science Data Collection. (2019). CTD data collected by the CCGS Amundsen in the
1197   Canadian Arctic. ArcticNet Inc., Québec, Canada. Processed data. Version 1. Archived at
1198   www.polardata.ca. Waterloo, Canada: Canadian Cryospheric Information Network (CCIN).
1199   https://doi.org/https://doi.org/10.5884/12713. Accessed May 2020.

1200 Atlas, R., Hoffman, R. N., Ardizzone, J., Leidner, S. M., Jusem, J. C., Smith, D. K., & Gombos,
1201   D. (2011). A cross-calibrated, multiplatform ocean surface wind velocity product for
1202   meteorological and oceanographic applications. *Bulletin of the American Meteorological*
1203   *Society*, *92*, 157–174. https://doi.org/10.1175/2010BAMS2946.1

1204 Beaird, N., Straneo, F., & Jenkins, W. (2015). Spreading of Greenland meltwaters in the ocean
1205   revealed by noble gases. *Geophysical Research Letters*, *42*(18), 7705–7713.
1206   https://doi.org/10.1002/2015GL065003

1207 Bender, M. L., Kinter, S., Cassar, N., & Wanninkhof, R. (2011). Evaluating gas transfer velocity
1208   parameterizations using upper ocean radon distributions. *Journal of Geophysical Research:*
1209   *Oceans*, *116*(2), 1–11. https://doi.org/10.1029/2009JC005805

1210 Blais, M., Tremblay, J. É., Jungblut, A. D., Gagnon, J., Martin, J., Thaler, M., & Lovejoy, C.
1211   (2012). Nitrogen fixation and identification of potential diazotrophs in the Canadian Arctic.
1212   *Global Biogeochemical Cycles*, *26*(3). https://doi.org/10.1029/2011GB004096

1213 Bushinsky, S. M., & Emerson, S. (2015). Marine biological production from in situ oxygen
1214   measurements on a profiling float in the subarctic Pacific Ocean. *Global Biogeochemical*
1215   *Cycles*, *29*, 2050–2060. https://doi.org/10.1002/2015GB005251

1216 Butterworth, B. J., & Miller, S. D. (2016). Air-sea exchange of carbon dioxide in the Southern
1217   Ocean and Antarctic marginal ice zone. *Geophysical Research Letters*, *43*, 7223–7230.
1218   https://doi.org/10.1002/2016GL069581

Castro de la Guardia, L., Garcia-Quintana, Y., Claret, M., Hu, X., Galbraith, E. D., & Myers, P. G. (2019). Assessing the Role of High-Frequency Winds and Sea Ice Loss on Arctic Phytoplankton Blooms in an Ice-Ocean-Biogeochemical Model. *Journal of Geophysical Research: Biogeosciences*, *124*(9), 2728–2750. https://doi.org/10.1029/2018JG004869

Chang, B. X., Devol, A. H., & Emerson, S. R. (2010). Denitrification and the nitrogen gas excess in the eastern tropical South Pacific oxygen deficient zone. *Deep-Sea Research Part I: Oceanographic Research Papers*, *57*(9), 1092–1101. https://doi.org/10.1016/j.dsr.2010.05.009

Chang, B. X., Devo, A. H., & Emerson, S. R. (2012). Fixed nitrogen loss from the eastern tropical North Pacific and Arabian Sea oxygen deficient zones determined from measurements of N2:Ar. *Global Biogeochemical Cycles*, *26*(3), 1–8. https://doi.org/10.1029/2011GB004207

Chanona, M., Waterman, S., & Gratton, Y. (2018). Variability of Internal Wave-Driven Mixing and Stratification in Canadian Arctic Shelf and Shelf-Slope Waters. *Journal of Geophysical Research: Oceans*, *123*(12), 9178–9195. https://doi.org/10.1029/2018JC014342

Crabeck, O., Delille, B., Rysgaard, S., Thomas, D. N., Geilfus, N.-X., Else, B., & Tison, J.-L. (2014). First '"in situ"' determination of gas transport coefficients (DO2, DAr, and DN2) from bulk gas concentration measurements (O2, N2, Ar) in natural sea ice. *Journal of Geophysical Research: Oceans*, *119*, 6655–6668. https://doi.org/10.1002/2014JC010105.Received

Craig, H., & Hayward, T. (1987). Oxygen Supersaturation in the Ocean: Biological Versus Physical Contributions. *Science*, *235*(4785), 199–202. https://doi.org/10.1126/science.235.4785.199

Cronin, M. F., Pellan, N. A., Emerson, S. R., & Crawford, W. R. (2015). Estimating diffusivity from the mixed layer heat and salt balances in the North Pacific. *Journal of Geophysical Research: Oceans*, *120*, 7346–7362. https://doi.org/10.1002/2015JC011010

DeGrandpre, M., Evans, W., Timmermans, M., Krishfield, R., Williams, B., & Steele, M. (2020). Changes in the Arctic Ocean Carbon Cycle With Diminishing Ice Cover. *Geophysical Research Letters*, *47*(12). https://doi.org/10.1029/2020gl088051

Deutsch, C., Sarmiento, J. L., Sigman, D. M., Gruber, N., & Dunne, J. P. (2007). Spatial coupling of nitrogen inputs and losses in the ocean. *Nature*, *445*(7124), 163–167. https://doi.org/10.1038/nature05392

DeVries, T., Deutsch, C., Primeau, F., Chang, B., & Devol, A. (2012). Global rates of water-column denitrification derived from nitrogen gas measurements. *Nature Geoscience*, *5*(8), 547–550. https://doi.org/10.1038/ngeo1515

DeVries, T., Deutsch, C., Rafter, P. A., & Primeau, F. (2013). Marine denitrification rates determined from a global 3-D inverse model. *Biogeosciences*, *10*(4), 2481–2496. https://doi.org/10.5194/bg-10-2481-2013

Emerson, S., & Bushinsky, S. (2016). The role of bubbles during air-sea gas exchange. *Journal of Geophysical Research: Oceans*, *121*(6), 4360–4376. https://doi.org/10.1002/2016JC011744

1260   Emerson, S., & Stump, C. (2010). Net biological oxygen production in the ocean-II: Remote in
1261   situ measurements of O2 and N2 in subarctic pacific surface waters. *Deep-Sea Research*
1262   *Part I: Oceanographic Research Papers*, *57*, 1255–1265.
1263   https://doi.org/10.1016/j.dsr.2010.06.001

1264   Emerson, S., White, M. R. T., Stump, C., & Bushinsky, S. M. (2017). Salinity and other
1265   variables collected from time series observations using Bubble type equilibrator for
1266   autonomous carbon dioxide (CO2) measurement, Carbon dioxide (CO2) gas analyzer and
1267   other instruments from MOORINGS_PAPA_145W_50N. NOAA National Centers for
1268   Environmental Information. Dataset.
1269   https://doi.org/https://doi.org/10.3334/cdiac/otg.tsm_papa_145w_50n_o2_n2.

1270   Emerson, S., Yang, B., White, M., & Cronin, M. (2019). Air-Sea Gas Transfer: Determining
1271   Bubble Fluxes With In Situ N2 Observations. *Journal of Geophysical Research: Oceans*,
1272   *124*(4), 2716–2727. https://doi.org/10.1029/2018JC014786

1273   Eveleth, R., Timmermans, M.-L., & Cassar, N. (2014). Physical and biological controls on
1274   oxygen saturation variability in the upper Arctic Ocean. *Journal of Geophysical Research:*
1275   *Oceans*, *119*(11), 7420–7432. https://doi.org/https://doi.org/10.1002/2014JC009816

1276   Eveleth, R., Cassar, N., Doney, S. C., Munro, D. R., & Sweeney, C. (2017). Biological and
1277   physical controls on O2/Ar, Ar and pCO2 variability at the Western Antarctic Peninsula and
1278   in the Drake Passage. *Deep-Sea Research Part II*, *139*, 77–88.
1279   https://doi.org/10.1016/j.dsr2.2016.05.002

1280   Fassbender, A. J., Sabine, C. L., & Cronin, M. F. (2016). Net community production and
1281   calcification from 7 years of NOAA Station Papa Morring measurements. *Global*
1282   *Biogeochemical Cycles*, *30*, 250–267. https://doi.org/10.1002/2015GB005205

1283   Garcia, H. E., & Gordon, L. I. (1993). Erratum: Oxygen solubility in seawater: better fitting
1284   equations. *Limnology and Oceanography*, *38*, 656.

1285   Giesbrecht, K. E., Hamme, R. C., & Emerson, S. R. (2012). Biological productivity along Line P
1286   in the subarctic northeast Pacific: In situ versus incubation-based methods. *Global*
1287   *Biogeochemical Cycles*, *26*(GB3028). https://doi.org/10.1029/2012GB004349

1288   Gordon, C., Fennel, K., Richards, C., Shay, L. K., & Brewster, J. K. (2020). Can ocean
1289   community production and respiration be determined by measuring high-frequency oxygen
1290   profiles from autonomous floats? *Biogeosciences Discuss*, (Preprint).
1291   https://doi.org/10.5194/bg-2020-119

1292   Gruber, N., & Sarmiento, J. L. (1997). Global paterns of marine nitrogen fixation and
1293   denitrification. *Global Biogeochemical Cycles*, *11*(2), 235–266.

1294   Hamme, R. C., & Emerson, S. R. (2002). Mechanisms controlling the global oceanic distribution
1295   of the inert gases argon, nitrogen and neon. *Geophysical Research Letters*, *29*(23), 1–4.
1296   https://doi.org/10.1029/2002GL015273

1297   Hamme, R. C., & Emerson, S. R. (2004). The solubility of neon , nitrogen and argon in distilled
1298   water and seawater. *Deep-Sea Research Part I*, *51*, 1517–1528.
1299   https://doi.org/10.1016/j.dsr.2004.06.009

1300   Hamme, R. C., & Emerson, S. R. (2006). Constraining bubble dynamics and mixing with

1301   dissolved gases: Implications for productivity measurements by oxygen mass balance.
1302   *Journal of Marine Research*, *64*, 73–95. https://doi.org/10.1357/002224006776412322

1303 Hamme, R. C., & Emerson, S. R. (2013). Deep-sea nutrient loss inferred from the marine
1304   dissolved N2/Ar ratio. *Geophysical Research Letters*, *40*(6), 1149–1153.
1305   https://doi.org/10.1002/grl.50275

1306 Hamme, R. C., & Severinghaus, J. P. (2007). Trace gas disequilibria during deep-water
1307   formation. *Deep-Sea Research Part I: Oceanographic Research Papers*, *54*(6), 939–950.
1308   https://doi.org/10.1016/j.dsr.2007.03.008

1309 Hamme, R. C., Cassar, N., Lance, V. P., Vaillancourt, R. D., Bender, M. L., Strutton, P. G., et al.
1310   (2012). Dissolved O2/Ar and other methods reveal rapid changes in productivity during a
1311   Lagrangian experiment in the Southern Ocean. *Journal of Geophysical Research*,
1312   *117*(C00F12). https://doi.org/10.1029/2011JC007046

1313 Hamme, R. C., Emerson, S. R., Severinghaus, J. P., Long, M. C., & Yashayaev, I. (2017). Using
1314   Noble Gas Measurements to Derive Air-Sea Process Information and Predict Physical Gas
1315   Saturations. *Geophysical Research Letters*, *44*(19), 9901–9909.
1316   https://doi.org/10.1002/2017GL075123

1317 Hamme, R. C., Nicholson, D. P., Jenkins, W. J., & Emerson, S. R. (2019). Using Noble Gases to
1318   Assess the Ocean's Carbon Pumps. *Annual Review of Marine Science*, *11*(18), 1–29.
1319   https://doi.org/10.1146/annurev-marine-121916-063604

1320 Hartmann, D. L. (1994). The ocean general circulation and climate. In *Global Physical
1321   Climatology* (pp. 171–203). San Diego, CA: Academic Press.

1322 Howard, E., Emerson, S., Bushinsky, S., & Stump, C. (2010). The role of net community
1323   production in air-sea carbon fluxes at the North Pacific subarctic-subtropical boundary
1324   region. *Limnology and Oceanography*, *55*(6), 2585–2596.
1325   https://doi.org/10.4319/lo.2010.55.6.2585

1326 Islam, F., DeGrandpre, M., Beatty, C., Krishfield, R., & Toole, J. (2016). Gas exchange of CO2
1327   and O2 in partially ice-covered regions of the Arctic Ocean investigated using in situ
1328   sensors. *IOP Conference Series: Earth and Environmental Science*, *35*(012018).
1329   https://doi.org/10.1088/1755-1315/35/1/012018

1330 Ito, T., & Deutsch, C. (2006). Understanding the saturation state of argon in the thermocline: The
1331   role of air-sea gas exchange and diapycnal mixing. *Global Biogeochemical Cycles*, *20*(3),
1332   1–15. https://doi.org/10.1029/2005GB002655

1333 Izett, R., & Tortell, P. (2020). The Pressure of In Situ Gases Instrument (PIGI) for Autonomous
1334   Shipboard Measurement of Dissolved O2 and N2 in Surface Ocean Waters. *Oceanography*,
1335   *33*(2). https://doi.org/10.5670/oceanog.2020.214

1336 Izett, R., Manning, C. C., Hamme, R. C., & Tortell, P. D. (2018). Refined estimates of net
1337   community production in the Subarctic Northeast Pacific derived from ΔO2/Ar
1338   measurements with N2O-based corrections for vertical mixing. *Global Biogeochemical
1339   Cycles*, *32*, 326–350. https://doi.org/https://doi.org/10.1002/2017GB005792

1340 Johnson, K. S., Plant, J. N., Dunne, J. P., Talley, L. D., & Sarmiento, J. L. (2017). Annual nitrate
1341   drawdown observed by SOCCOM profiling floats and the relationship to annual net

community production. *Journal of Geophysical Research: Oceans*, *122*(8), 6668–6683. https://doi.org/10.1002/2017JC012839

Jonsson, B. F., Doney, S. C., Dunne, J., & Bender, M. (2013). Evaluation of the Southern Ocean O_2/Ar-based NCP estimates in a model framework. *Journal of Geophysical Research: Biogeosciences*, *118*, 385–399. https://doi.org/10.1002/jgrg.20032

Juranek, L., Takahashi, T., Mathis, J., & Pickart, R. (2019). Significant Biologically Mediated CO2 Uptake in the Pacific Arctic During the Late Open Water Season. *Journal of Geophysical Research: Oceans*, *124*(2), 1–23. https://doi.org/10.1029/2018JC014568

Kaiser, J., Reuer, M. K., Barnett, B., & Bender, M. L. (2005). Marine productivity estimates from continuous O_2/Ar ratio measurements by membrane inlet mass spectrometry. *Geophysical Research Letters*, *32*(L19605). https://doi.org/10.1029/2005GL023459

Kalnay, E., Kanamitsu, M., Kistler, R., Collins, W., Deaven, D., Gandin, L., et al. (1996). The NCEP/NCAR 40-year reanalysis project. *Bulletin of the American Meteorological Society*, *77*, 437–471. https://doi.org/10.1175/1520-0477(1996)077<0437:TNYRP>2.0.CO;2

Kana, T. M., Sullivan, M. B., Cornwell, J. C., & Groszkowski, K. M. (1998). Denitrification in estuarine sediments determined by membrane inlet mass spectrometry. *Limnology and Oceanography*, *43*(2), 334–339. https://doi.org/10.4319/lo.1998.43.2.0334

Liang, J.-H. H., Deutsch, C., McWilliams, J. C., Baschek, B., Sullivan, P. P., & Chiba, D. (2013). Parameterizing bubble-mediated air-sea gas exchange and its effect on ocean ventilation. *Global Biogeochemical Cycles*, *27*(3), 894–905. https://doi.org/10.1002/gbc.20080

Liang, J. H., Emerson, S. R., D'Asaro, E. A., McNeil, C. L., Harcourt, R. R., Sullivan, P. P., et al. (2017). On the role of sea-state in bubble-mediated air-sea gas flux during a winter storm. *Journal of Geophysical Research: Oceans*, *122*(4), 2671–2685. https://doi.org/10.1002/2016JC012408

Lockwood, D., Quay, P. D., Kavanaugh, M. T., Juranek, L. W., & Feely, R. A. (2012). High-resolution estimates of net community production and air-sea CO_2 flux in the northeast Pacific. *Global Biogeochemical Cycles*, *26*(GB4010). https://doi.org/10.1029/2012GB004380

Loose, B., & Jenkins, W. J. (2014). The five stable noble gases are sensitive unambiguous tracers of glacial meltwater. *Geophysical Research Letters*, *41*, 2835–2841. https://doi.org/doi:10.1002/2013GL058804

Loose, B., McGillis, W. R., Perovich, D., Zappa, C. J., & Schlosser, P. (2014). A parameter model of gas exchange for the seasonal sea ice zone. *Ocean Science*, *10*(1), 17–28. https://doi.org/10.5194/os-10-17-2014

Manning, C. C., Stanley, R. H. R., Nicholson, D. P., Loose, B., Lovely, A., Schlosser, P., & Hatcher, B. G. (2017). Changes in gross oxygen production, net oxygen production, and air-water gas exchange during seasonal ice melt in the Bras d'Or Lake, a Canadian estuary. *Biogeosciences Discussions*. https://doi.org/10.5194/bg-2017-428

McNeil, C., D'Asaro, E., Johnson, B., & Horn, M. (2006a). A gas tension device with response times of minutes. *Journal of Atmospheric and Oceanic Technology*, *23*(11), 1539–1558.

1383   https://doi.org/10.1175/JTECH1974.1

1384 McNeil, C., Katz, D. R., Ward, B., McGillis, W. R., & Johnson, B. D. (2006b). A method to
1385   estimate net community metabolism from profiles of dissolved O2 and N2. *Hydrobiologia*,
1386   *571*(1), 181–190. https://doi.org/10.1007/s10750-006-0236-7

1387 McNeil, C. L., Johnson, B. D., & Farmer, D. M. (1995). In situ measurement of dissolved
1388   nitrogen and oxygen in the ocean. *Deep-Sea Research Part I*, *42*(5), 819–826.
1389   https://doi.org/10.1016/0967-0637(95)97829-W

1390 Mordy, C. W., Cokelet, E. D., Robertis, A. De, Jenkins, R., Kuhn, C. E., Lawrence-Salvas, N., et
1391   al. (2017). Advances in Ecosystem Research: Saildrone Surveys of Oceanography, Fish,
1392   and Marine Mammals in the Bering Sea. *Oceanography*, *30*(2), 113–115.

1393 Munro, D. R., Quay, P. D., Juranek, L. W., & Goericke, R. (2013). Biological production rates
1394   off the Southern California coast estimated from triple O 2 isotopes and O 2 : Ar gas ratios.
1395   *Limnology and Oceanography*, *58*(4), 1312–1328.
1396   https://doi.org/10.4319/lo.2013.58.4.1312

1397 Nicholson, D., Emerson, S., Caillon, N., Jouzel, J., & Hamme, R. C. (2010). Constraining
1398   ventilation during deepwater formation using deep ocean measurements of the dissolved gas
1399   ratios 40 Ar/ 36 Ar, N 2 /Ar, and Kr/Ar. *Journal of Geophysical Research*, *115*(C11015), 1–
1400   15. https://doi.org/10.1029/2010jc006152

1401 Nilsson, E. D., Rannik, Ü., Swietlicki, E., Leck, C., Aalto, P. P., Zhou, J., & Norman, M. (2001).
1402   Turbulent aerosol fluxes over the Arctic Ocean 2. Wind-driven sources from the sea.
1403   *Journal of Geophysical Research*, *106*(D23), 32139–32154.

1404 Palevsky, H. I., Quay, P. D., Lockwood, D. E., & Nicholson, D. P. (2016). The annual cycle of
1405   gross primary production, net community production, and export efficiency across the
1406   North Pacific Ocean. *Global Biogeochemical Cycles*, *30*(2), 361–380.
1407   https://doi.org/10.1002/2015GB005318

1408 Pelland, N. A., Eriksen, C. C., Emerson, S. R., & Cronin, M. F. (2018). Seaglider surveys at
1409   Ocean Station Papa: Oxygen kinematics and upper-ocean metabolism. *Journal of*
1410   *Geophysical Research: Oceans*, 1–20. https://doi.org/10.1029/2018JC014091

1411 Plant, J. N., Johnson, K. S., Sakamoto, C. M., Jannasch, H. W., Coletti, L. J., Riser, S. C., &
1412   Swift, D. D. (2016). Net community production at Ocean Station Papa observed with nitrate
1413   and oxygen sensors on profiling floats. *Global Biogeochemical Cycles*, *30*, 859–879.
1414   https://doi.org/10.1002/2015GB005349.Received

1415 Reed, A., McNeil, C., D'Asaro, E., Altabet, M., Bourbonnais, A., & Johnson, B. (2018). A gas
1416   tension device for the mesopelagic zone. *Deep-Sea Research Part I*, *139*(2018), 68–78.
1417   https://doi.org/10.1016/j.dsr.2018.07.007

1418 Reynolds, R. W., Smith, T. M., Liu, C., Chelton, D. B., Casey, K. S., & Schlax, M. G. (2007).
1419   Daily High-Resolution-Blended Analyses for Sea Surface Temperature. *Journal of Climate*,
1420   *20*, 5473-5496.

1421 Rosengard, S. Z., Izett, R. W., Burt, W. J., Schuback, N., & Tortell, P. D. (2020). Decoupling of
1422   O 2 / Ar and particulate organic carbon dynamics in nearshore surface ocean waters.
1423   *Biogeosciences*, *17*, 3277–3298. Retrieved from https://doi.org/10.5194/bg-17-3277-2020

1424 Scheifele, B., Waterman, S., Merckelbach, L., & Carpenter, J. R. (2018). Measuring the
1425   Dissipation Rate of Turbulent Kinetic Energy in Strongly Stratified, Low-Energy
1426   Environments: A Case Study From the Arctic Ocean. *Journal of Geophysical Research:*
1427   *Oceans*, *123*, 5459–5480. https://doi.org/10.1029/2017JC013731

1428 Schmidtko, S., Johnson, G. C., & Lyman, J. M. (2013). MIMOC: A global monthly isopycnal
1429   upper-ocean climatology with mixed layers. *Journal of Geophysical Research: Oceans*,
1430   *118*, 1658–1672.

1431 Shigemitsu, M., Gruber, N., Oka, A., & Yamanaka, Y. (2016). Potential use of the N2/Ar ratio as
1432   a constraint on the oceanic fixed nitrogen loss. *Global Biogeochemical Cycles*, *30*, 576–594.
1433   https://doi.org/10.1111/1462-2920.13280

1434 Sipler, R. E., Gong, D., Baer, S. E., Sanderson, M. P., Roberts, Q. N., Mulholland, M. R., &
1435   Bronk, D. A. (2017). Preliminary estimates of the contribution of Arctic nitrogen fixation to
1436   the global nitrogen budget. *Limnology and Oceanography Letters*, *2*(5), 159–166.
1437   https://doi.org/10.1002/lol2.10046

1438 Steiner, N., Vagle, S., Denman, K. L., & McNeil, C. (2007). Oxygen and nitrogen cycling in the
1439   northeast Pacific - Simulations and observations at Station Papa in 2003/2004. *Journal of*
1440   *Marine Research*, *65*(3), 441–469. https://doi.org/10.1357/002224007781567658

1441 Tang, W., Wang, S., Fonseca-Batista, D., Dehairs, F., Gifford, S., Gonzalez, A. G., et al. (2019).
1442   Revisiting the distribution of oceanic N 2 fixation and estimating diazotrophic contribution
1443   to marine production. *Nature Communications*, *10*(1), 1–10.
1444   https://doi.org/10.1038/s41467-019-08640-0

1445 Tang, W., Cerdán-García, E., Berthelot, H., Polyviou, D., Wang, S., Baylay, A., et al. (2020).
1446   New insights into the distributions of nitrogen fixation and diazotrophs revealed by high-
1447   resolution sensing and sampling methods. *ISME Journal*. https://doi.org/10.1038/s41396-
1448   020-0703-6

1449 Teeter, L., Hamme, R. C., Ianson, D., & Bianucci, L. (2018). Accurate Estimation of Net
1450   Community Production From O2/Ar Measurements. *Global Biogeochemical Cycles*, 1–19.
1451   https://doi.org/10.1029/2017GB005874

1452 Tengberg, A., Hovdenes, J., Andersson, H. J., Brocandel, O., Diaz, R., Hebert, D., et al. (2006).
1453   Evaluation of a lifetime-based optode to measure oxygen in aquatic systems. *Limnology and*
1454   *Oceanography: Methods*, *4*(2), 7–17. https://doi.org/10.4319/lom.2006.4.7

1455 Top, Z., Martin, S., & Becker, P. (1988). A labratory study of dissolved noble gas anomaly due
1456   to ice formation. *Geophysical Research Letters*, *15*(8), 796–799.

1457 Tortell, P. D. (2005). Dissolved gas measurements in oceanic waters made by membrane inlet
1458   mass spectrometry. *Limnology and Oceanography: Methods*, *3*, 24–37.
1459   https://doi.org/10.4319/lom.2005.3.24

1460 Tortell, P. D., Bittig, H. C., Körtzinger, A., Jones, E. M., & Hoppema, M. (2015). Biological and
1461   physical controls on N2, O2, and CO2 distributions in contrasting Southern Ocean surface
1462   waters. *Global Biogeochemical Cycles*, *29*, 994–1013.
1463   https://doi.org/10.1002/2014GB004975

1464 Ulfsbo, A., Cassar, N., Korhonen, M., van Heuven, S., Hoppema, M., Kattner, G., & Anderson,

1465   L. G. (2014). Late summer net community production in the central Arctic Ocean using
1466   multiple approaches. *Global Biogeochemical Cycles*, *28*, 1129–1148.
1467   https://doi.org/10.1002/2014GB004833

1468 Voermans, J. J., Babanin, A. V., Thomson, J., Smith, M. M., & Shen, H. H. (2019). Wave
1469   Attenuation by Sea Ice Turbulence. *Geophysical Research Letters*, *46*(12), 6796–6803.
1470   https://doi.org/10.1029/2019GL082945

1471 Wang, S., Kranz, S. A., Kelly, T. B., Song, H., Stukel, M. R., & Cassar, N. (2020). Lagrangian
1472   Studies of Net Community Production: The Effect of Diel and Multiday Nonsteady State
1473   Factors and Vertical Fluxes on O 2 /Ar in a Dynamic Upwelling Region. *Journal of*
1474   *Geophysical Research: Biogeosciences*, *125*(6), 1–19.
1475   https://doi.org/10.1029/2019jg005569

1476 Wanninkhof, R. (2014). Relationship between wind speed and gas exchange over the ocean
1477   revisited. *Limnology and Oceanography: Methods*, *12*(6), 351–362.
1478   https://doi.org/10.1029/92JC00188

1479 Weeding, B., & Trull, T. W. (2014). Hourly oxygen and total gas tension measurements at the
1480   Southern Ocean Time Series site reveal winter ventilation and spring net community
1481   production. *Journal of Geophysical Research: Oceans*, *119*, 348–358.
1482   https://doi.org/10.1002/2013JC009302

1483 Weiss, R. F. (1970). The solubility of nitrogen, oxygen and argoninwater and seawater. *Deep Sea*
1484   *Research*, *17*(4), 721–735.

1485 Whalen, C. B., Talley, L. D., & MacKinnon, J. A. (2012). Spatial and temporal variability of
1486   global ocean mixing inferred from Argo profiles. *Geophysical Research Letters*, *39*(17).
1487   https://doi.org/10.1029/2012GL053196

1488 Wise, D. L., & Houghton, G. (1966). The diffusion coefficients of ten slightly soluble gases in
1489   water at 10-60°C. *Chemical Engineering Science*, *21*(11), 999–1010.
1490   https://doi.org/10.1016/0009-2509(66)85096-0

1491 Woolf, D. K., & Thorpe, S. A. (1991). Bubbles and the air-sea exchange of gases in near-
1492   saturation conditions. *Journal of Marine Research*, *49*, 435–466.
1493   https://doi.org/10.1357/002224091784995765

1494 Wu, J., Chen, N., Hong, H., Lu, T., Wang, L., & Chen, Z. (2013). Direct measurement of
1495   dissolved N2 and denitrification along a subtropical river-estuary gradient, China. *Marine*
1496   *Pollution Bulletin*, *66*(2013), 125–134. https://doi.org/10.1016/j.marpolbul.2012.10.020

1497 Yang, B., Emerson, S. R., & Bushinsky, S. M. (2017). Annual net community production in the
1498   subtropical Pacific Ocean from in-situ oxygen measurements on profiling floats. *Global*
1499   *Biogeochemical Cycles*, *31*, 728–744. https://doi.org/10.1002/2016GB005545

1500 Zhou, J., Delille, B., Brabant, F., & Tison, J. L. (2014). Insights into oxygen transport and net
1501   community production in sea ice from oxygen, nitrogen and argon concentrations.
1502   *Biogeosciences*, *11*, 5007–5020. https://doi.org/10.5194/bg-11-5007-2014

1503

ΔO₂/N₂' as a Tracer of Mixed Layer Net Community Production: Theoretical Considerations and Proof-of-Concept

Robert W. Izett[1] & Philippe D. Tortell[1,2]

[1.] Department of Earth, Ocean and Atmospheric Sciences, University of British Columbia, Vancouver, BC, Canada.

[2.] Botany Department, University of British Columbia, Vancouver, BC, Canada.

Contents of this file

Introduction

This supporting information provides supplementary figures, tables and explanations for the interpretation of the main text. Additional formulae derivations (S1) and error analyses (S2, Table S2) are also presented. A more detailed description of field applications of the N_2' approach presented in the main text is provided in section S3, with accompanying Matlab code and examples in a toolbox repository (available at *https://doi.org/10.5281/zenodo.4024952*, with link to *github.com/rizett/O2N2_NCP_toolbox* repository). Matlab code and output from the 1D numerical simulations described in the main text are also provided at the same repository.

S1. One-dimensional mixed layer physical gas model

As per Eq. 2 in the main text, we applied the following mixed layer budget to O_2, Ar and N_2:

$$MLD \cdot \frac{dC}{dt} = F_d + F_B + F_M. \tag{S1.1}$$

In this equation, MLD is the mixed layer depth (m), dC/dt represents the change in gas concentration over time resulting from physical processes, F_d represents the diffusive air-sea exchange flux, F_B is the combined small and large bubble fluxes (representing air-sea exchange processes via complete bubble injection, F_C, or partial exchange, F_P, respectively), and F_M is the sum of vertical diapycnal mixing (F_k), upwelling (F_w) and entrainment during mixed layer deepening (F_e). We used the model of Liang et al. (2013) to parameterize the air-sea exchange terms (F_d, F_c and F_p) in ice-free waters, and the model of Butterworth & Miller (2016) (which excludes explicit bubble fluxes) in partially-ice covered waters. We estimated the vertical mixing terms from subsurface gas concentrations (C_{deep}) and mixing rates as described in the main text. Equation S1.1 can be expanded as:

$$MLD \cdot \frac{dC}{dt} = F_d + F_C + F_P + F_k + F_w + F_e. \tag{S1.2}$$

$$MLD \cdot \frac{dC}{dt} = \left[k_d \left(C_{eq} \cdot \frac{SLP}{1\,atm} - C \right) \right] + \left[\beta \cdot k_p \left(C_{eq} \cdot (1 + \Delta P) \cdot \frac{SLP}{1\,atm} - C \right) + \beta \cdot F_c \right] + \left[\kappa_Z \cdot \frac{dC}{dz} \right] + \left[\omega \cdot \frac{dC}{dz} \cdot MLD \right] + \left[\frac{dMLD}{dt} \cdot (C_{deep} - C) \right] \tag{S1.3}$$

where k_d and k_p are the diffusive and bubble-mediated air-sea exchange coefficients, ΔP is the supersaturation increase caused by partially-dissolving bubbles, and F_C is the small bubble flux, all parameterized in Liang et al. (2013) and Butterworth & Miller (2016) (F_p and F_C are zero in ice-covered conditions). Sensitivity analyses comparing our simulation results with in-situ observations at Ocean Station Papa suggest that a bubble-mediated gas flux scaling coefficient, β, of 0.5 is appropriate, as in Yang et al. (2017) (see Fig. 5 in the main text). C_{eq} (mmol m^{-3}) is the gas solubility at equilibrium, per Garcia & Gordon (1993) for O_2 and Hamme & Emerson (2004) for Ar and N_2. SLP represents the sea level pressure (atm). The mixing terms are represented by the eddy diffusivity coefficient ($\kappa_{Z,}$; m^2 d^{-1}), advection velocity (ω, proportional to wind speed; m d^{-1}), the rate of mixed layer deepening (dMLD/dt; m d^{-1}), the surface-to-subsurface gas gradient (dC/dZ = (C_{deep} − C)/dZ; mmol m^{-4}) and the deep gas concentration (C_{deep}; mmol m^{-3}). We set Ar_{deep} and $N_{2,deep}$ values by adjusting subsurface ΔAr and $\Delta N_2/Ar$ (i.e. $\Delta N_2/Ar_{deep}$), while holding $O_{2,deep}$ constant at equilibrium concentrations (experimental simulations) or set to values based on observations (realistic simulations). The entrainment term is zero when the mixed layer shoals, and all mixing terms were set to zero in run a (no mixing) of the experimental and realistic simulations.

Matlab code for performing simulations with our 1D gas model is provided in the O2N2_NCP_toolbox on *Zenodo* (*https://doi.org/10.5281/zenodo.4024952*) and *GitHub* (*github.com/rizett/O2N2_NCP_toolbox*). Users can define forcing input (e.g. environmental data, initial conditions, and mixing coefficients) and experimental settings (e.g. see details in table 1 in the main text), and can specify the air-sea flux parameterization.

S1.2 N₂' budget: Quasi-steady-state conditions and estimating O₂ re-equilibration timescale

The N_2' term is derived by predicting N_2 and Ar divergence over a MLD O_2 re-equilibration time scale (defined below in Eq. S6.3), and subtracting this value from observed N_2 saturation. To derive N_2', we simplified the MLD budget described in Eq. S1 by combining all mixing processes into a single term. We set F_e to zero, and collapsed the remaining fluxes with a single coefficient, κ ($\kappa = \kappa_Z + \omega*dz$; $m^2\ d^{-1}$):

$$F_k + F_w + F_e \approx \frac{dC}{dZ}\kappa \tag{S2}$$

Combining Eqs. S1.2 and S2 yields the simplified budget used to perform N_2' calculations (Eq. 3 in the main text), which was evaluated over one O_2 re-equilibration time, τ_{O2} (Eq. S6.3), prior to observations (Fig. S2).

$$MLD \cdot \frac{dC}{dt} = \left[k_d\left(C_{eq} \cdot \frac{SLP}{1\ atm} - C\right)\right] + $$
$$\left[\beta \cdot k_p\left(C_{eq} \cdot (1 + \Delta P) \cdot \frac{SLP}{1\ atm} - C\right) + \beta \cdot F_c\right] + \frac{dC}{dZ}\kappa \tag{S3}$$

Using this budget, we calculated the expected divergence between Ar and N_2 saturation states at the end of the τ_{O2} time period, and subtracted this difference from the true ΔN_2 (Eq. 4 in the main text; Fig. S2). In the model setting, true ΔN_2 (i.e. ΔN_2^{true}) is the N_2 supersaturation anomaly predicted by the full MLD budget (Eq. S1), and in field studies, ΔN_2^{true} is the measured N_2 supersaturation. Figure S2 shows a representation of calculations performed with the full and condensed N_2' MLD budgets. The approach to estimating N_2' was repeated for all time points in the full model simulations. In field studies, calculations will be performed over the O_2 re-equilibration timeframe prior to each observation, in an analogous approach to calculations of a weighted piston velocity (Reuer et al., 2007). Matlab code, and example data are provided at *https://doi.org/10.5281/zenodo.4024952*. Refer to section S3 for further details.

The analytical solution to Eq. S3 describes the quasi-steady-state gas condition, and can be derived by further simplifying the gas budget to combine the air-sea exchange terms, following (Woolf, 1997) and Eq. 2 in Liang et al. (2013):

$$F_d + F_C + F_P \approx -k_T\left(C - C_{eq}(1 + \Delta_{eq})\frac{SLP}{1\ atm}\right) \tag{S4}$$

Here k_T is the pooled diffusive and bubble-mediated gas transfer coefficients (i.e. $k_d + \beta \cdot k_P$) and Δ_{eq} is the bubble-induced steady-state gas supersaturation. This approximation simplifies the derivation of the analytical solution, and matches the net air-sea flux predicted by the full parameterization (as in Eq. S1) with a relative accuracy of ~2 % over a range of wind speeds (0-25 m s⁻¹) and gas saturation states (90-110 %; results not shown). The analytical solution can subsequently be derived by discretizing the simplified gas budget into sufficiently short time

increments, dt, so that MLD, k_T, Δ_{eq}, C_{deep} and κ can be considered constant. Below, we derive the analytical solution to the simplified budget through the following steps:

1) Expand Eq. S3 with simplified gas flux terms.

$$\frac{dC}{dt} = \frac{-k_T}{MLD}\left(C - C_{eq}\left(1 + \Delta_{eq}\right)\frac{SLP}{1\,atm}\right) + \frac{C_{deep}-C}{dZ}\frac{\kappa}{MLD} \tag{S5.1}$$

2) Simplify k_T/MLD and $\kappa/(dZ \cdot MLD)$ as K_1 and K_2, respectively, and re-write the equation by combining terms.

$$\frac{dC}{dt} = -(K_1 + K_2)\cdot C + K_1 \cdot C_{eq} \cdot \left(1 + \Delta_{eq}\right)\frac{SLP}{1\,atm} + K_2 \cdot C_{deep} \tag{S5.2}$$

3) Further simplify by expressing $(K_1 + K_2)$ as P, $\left(K_1 \cdot C_{eq} \cdot \left(1 + \Delta_{eq}\right) \cdot \frac{SLP}{1\,atm} + K_2 \cdot C_{deep}\right)$ as Q, and dC/dt as C'. Apply an integration factor of e^{Pt}.

$$C' = -\mathrm{P}\cdot C + Q \tag{S5.3}$$

$$C' \cdot e^{Pt} + \mathrm{P}\cdot C \cdot e^{Pt} = Q \cdot e^{Pt} \tag{S5.4}$$

4) Note that $d/dt(C \cdot e^{Pt}) = C' \cdot e^{Pt} + \mathrm{P}\cdot C \cdot e^{Pt}$ by the product rule.

$$\frac{d}{dt}(C \cdot e^{Pt}) = Q \cdot e^{Pt} \tag{S5.5}$$

$$C \cdot e^{Pt} = Q \cdot \int e^{Pt}\, dt \tag{S5.6}$$

5) Since P and Q (defined above in step 3) are considered constant over dt, Eq. S5.6 can be integrated simply. In Eq. S5.7, R is the integration constant.

$$C = \frac{Q}{P} + R \cdot e^{-Pt} \tag{S5.7}$$

6) Finally, by setting C(t=0) to be the initial condition, C_0, we derive a single analytical solution, by re-substituting the simplifying terms (P and Q defined above in step 3) for the gas flux terms.

$$R = C_0 - \frac{Q}{P} \tag{S5.8}$$

$$C = \frac{k_T \cdot C_{eq}\cdot\left(1+\Delta_{eq}\right)\cdot\frac{SLP}{1\,atm}+\frac{\kappa}{dz}\cdot C_{deep}}{k_T+\frac{\kappa}{dz}}$$
$$+ \left(C_0 - \frac{k_T \cdot C_{eq}\cdot\left(1+\Delta_{eq}\right)\cdot\frac{SLP}{1\,atm}+\frac{\kappa}{dz}\cdot C_{deep}}{k_T+\frac{\kappa}{dz}}\right)\cdot e^{-\left(\frac{k_T}{MLD}+\frac{\kappa}{dz\,\cdot\,MLD}\right)t} \tag{S5.9}$$

When mixing is negligible (i.e. $\kappa \approx 0$ m^2 d^{-1}), Eq. S5.9 simplifies to

$$C = C_{eq} \cdot (1 + \Delta_{eq}) \cdot \frac{SLP}{1\,atm} + \left(C_0 - C_{eq} \cdot (1 + \Delta_{eq}) \cdot \frac{SLP}{1\,atm} \right) \cdot e^{-\left(\frac{k_T}{MLD}\right)t} \qquad \text{(S5.10)}$$

The analytical solution is useful for understanding quasi-steady-state gas conditions, and the rate of response to perturbations. For example, the quasi-steady-state gas concentration, C_{SS}, can be predicted from Eq. S5.9 as t approaches infinity, and C approaches the value of the first term:

$$C_{SS} = \frac{k_T \cdot C_{eq} \cdot (1 + \Delta_{eq}) \cdot \frac{SLP}{1\,atm} + \frac{\kappa}{dz} \cdot C_{deep}}{k_T + \frac{\kappa}{dz}} \qquad \text{(S5.11)}$$

Subsequently, the mixed layer O_2 re-equilibration timescale, τ_{O2}, can be estimated as the time required for air-sea gas exchange and vertical mixing processes to re-establish the quasi-steady-state condition. We thus estimated τ_{O2} by setting $(C - C_{SS}) / (C_0 - C_{SS})$ to be 0.01 (i.e. $C - C_{SS} << C_0 - C_{SS}$) and t to τ_{O2}:

$$C = C_{SS} + (C_0 - C_{SS}) \cdot e^{-\left(\frac{k_T}{MLD} + \frac{\kappa}{dz \cdot MLD}\right)\tau_{O2}} \qquad \text{(S6.1)}$$

$$\frac{C - C_{SS}}{C_0 - C_{SS}} = 0.01 = e^{-\left(\frac{k_T}{MLD} + \frac{\kappa}{dz \cdot MLD}\right)\tau_{O2}} \qquad \text{(S6.2)}$$

$$\tau_{O2} = \frac{-\ln(0.01) \cdot MLD}{\left(k_T + \frac{\kappa}{dz}\right)} \qquad \text{(S6.3)}$$

The MLD O_2 re-equilibration time calculated by this approach represents several MLD O_2 residence times, which is typically approximated by MLD/k_T.

Since the exponential weighting function used to calculate O_2 piston velocities is typically negligible after ~30 days (Teeter et al., 2018), calculation of gas transfer coefficients (i.e. Eq. 5 in the main text) will not be significantly impacted by the choice to weight k_{O2} over τ_{O2} or MLD/k_T. However, calculating τ_{O2} by this approach reflects the contribution of vertical mixing (proportional to κ) in reducing O_2 cycling in surface waters, and more fully represents the timeframe of gas re-equilibration within the MLD. This timescale, τ_{O2}, is therefore more appropriate for N_2' calculations relevant to NCP derivation. Indeed, when the N_2' calculations are performed over a timescale represented by MLD/k_T, differences between Ar and N_2 relevant to NCP calculations are not fully reconciled (Fig. S2b). In ocean environments, where MLD, k_T and κ vary in time, τ_{O2} should be estimated using 30- to 60-day weighted values for these terms, where possible, or from ship-based observations.

S2. Uncertainty analyses
S2.1 ΔN$_2$' parameter uncertainty

We performed a Monte Carlo analysis on the real-OSP and real-BB full mixing (run c) simulations to determine the contributions of individual and combined parameterization uncertainty to errors in $\Delta O_2/N_2'$. This analysis was conducted by randomly varying each of the input variables (wind speed, SST, SLP, MLD), air-sea flux (F_d, F_P, F_C, β) and mixing terms (κ, $\Delta N_2/Ar_{deep}$) in the N_2' MLD budget (Eq. S4 above, and Eq. 3 in the main text) around their estimated uncertainties (Table S1), and performing 100 (for individual parameter errors) or 1000 (for combined errors) iterations of N_2' calculations.

We used uncertainties of $\pm$ 2.5 m s^{-1}, $\pm$ 0.75 $^{\circ}$C and $\pm$ 2 mbar in the wind speed, SST and SLP data based on a comparison of in-situ observations (from ships, moorings and weather buoys) with various gridded products. For observations based in the Subarctic NE Pacific, the Cross-Calibrated Multi-Parameter (CCMP) wind speed product (provided by Remote Sensing Systems at *www.remss.com*; Atlas et al., 2011), NOAA High Resolution SST Dataset (provided by NOAA ESRL at https://psl.noaa.gov/; Reynolds et al., 2007), and NCEP/NCAR reanalysis 2 SLP (provided by NOAA ESRL at psl.noaa.gov; Kalnay et al., 1996) products compared best with observations from moorings in coastal and off-shore waters. In the Arctic, the NCEP/NCAR Reanalysis 2 wind product performed best.

The air-sea flux terms (F_d, F_P and F_C) depend on the choice of gas transfer parameterization. In the present study, we use the bubble-mediated model of Liang et al. (2013), as it was parameterized for O_2 and N_2, and is considered valid for gases with similarly low solubility. Over a range of wind speeds and temperatures, we estimate the relative uncertainty in these terms to be ~18-24 %, based on the standard deviation of values derived using several gas transfer parameterizations (Stanley et al., 2009; Sweeney et al., 2007; Vagle et al., 2010; Wanninkhof, 2014; Woolf, 1997). These errors are roughly consistent with Wanninkhof (2014), who estimated a mean total error in the air-sea gas flux of ~20 %. We therefore followed Bushinsky & Emerson (2015) by assigning a relative error of 15 % to F_d, F_P and F_C in our Monte Carlo analysis. Finally, we ascribed an error of $\pm$5 m to estimates of the MLD, following Izett et al. (2018), an error of $\pm$0.14 to β based on Emerson et al. (2019), and conservative uncertainties of $\pm10^{-5}$ m^2 s^{-1} and 0.25 % to

Overall, we find that uncertainty in the sea surface temperature product (mean 0.07 %) contributes the largest individual errors to $\Delta O_2/N_2'$. This is unsurprising as seasonal SST variability, which drives diffusive air-sea exchange, contributes to strong variability in $\Delta N_2/Ar$ (see main text). Errors in the mixing coefficient term were next greatest (mean 0.02 %), while errors in the bubble-flux terms (β, F_C, F_P) were generally small, due to the low prevalence of high wind speeds. Errors associated with these terms were typically larger during autumn to spring, when wind speeds were elevated. The combined uncertainty from all parameterizations is 0.09 %, on average, across both real-OSP and real-BB simulations.

S2.2 Assumption uncertainty

The N_2' approach assumes constant values of MLD, salinity, κ, and $\Delta N_2/Ar_{deep}$, based on the availability of data products and at-sea measurements (see main text for details). To evaluate the uncertainty in N_2' incurred by these assumptions, we compared calculations on the real-OSP and real-BB full mixing (run c) simulations in which these values were held constant against calculations in which they were allowed to vary, based on values in the full model simulations. Across both simulations, we found mean errors in $\Delta O_2/N_2'$ from these assumptions of 0.07 %

(range ~0.001 – 0.3; Table S1). This value is similar to the combined parameterization uncertainty, but can only be reduced through accurate estimation of the time-history of MLD, salinity κ, and $\Delta N_2/Ar_{deep}$ terms. This may not be feasible for many field measurement programs.

In general, the uncertainties associated with the N_2' assumptions were larger in the real-BB simulation (Fig. s9b) due to significant and rapid variability in subsurface temperature, and therefore subsurface N_2 and Ar concentrations, invoked in our model. These uncertainties, and the remaining biases in $\Delta N_2'/Ar$ ($\Delta O_2/Ar - \Delta O_2/N_2'$ almost as large as $\Delta O_2/Ar - \Delta O_2/N_2$ in Fig. s9b), are likely represent the upper range errors in the approach presented here, as subsurface inert gas concentrations likely do not vary as much in reality as they do in our modeled environment. In the absence of time-series observations of subsurface gas concentrations in Baffin Bay, we necessarily set $N_{2,deep}$ and Ar_{deep} equivalent to their equilibrium concentrations at the time-variable temperature and salinity conditions of the deep box layer. The large amplitude in temperature variability in this deep box layer results from significant shoaling of the MLD as the model progresses into summer months, and contributed to significant variability in subsurface N_2 and Ar concentrations. As the N_2' approach assumes these values are constant over the duration of calculations, failure to represent this variability will result in large remaining biases in $\Delta N_2'/Ar$. If deep gas concentrations do not vary to such large degrees in reality, the errors in N_2' would be significantly smaller, as in the real-OSP simulation.

S2.3 Uncertainty from N_2-fixation

We estimated the potential uncertainty in N_2' and $\Delta O_2/N_2'$ due to N_2-fixation by applying constant rates of N_2 removal (see main text for details) in 1D model simulations without vertical mixing over a range of constant u_{10} and SST. We compared the steady-state ΔN_2 from these runs against values obtained with N_2-fixation rates of zero. For the upper range of N_2-fixation observed in the ocean, we calculate a maximum steady-state deviation of ~0.3 % at very low wind speeds, but values are always less than 0.05 % above wind speeds of 6 m s^{-1} (Fig. S8c). Applying a constant N_2-fixation rate equivalent to the global observed maximum (see main text) to the real-OSP full mixing run resulted in deviations of less than 0.05 % in N_2 saturation when compared against the run excluding N_2-fixation. We thus conclude that N_2-fixation will have a negligible effect on $\Delta O_2/N_2'$ calculations in most oceanic waters.

S2.4 Total uncertainty

Our error analyses produce a total average uncertainty in $\Delta O_2/N_2'$ of 0.01 % (range 0.04 – 0.3; Table 1) resulting from the parameterization and assumption errors. On average, this is smaller than the offset between $\Delta O_2/Ar$ and uncorrected $\Delta O_2/N_2$. The upper range of uncertainty in $\Delta O_2/N_2'$ (including potential contributions from N_2-fixation) is represented in Fig. S9, which presents $\Delta O_2/Ar - \Delta O_2/N_2'$ from the realistic OSP and BB simulations (full mixing scenario / run c only). Since the assumption errors contribute the largest proportion to total $\Delta N_2'$ uncertainty, the total error in $\Delta O_2/N_2'$ is smallest when these values are small during periods of reduced MLD, κ and $\Delta N_2/Ar_{deep}$ variability (see Figs. 3-4 in the main text). In field studies, the error approximated here and potential uncertainty from in-situ O_2 and N_2 measurement accuracy will contribute to total uncertainty in $\Delta O_2/N_2'$.

We exclude the RMSE derived from the N_2 validation against observations (0.9 %; see main text) from the total estimated N_2' uncertainty, as this likely over-estimates the relative differences between Ar and N_2.

S3 Application of the N_2' approach to field data

In field-based applications, derivation of N_2' estimates requires measurements of surface gas concentrations (N_2), hydrographic data (temperature and salinity) and best estimates of the MLD and the mixing terms κ and $\Delta N_2/Ar_{deep}$ at the time of sampling. MLD can be derived by interpolating between CTD casts or using climatological datasets, whereas mixing terms can be estimated from observations, numerical models or archived datasets (see main text for details). Information on ocean conditions (SST, u_{10}, and SLP) prior to gas measurements, during the O_2 re-equilibration time frame (typically ~60-90 days in ice-free waters; Eq. 6.3), are also necessary to perform calculations. These "historic" data can be obtained from reanalysis or satellite products. The MLD, κ and $\Delta N_2/Ar_{deep}$ will commonly be assumed constant backwards in time, based on values at the time of ship-board gas observation, or based on alternative sources (see main text).

In Eq. 4 in the main text, ΔN_2^{obs} is the measured gas supersaturation condition, and ΔN_2^{est} and ΔAr^{est} are predicted by the calculations described above in section S1.2. N_2' calculations are performed in a similar approach to piston velocity weighting (Reuer et al., 2007), and the weighting function (Eq. 4 in Teeter et al., 2018) should be applied to the historic estimates of wind speed and κ when evaluating the O_2 re-equilibration and N_2' timescale from Eq. 6.3. All input data should have the same spatial resolution as continuous O_2/N_2 observations, with N_2' calculations applied independently to each underway gas measurement.

In using our Matlab codes (with examples in the O2N2_NCP_toolbox; *https://doi.org/10.5281/zenodo.4024952*), users provide the historic datasets, observed ΔN_2, and specify the gas transfer parameterization (including β gas scaling term) best suited to their region of study. These codes can be used as templates for future studies, and can be modified to incorporate future developments. The main codes we provided were written by R. Izett, with additional scripts cited accordingly.

References

Atlas, R., Hoffman, R. N., Ardizzone, J., Leidner, S. M., Jusem, J. C., Smith, D. K., & Gombos, D. (2011). A cross-calibrated, multiplatform ocean surface wind velocity product for meteorological and oceanographic applications. *Bulletin of the American Meteorological Society*, *92*, 157–174. https://doi.org/10.1175/2010BAMS2946.1

Bushinsky, S. M., & Emerson, S. (2015). Marine biological production from in situ oxygen measurements on a profiling float in the subarctic Pacific Ocean. *Global Biogeochemical Cycles*, *29*, 2050–2060. https://doi.org/10.1002/2015GB005251

Butterworth, B. J., & Miller, S. D. (2016). Air-sea exchange of carbon dioxide in the Southern Ocean and Antarctic marginal ice zone. *Geophysical Research Letters*, *43*, 7223–7230. https://doi.org/10.1002/2016GL069581

Emerson, S., Yang, B., White, M., & Cronin, M. (2019). Air-Sea Gas Transfer: Determining Bubble Fluxes With In Situ N2 Observations. *Journal of Geophysical Research: Oceans*, *124*(4), 2716–2727. https://doi.org/10.1029/2018JC014786

Garcia, H. E., & Gordon, L. I. (1993). Erratum: Oxygen solubility in seawater: better fitting equations. *Limnology and Oceanography*, *38*, 656.

Hamme, R. C., & Emerson, S. R. (2004). The solubility of neon , nitrogen and argon in distilled water and seawater. *Deep-Sea Research Part I*, *51*, 1517–1528. https://doi.org/10.1016/j.dsr.2004.06.009

Izett, R., Manning, C. C., Hamme, R. C., & Tortell, P. D. (2018). Refined estimates of net community production in the Subarctic Northeast Pacific derived from ΔO2/Ar measurements with N2O-based corrections for vertical mixing. *Global Biogeochemical Cycles*, *32*, 326–350. https://doi.org/https://doi.org/10.1002/2017GB005792

Kalnay, E., Kanamitsu, M., Kistler, R., Collins, W., Deaven, D., Gandin, L., et al. (1996). The NCEP/NCAR 40-year reanalysis project. *Bulletin of the American Meteorological Society*, *77*, 437–471. https://doi.org/10.1175/1520-0477(1996)077<0437:TNYRP>2.0.CO;2

Liang, J.-H. H., Deutsch, C., McWilliams, J. C., Baschek, B., Sullivan, P. P., & Chiba, D. (2013). Parameterizing bubble-mediated air-sea gas exchange and its effect on ocean ventilation. *Global Biogeochemical Cycles*, *27*(3), 894–905. https://doi.org/10.1002/gbc.20080

Reuer, M. K., Barnett, B. A., Bender, M. L., Falkowski, P. G., & Hendricks, M. B. (2007). New estimates of Southern Ocean biological production rates from O_2/Ar ratios and the triple isotope composition of O_2. *Deep Sea Research I*, *54*(2007), 951–974. https://doi.org/10.1016/j.dsr.2007.02.007

Reynolds, R. W., Smith, T. M., Liu, C., Chelton, D. B., Casey, K. S., & Schlax, M. G. (2007). Daily High-Resolution-Blended Analyses for Sea Surface Temperature. *Journal of Climate*, *20*, 5473-5496.

Stanley, R. H. R., Jenkins, W. J., Lott, D. E., & Doney, S. C. (2009). Noble gas constraints on air-sea gas exchange and bubble fluxes. *Journal of Geophysical Research: Oceans*, *114*(11), 1–14. https://doi.org/10.1029/2009JC005396

Sweeney, C., Gloor, E., Jacobson, A. R., Key, R. M., McKinley, G., Sarmiento, J. L., & Wanninkhof, R. (2007). Constraining global air–sea gas exchange for CO2 with recent bomb 14C measurements. *Global Biogeochemical Cycles*, *21*(GB2015). https://doi.org/doi:10.1029/2006GB002784

Teeter, L., Hamme, R. C., Ianson, D., & Bianucci, L. (2018). Accurate Estimation of Net Community Production From O2/Ar Measurements. *Global Biogeochemical Cycles*, 1–19. https://doi.org/10.1029/2017GB005874

Vagle, S., McNeil, C., & Steiner, N. (2010). Upper ocean bubble measurements from the NE Pacific and estimates of their role in air-sea gas transfer of the weakly soluble gases nitrogen and oxygen, *115*, C12054. https://doi.org/10.1029/2009JC005990

Wang, S., Kranz, S. A., Kelly, T. B., Song, H., Stukel, M. R., & Cassar, N. (2020). Lagrangian Studies of Net Community Production: The Effect of Diel and Multiday Nonsteady State Factors and Vertical Fluxes on O 2 /Ar in a Dynamic Upwelling Region. *Journal of Geophysical Research: Biogeosciences*, *125*(6), 1–19. https://doi.org/10.1029/2019jg005569

Wanninkhof, R. (2014). Relationship between wind speed and gas exchange over the ocean revisited. *Limnology and Oceanography: Methods*, *12*(6), 351–362. https://doi.org/10.1029/92JC00188

Woolf, D. K. (1997). *Bubbles and their role in gas exchange. The Sea Surface and Global Change*. https://doi.org/10.1017/cbo9780511525025.007

Yang, B., Emerson, S. R., & Bushinsky, S. M. (2017). Annual net community production in the subtropical Pacific Ocean from in-situ oxygen measurements on profiling floats. *Global Biogeochemical Cycles*, *31*, 728–744. https://doi.org/10.1002/2016GB005545
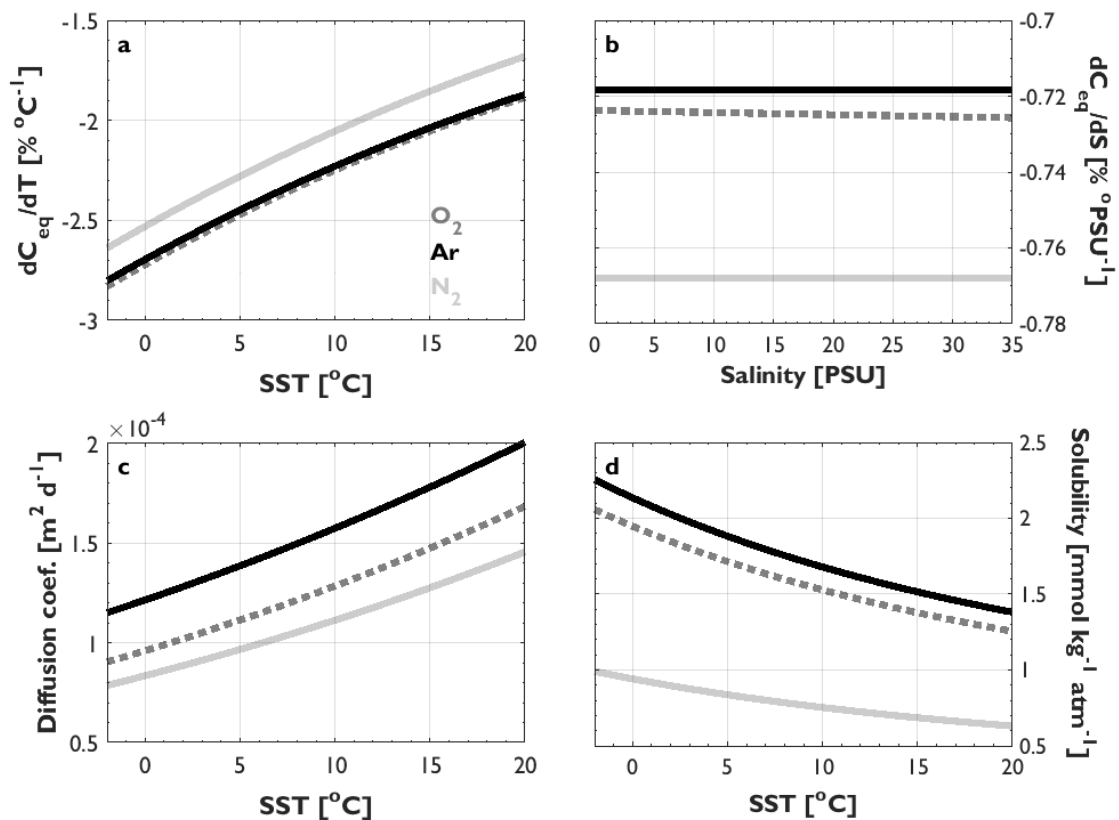
Figure S1. The differential physical properties of O_2 (dotted grey), Ar (black) and N_2 (solid grey) across a range of temperatures and salinities. Panels (a) and (b) represent the solubility-temperature and -salinity dependence of each gas, respectively, panel (c) presents their air-sea diffusion exchange coefficients, and panel (d) shows the Henry's Law solubility for each gas in one standard atmosphere of dry air. Lines represent average values over a salinity range of 0-35 PSU (panels a, c and d) or a temperature range of -2 to 10 °C (panel b).
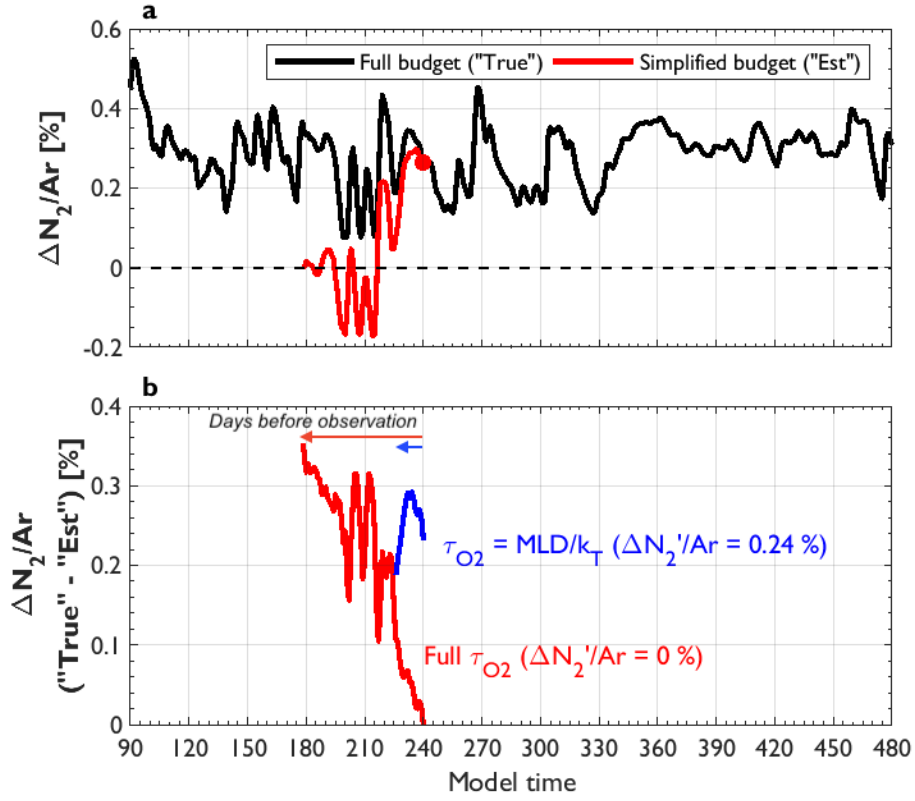
Figure S2. An example of the application of the N_2' approach. Panel (a) shows $\Delta N_2/Ar$ predicted in a full model simulation (i.e. based on ΔN_2^{true} and ΔAr from a real-OSP simulation with mixing; black line), and one example of values calculated using ΔN_2^{est} and ΔAr^{est} (red line, Eq. 4 in the main text) derived by evaluating the N_2' budget over the O_2 re-equilibration timescale, τ_{O2} before the time of observation (Eq. 3 in the main text and Eq. S3 above). $\Delta N_2'$ was estimated by subtracting the estimated difference between ΔN_2 and ΔAr (i.e. $\Delta N_2^{est} - \Delta Ar^{est}$) obtained from the simplified model from ΔN_2^{true} at the time marked by the red dot. This was repeated for all time points obtained from the full model simulation. Panel (b) represents the difference in $\Delta N_2/Ar$ predicted by the full model and the simplified model over the time frame of calculations. Two sets of calculations are shown: one for the full τ_{O2} (estimated from Eq. S6.3) and one set performed over an O_2 residence time, approximated as MLD/k_{O2}. Note that the latter is too short of a time period to fully-reconcile ΔN_2 and ΔAr differences relevant to NCP calculations.

12
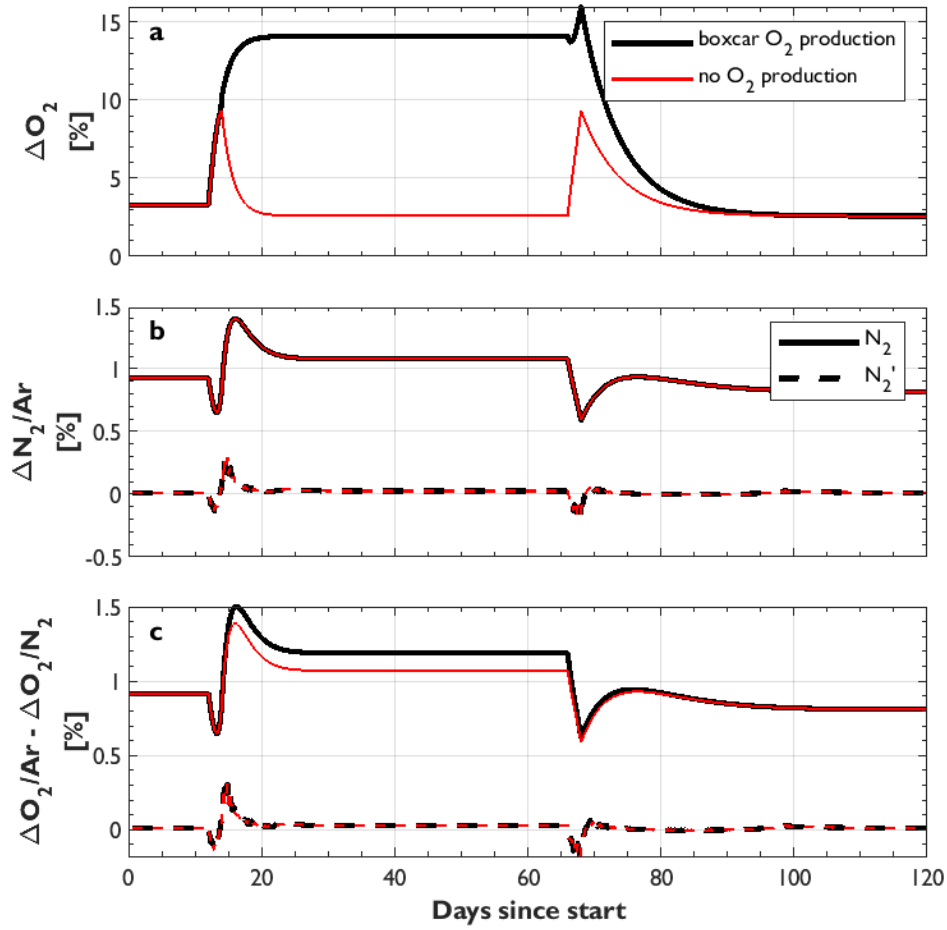
Figure S3. Results from a numerical simulation (Ex-IF 3) exploring the impact of biological O_2 production on surface gas concentrations. Black and red lines represent simulation results obtained with (black) and without (red) biological O_2 production (20 mmol O_2 m^{-2} d^{-1}). Productivity transients were applied as a boxcar step change corresponding with the changes in environmental forcing (Table 1). The results represented by the red lines correspond with the results presented in Fig. 2c in the main text. Panels (b) and (c) demonstrate that the N_2' approach is equally skillful in representing excess ΔN_2 with both high and low rates of biological O_2 production, and that $\Delta N_2'$ is insensitive to ΔO_2.
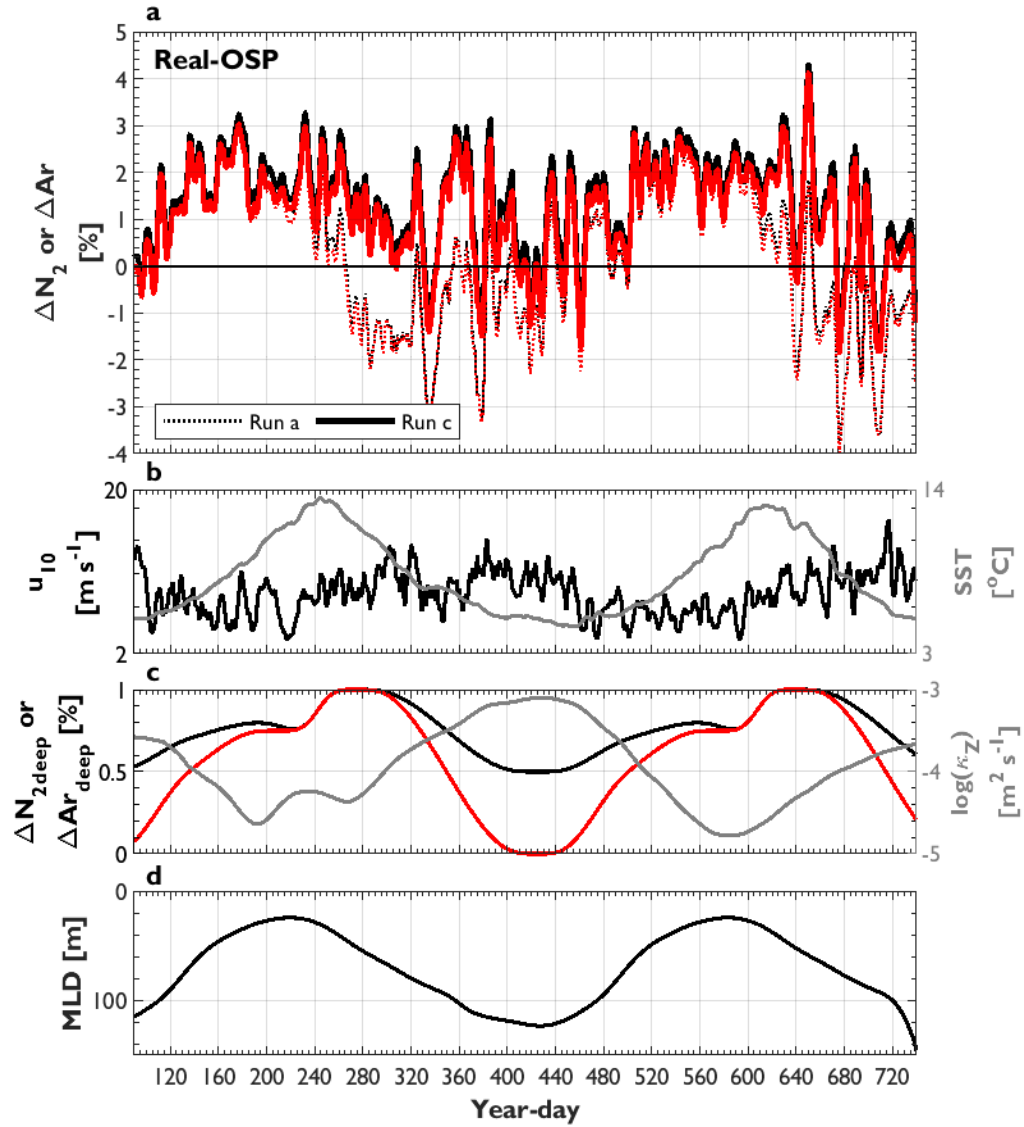
Figure S4. ΔN₂ (black) and ΔAr (red) in the realistic OSP simulation, with corresponding forcing parameters. In panel (a), solid lines represent output from the full-mixing simulation (i.e. run c), and dotted lines represent output from simulations with no mixing (run a). In panel (c), the black line represents subsurface ΔN₂, while the red line represents subsurface ΔAr. The x-axes represent April 2011-Jan. 2013. Refer to Figs. 3, 4 and Table 1 in the main text for further details.
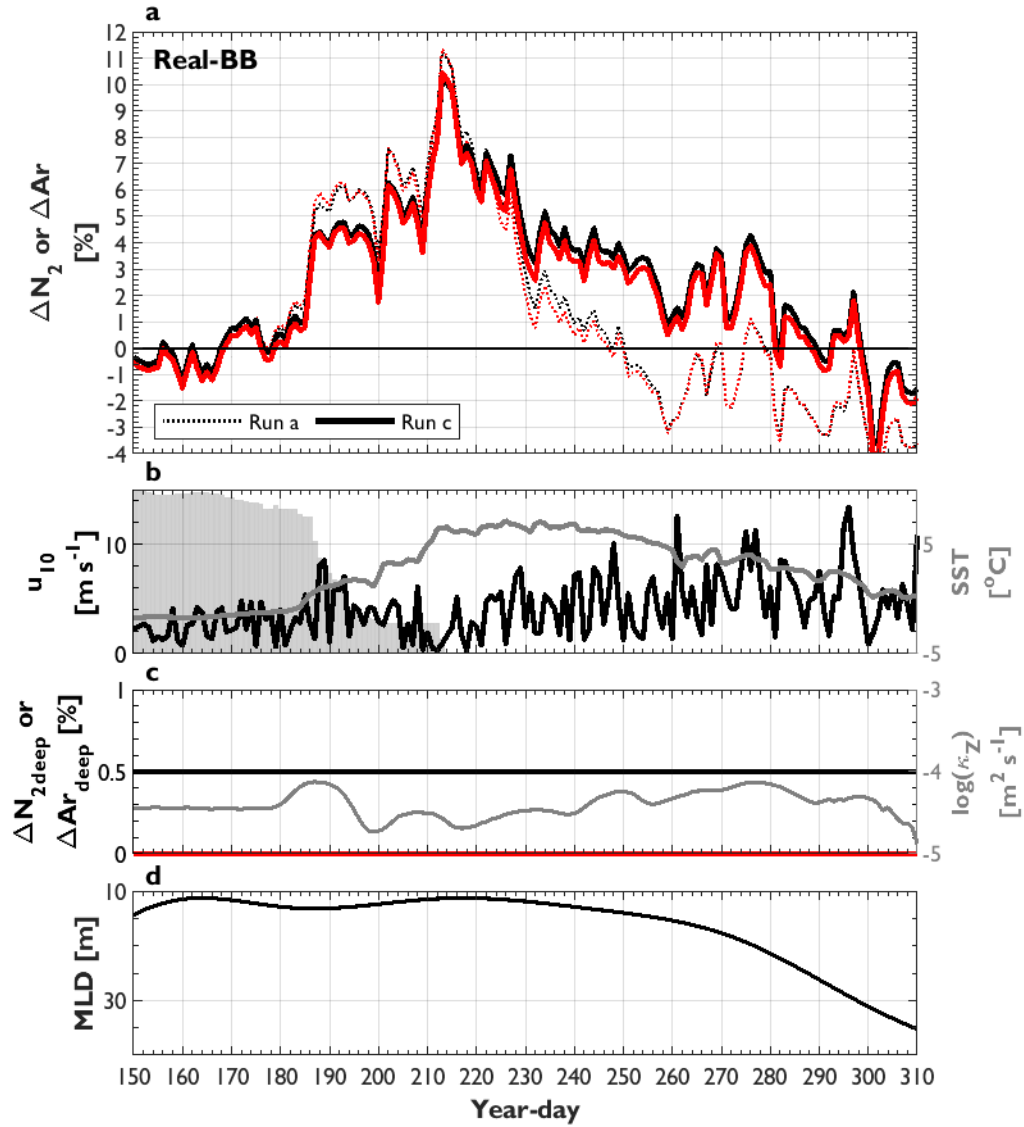
Figure S5. ΔN_2 (black) and ΔAr (red) in the realistic BB simulation, with corresponding forcing parameters. The x-axes represent 2019 year-day. Refer to Fig. S4 (above) and Figs. 3, 4 and Table 1 in the main text for further details.
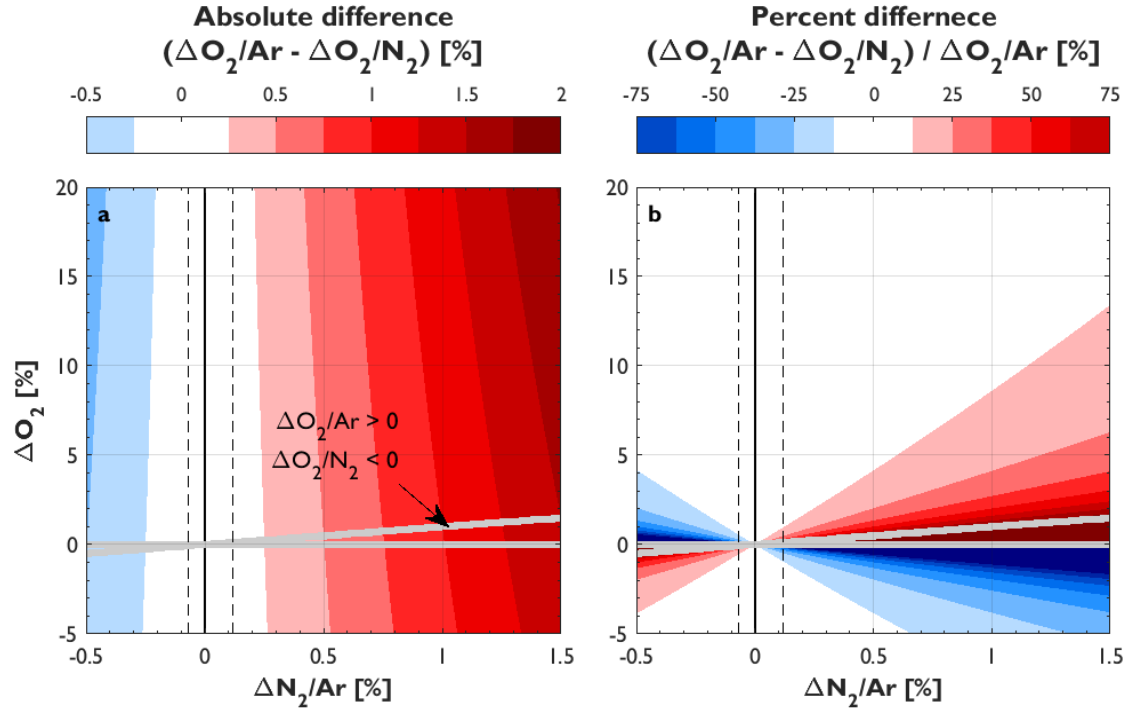
Figure S6. The absolute (a) and relative (b) differences between $\Delta O_2/Ar$ and $\Delta O_2/N_2$ over a realistic range of surface ΔO_2 in the ocean, and $\Delta N_2/Ar$ produced in the model simulations. Differences represent uncertainty in NCP estimates derived from O_2/N_2 if corrections for excess N_2 supersaturation are not made. The grey outlined region in both panels represents scenarios where $\Delta O_2/Ar$ and $\Delta O_2/N_2$ have opposite signs, leading to false interpretation of net tropic status from $\Delta O_2/N_2$. measurements. The vertical dashed lines represent the range of $\Delta N_2'/Ar$ (i.e. after correcting for excess N_2 supersaturation) in the realistic model simulations.
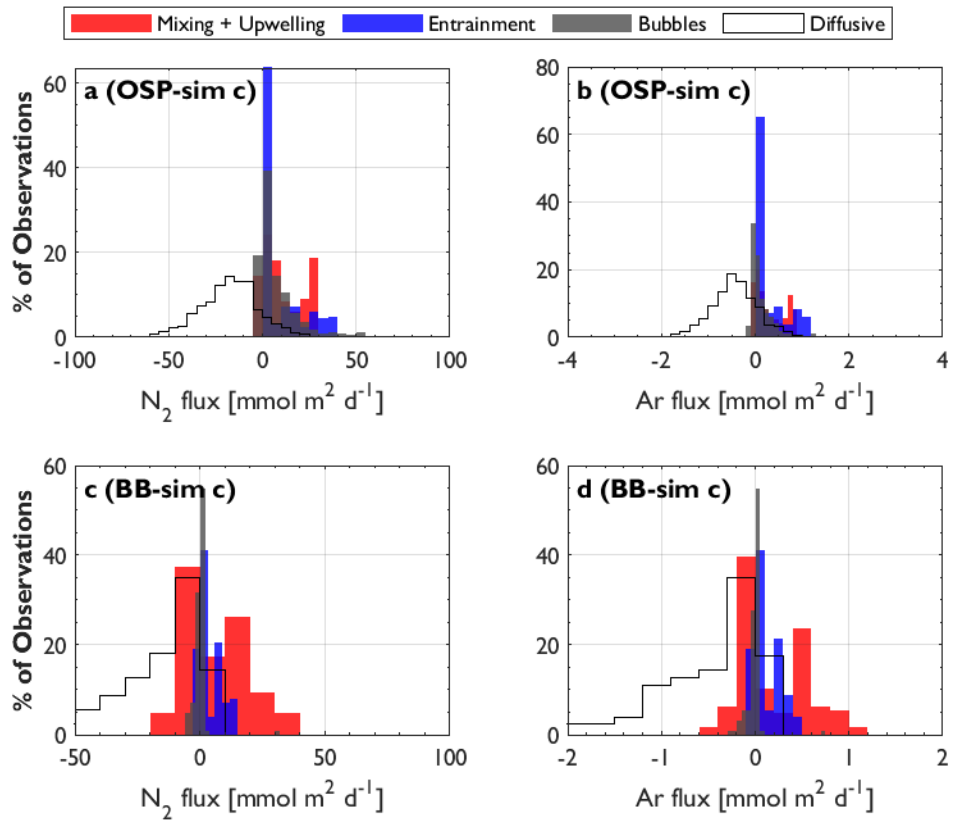
Figure S7. The frequency distribution of mixed layer fluxes in the realistic real-OSP (a, b) and real-BB (c, d) model run c (left = N$_2$; right = Ar). A positive flux represents an increase in the gas in the mixed layer.
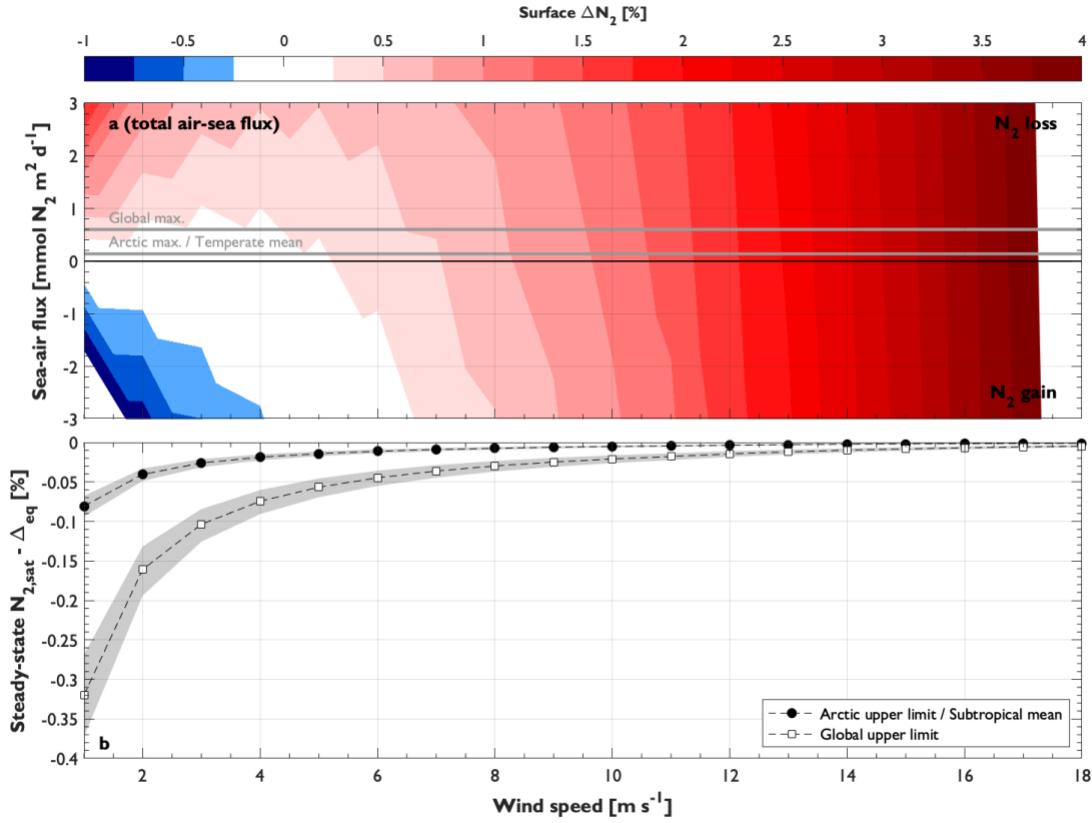
Figure S8. Relative importance of N_2 fixation and sea-air flux on surface N_2 supersaturation. Panel (a) shows the effect of total sea-to-air flux at various wind speeds, based on the Liang et al. (2013) exchange parameterization. Estimates of the global maximum and Arctic maximum / global subtropical mean N_2-fixation rates are shown as grey lines (details in main text), and the solid black line represents a N_2-fixation rate of zero. Biological N_2 removal is only significant when the magnitude of N_2-fixation exceeds the air-sea flux, which only occurs over a narrow range of conditions. Panel (b) shows the quasi-steady-state deviation of ΔN_2 from the bubble-induced supersaturation state ($\Delta_{eq,N2}$; Liang et al., 2013) for various wind speeds. Lines depict results calculated using different estimates of N_2-fixation rates, and shading represents the range of results over a range of temperate (0-25 °C) and salinity (0-35 PSU). A steady-state deviation value of 0 % means that bubble-mediated air-sea flux processes dominate over N_2-fixation. Other physical processes, including vertical mixing are ignored here. The x-scales on both panels are truncated at 18 m s^{-1} because air-sea fluxes almost always exceed N_2-fixation rates above this threshold.
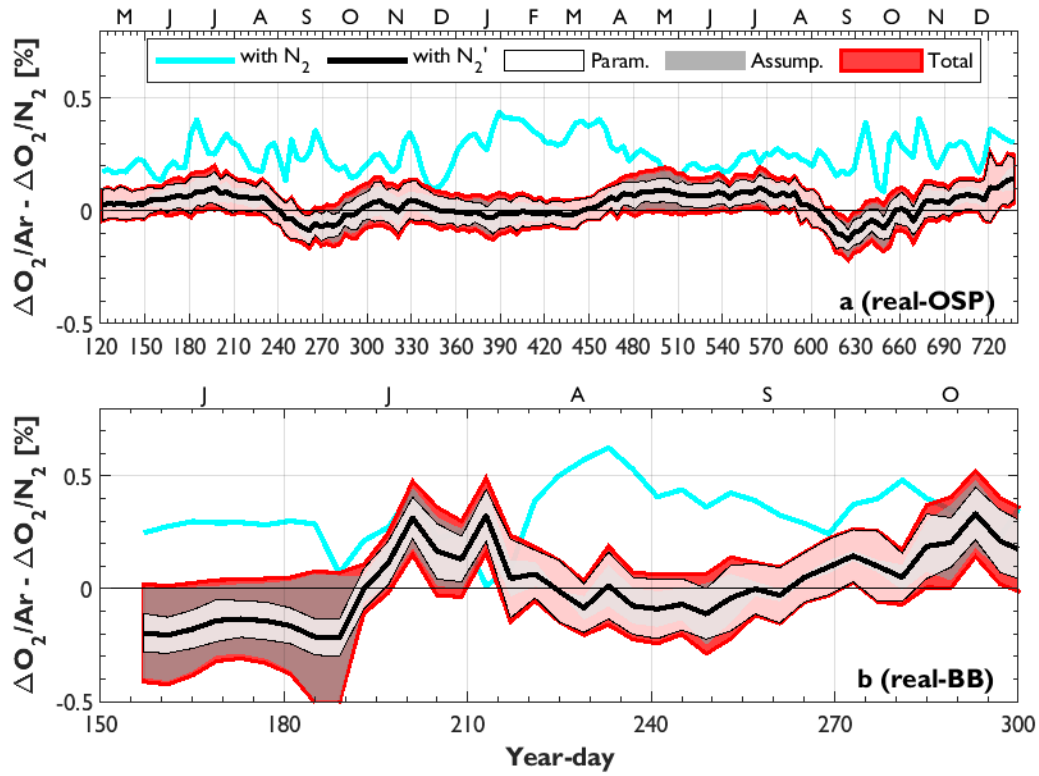
Figure S9. $\Delta O_2/Ar - \Delta O_2/N_2$ in the real-OSP (a) and real-BB (b) run c (full mixing) simulations. Uncertainty in $\Delta O_2/N_2'$ is represented as shaded regions around model-derived $\Delta O_2/Ar - \Delta O_2/N_2'$ values (black lines represent values with N_2', and blue lines are values with uncorrected N_2). The light grey patch represents the combined parameterization uncertainty, the dark grey patch is uncertainty from N_2' assumptions, and the red patch is the estimated total uncertainty, including the upper range of potential N_2-fixation. Mean uncertainty estimates are summarized in table S1.

Table S1. Sources of uncertainty in $\Delta O_2/N_2'$, based on the full mixing runs of the realistic simulations (real-OSP run c, and real-BB run c). We performed Monte Carlo simulations by randomly applying parameter errors to each variable separately and in combination. Reported uncertainty (upper section, right column; in order of descending importance) represents the range and mean (in parentheses) of values across the model simulations. The error associated with the N_2' budget assumptions (i.e. constant salinity, MLD, κ, and $\Delta N_2/Ar_{deep}$) was evaluated by running an additional simulation in which these terms were set to the true values from the full 1D simulation environment. The total uncertainty presented at the bottom of the upper section was derived by summing in quadrature each of the underlined errors. Additional biases and uncertainty in NCP calculations are shown in the lower section of the table. NCP errors are based on Eq. 5 in the main text, over a realistic SST, salinity and u_{10} range.

Parameter	Parameter Error	Absolute $\Delta O_2/N_2'$ uncertainty [%] Range (mean)
Sea surface temperature, SST	0.75 ^{o}C	0.02 – 0.1 (0.07)
Mixing coefficient, κ	10^{-5} $m^2\,s^{-1}$	0.001 – 0.05 (0.02)
Wind speed, u_{10}	2.5 $m\,s^{-1}$	0.002 – 0.06 (0.01)
Bubbled flux scaling coefficient, β	0.14	<0.001 – 0.05 (0.01)
Diffusive air-sea flux, F_d	15 % (relative)	0.001 – 0.03 (0.008)
Mixed layer depth, MLD	5 m	<0.001 – 0.03 (0.006)
Partial bubble flux, F_P	15 % (relative)	<0.001 – 0.02 (0.004)
Subsurface $\Delta N_2/Ar$, $\Delta N_2/Ar_{deep}$	0.25 %	0.001 – 0.02 (0.004)
Sea level pressure, SLP	2 mbar	<0.001 – 0.004 (0.002)
Small bubble flux, F_C	15 % (relative)	<0.001– 0.007 (0.002)
Combined parameterization		<u>0.04 – 0.2 (0.09)</u>
All assumptions		<u>0.001 – 0.3 (0.07)</u>
Total		**0.04 – 0.3 (0.1)**
Surface N_2-fixation		<0.05

Additional biases		
Parameter	Parameter value [%] Range (mean)	NCP error [mmol O_2 m^{-2} d^{-1}]
N_2 validation	0.9	N/A
Ex $\Delta O_2/Ar$ – $\Delta O_2/N_2$	0 – 1.1 (0.4)	0 - 19 (<7)
Real $\Delta O_2/Ar$ – $\Delta O_2/N_2$	0 – 0.8 (0.3)	0 – 14 (<6)
Ex $\Delta O_2/Ar$ – $\Delta O_2/N_2'$	0 – 0.5 (0.01)	0 – 9 (<0.2)
Real $\Delta O_2/Ar$ – $\Delta O_2/N_2'$	0 – 0.4 (0.01)	0 – 7 (<0.02)
Offshore mixing	N/A	0 – 50 (Izett et al., 2018)
Nearshore mixing	N/A	60 – 190 (Izett et al., 2018)
Diel $\Delta O_2/Ar$ variability	N/A	0 – 26 (Wang et al., 2020)